



HAL
open science

Towards neuromorphic computing on quantum many-body architectures: VO₂ transition dynamics

Melissa Alzate Banguero

► **To cite this version:**

Melissa Alzate Banguero. Towards neuromorphic computing on quantum many-body architectures: VO₂ transition dynamics. Neuroscience. Université Paris sciences et lettres, 2024. English. NNT: 2024UPSL021 . tel-04833426

HAL Id: tel-04833426

<https://pastel.hal.science/tel-04833426v1>

Submitted on 12 Dec 2024

HAL is a multi-disciplinary open access archive for the deposit and dissemination of scientific research documents, whether they are published or not. The documents may come from teaching and research institutions in France or abroad, or from public or private research centers.

L'archive ouverte pluridisciplinaire **HAL**, est destinée au dépôt et à la diffusion de documents scientifiques de niveau recherche, publiés ou non, émanant des établissements d'enseignement et de recherche français ou étrangers, des laboratoires publics ou privés.



THÈSE DE DOCTORAT

DE L'UNIVERSITÉ PSL

Préparée à l'École Supérieure de Physique
et de Chimie Industrielles de la ville de Paris

**Towards Neuromorphic Computing on Quantum
Many-Body Architectures: VO₂ Transition Dynamics**

**Circuits neuromorphiques à base de matériaux quantiques:
Dynamiques de transition du VO₂**

Soutenue par

Melissa ALZATE-BANGUERO

Le 27 Septembre 2024

École doctorale n°397

**École Doctorale Physique et
Chimie des Matériaux**

Spécialité

Physique et Chimie des Matériaux

Préparée au

Laboratoire de Physique et d'Etude des
Matériaux (LPEM)

Composition du jury :

Abhay SHUKLA *Président du jury*
Professeur - Sorbonne Université - IMPMC

Elena-Ioana VATAJELU *Rapporteuse*
Chargée de Recherche - Université Grenoble
Alpes - TIMA

Jérémie GRISOLIA *Rapporteur*
Professeur - INSA Toulouse - LPCNO

Laurie CALVET *Examinatrice*
Chargée de Recherche - École Polytechnique -
LPICM

Lionel AIGOUY *Directeur de thèse*
Directeur de Recherche - ESPCI-Paris - LPEM

Alexandre ZIMMERS *Co-Directeur de thèse*
Maître de conférences - Sorbonne Université -
ESPCI-Paris - LPEM

Acknowledgements

At the conclusion of this enriching learning experience, I wish to express my heartfelt gratitude to those who have accompanied me through this particularly rewarding professional and personal journey.

First and foremost, I would like to express my gratitude to the Marie Curie AI4TheScience Cofund for allowing me to be part of this amazing program with colleagues dedicated to making significant changes in scientific disciplines. This work was conducted with funding from the European Union’s Horizon 2020 research and innovation programme under the Marie Skłodowska-Curie grant agreement No 945304.

Furthermore, I am profoundly thankful for the opportunity to pursue my PhD at the *École Supérieure de Physique et de Chimie Industrielles de la Ville de Paris* (ESPCI–PSL Paris) in the *Laboratoire de Physique et d’Étude des Matériaux* (LPEM.)

I would like to express my heartfelt gratitude to my thesis directors. To Professor Lionel Aigouy, for his invaluable feedback, guidance, insightful management, and the trust he placed in me. His enlightened advice helped me to outline the main directions of this thesis. And to Professor Alexandre Zimmers, for his thoughtful comments, patience, and recommendations throughout the process. He notably gave me the opportunity to take part in international conferences that broadened my professional horizons. Their leadership has continuously inspired me, and their expert guidance has not only boosted my confidence but also facilitated the development of new skills and identified areas for improvement.

I am equally grateful to Professor Erica Carlson at Purdue University for engaging in captivating scientific discussions and for generously providing the resources necessary for completing the coding aspects of the thesis. I also want to acknowledge the invaluable contributions of her research group members – Sayan Basak, Yuxin Sun, Forrest Simmons, Amit Rajapurohita and Po-Yu Chen – whose collaboration played a crucial role in achieving publishable results.

I would like to express my gratitude to Zhuoqun Fang for providing samples and insights on the topic, and to Yingchao Ren for his invaluable support. I am also thankful to my colleagues and labmates Dongjiu Zhang, Mahima Chaudhry, Chenghao Xin, and Wei Zhou. Additionally, I appreciate Professor Zhuoying Chen for providing space in our group meetings. I would also like to acknowledge the support of Dimitri Yakovlev, Lina Makke, and Biswajit Biswas. Special thanks to Marie Claude Theme and Sophie Demonchaux for their assistance in helping me acclimate to the lab environment. I extend my sincere appreciation to the entire lab team for their warm welcome. Your presence contributed to a supportive, dynamic, and positive work environment.

Naturally, this experience owes much to my friends in Paris who were supportive and made

my life more beautiful by helping me adapt and including me in their plans as a family. Thank you to Thomas for his emotional support, care, and motivation during the writing process.

My deepest thanks go to my parents, Stella and Diego, for their unwavering support in all my endeavors, their countless sacrifices, and for being examples of perseverance and resilience in life. Thank you to my sister, Nathalia, for being an inspiration and for giving me the confidence and trust to take on this challenge.

Lastly, I want to express my gratitude to my extended family and friends who, by sharing my daily life, brightened my best days with enthusiasm and stood by me through moments of doubt. You have been a constant source of encouragement and love, and your support has been invaluable throughout this journey.

Résumé

Alors que les exigences en matière d'IA augmentent, de nouveaux paradigmes informatiques deviennent essentiels. Les architectures traditionnelles de von Neumann peinent à répondre aux exigences intensives de l'IA. L'informatique neuromorphique, inspirée par le cerveau, intègre traitement et mémoire pour une computation plus rapide et efficace, idéale pour des applications d'IA comme l'apprentissage profond et la reconnaissance de formes.

Les matériaux clés pour l'informatique neuromorphique incluent les synaptors et les neuristors. Les memristors, des mémoires non volatiles fabriquées à partir d'oxydes tels que HfO_2 et TiO_2 , imitent le comportement synaptique en changeant d'état via des filaments à l'échelle nanométrique ou des transitions de phase. Quant aux neuristors, ils imitent le celui du déclenchement des neurones en utilisant des memristors et des circuits résistance-condensateur reproduisant le modèle LIF (Leaky, Integrate, and Fire). À température ambiante, l'isolant de Mott VO_2 remplit les fonctions neuronales en formant des chemins conducteurs volatiles. Cependant, les synaptors et les neuristors nécessitent souvent des matériaux différents. L'optimisation de VO_2 comme synapse pourrait lui permettre de remplir les deux fonctions à température ambiante.

Étudier des systèmes à séparation de phases comme VO_2 reste complexe en raison des inhomogénéités. Les avancées en microscopie infrarouge et optique permettent désormais d'imager ces régions avec une résolution nanométrique. Les techniques de champ proche peuvent sonder la conductivité locale à l'échelle nanométrique. Cependant, ces sondes ont des limites : (i) des scans longs pour les inhomogénéités plus grandes et (ii) des transitions de phase induites par la température causant des dérives thermiques et des comparaisons d'images difficiles. Pour y remédier, nous avons développé un système de microscopie optique à champ lointain pour étudier les transitions de phase dans le VO_2 . Ce système exploite le contraste optique entre les phases isolantes et métalliques, observable des nanomètres aux microns.

Nous avons mis en œuvre différents protocoles de température en imagerie continue, compensant la dérive thermique et alignant des images nettes. Cela permet des traces temporelles de pixels uniques pour indiquer les températures spécifiques de transition de phase.

Nous avons tout d'abord cartographié la température critique (T_c), la largeur de transition (ΔT_c) et leur netteté (δT_c). Ces cartographies pourraient permettre d'adapter les propriétés du VO_2 pour des applications spécifiques comme les dispositifs de mémoire et les composants à commutation rapide.

Nous avons également présenté la première imagerie optique de la mémoire à inversion de rampe (RRM) dans le VO_2 , montrant l'évolution des clusters pendant l'entraînement thermique. L'accumulation de mémoire se produit aux frontières des clusters et à l'intérieur des patches, suggérant une diffusion préférentielle des défauts ponctuels.

De plus, nous avons mené une analyse d'apprentissage automatique (ML) des motifs fractals dans le VO₂, en utilisant le ML pour classifier l'Hamiltonien, conduisant à la formation de motifs. Notre réseau neuronal convolutionnel (CNN) a atteint une haute précision avec des données synthétiques et expérimentales, confirmant la formation de motifs due à la proximité d'un point critique du modèle Ising 2D à champ aléatoire. Cela, combiné à la réduction de symétrie et à la quantification de confiance, offre un puissant nouvel outil pour analyser les transitions de phase complexes dans les matériaux corrélés.

Notre recherche fournit une nouvelle méthode de caractérisation optique pour comprendre la dynamique de transition du VO₂ et introduit des approches innovantes pour des applications non-mémoires. Ces perspectives posent les bases d'études futures explorant le potentiel de la RRM et étendant les cadres ML à d'autres matériaux corrélés.

Mots-clés : circuit neuromorphique, dioxyde de vanadium, transition isolant-métal, caractérisation optique, mémoire non-volatile, réseau neuronal convolutionnel.

Abstract

As AI demands grow, new computing paradigms are essential. Traditional von Neumann architectures struggle with intensive AI requirements. Neuromorphic computing, inspired by the brain, integrates processing and memory for faster, efficient computation, ideal for AI applications like deep learning and pattern recognition.

Key materials for neuromorphic computing include synaptors and neuristors. Memristors, non-volatile memories made from oxides like HfO_2 and TiO_2 , mimic synaptic behavior by switching states via nanoscale filaments or phase transitions. Neuristors emulate neuron spiking behavior using memristors and resistance-capacitance circuits to replicate the Leaky, Integrate, and Fire model. Mott insulators like VO_2 mimic neuron-like behavior by forming volatile conductive pathways. However, synaptors and neuristors often require different materials. Optimizing VO_2 for synaptic behavior could enable it to serve both functions at room temperature.

Studying phase-separated systems like VO_2 is complex due to inhomogeneities. Advances in infrared and optical microscopy now allow imaging these regions with nanometer-scale resolution. Near-field techniques, using atomic force microscopes coupled to IR lasers, can probe local conductivity at the nanoscale. However, these probes have limitations : (i) long scans for larger inhomogeneities and (ii) temperature-driven phase transitions causing temperature drifts and difficult imaging comparisons.

To address these, we developed a far-field optical microscopy setup to study VO_2 phase transitions. This setup leverages optical contrast between insulating and metallic phases, observable from nanometers to microns. We applied different temperature protocols while continuously imaging, counteracting temperature drift and aligning sharp images. This enables single-pixel time traces to indicate specific phase transition temperatures.

We first mapped critical temperature (T_c), transition width (ΔT_c), and transition sharpness (δT_c) in VO_2 . These maps could enable tailoring VO_2 properties for specific applications like memory devices and fast switching components.

We also presented the first optical imaging of ramp reversal memory (RRM) in VO_2 , showing cluster evolution during thermal subloop training. Memory accumulation occurs at cluster boundaries and within patches, suggesting preferential diffusion of point defects. This could enhance memory effects through defect engineering, improving memory devices' robustness and stability.

Additionally, we pursued a machine learning (ML) analysis of fractal patterns in VO_2 , using ML to classify the Hamiltonian driving pattern formation. Our convolutional neural network (CNN) achieved high accuracy with synthetic and experimental data, confirming pattern formation driven by proximity to a critical point of the two-dimensional random field Ising model. This framework, combined with symmetry reduction and confidence quantification, offers a new

powerful tool for analyzing complex phase transitions in correlated materials.

Our research provides a new optical characterization method for understanding VO₂ transition dynamics and introduces innovative approaches for optimizing VO₂ for non-memory applications. These insights lay a foundation for future studies that explore RRM's potential, and extend ML frameworks to other correlated materials.

Keywords : neuromorphic devices, vanadium dioxide, insulating-to-metal transition, optical characterization, non-volatile memory, convolutional neural network.

List of Acronyms

AFM Atomic Force Microscopy	40
AI Artificial Intelligence	70
ANN Artificial Neural Network	3
CCD Charge-coupled device	44
CMOS Complementary Metal-Oxide-Semiconductor	3
DL Deep learning	35
DNNs Deep Neural Networks	5
IMT Insulator-to-metal transition	10
GST $\text{Ge}_2\text{Sb}_2\text{Te}_5$	9
KPFM Kelvin Probe Force Microscopy	31
LIF Leaky, Integrate, and Fire	9
MEMs micro-electromechanical systems	14
ML Machine learning	34
MRAM Magnetoresistive Random Access Memory	8
MTJs Magnetic Tunnel Junctions	8

MZMs Mach-Zehnder Modulator	11
NDR Negative Differential Resistance	10
ONNs Oscillatory Neural Network	14
PCM Phase Change Material	9
RRM Ramp Reversal Memory	70
SNNs Spiking Neural Network	9
SNOM Scanning Near-field Optical Microscopy	32
STDP Spike-Timing-Dependent Plasticity	9
STEM Scanning Transmission Electron Microscopy	40
STM Scanning Tunneling Microscopy	32
STOs Spin Torque Oscillators	10
STT-MRAM Spin Transfer Torque Magnetoresistive Random Access Memory	8
T_c transition temperature	22
VCSELs Vertical Cavity Surface Emitting Lasers	11
VO₂ vanadium dioxide	20
XRD X-ray Diffraction	32

Contents

Acknowledgements	i
Résumé	iii
Abstract	v
List of Acronyms	vii
List of Figures	xi
List of Tables	xix
1 Introduction	1
1 The Rise of Artificial Intelligence and Neuromorphic Computing	1
1.1 Potential of Neuromorphic Computing	2
1.2 Neuromorphic computing implementation approaches	3
1.3 Neuromorphic materials	7
1.4 Non-volatile Switching - Artificial Synapse	7
1.5 Volatile Switching - Artificial Neuron	9
1.6 Combining Neuristors and Synaptors on Single Chip	11
2 Aim of the thesis	17
2 Background on the Insulating-to-Metal Transition in VO₂ and Machine learning	20
1 IMT in VO ₂ films	20
1.1 Electrical properties of the IMT	22
1.2 Fabrication methods of VO ₂ thin films	27
1.3 Characterization methods to study VO ₂ IMT	29
2 Machine learning in materials science	34
2.1 Supervised learning	35
2.2 Deep learning	35
2.3 Machine learning in image processing	36
2.4 Convolutional neural networks	36
2.5 Material characterization and imaging	39
3 Optical characterization of VO₂	42
1 Materials and methods	44
1.1 Instrumentation- experimental set-up	44
1.2 VO ₂ samples	44

1.3	Image acquisition	47
1.4	Imaging workflow for micrographs automated acquisition	50
2	Image processing for applications	51
2.1	Obtaining single pixel time trace	51
2.2	Time domain convolution	54
2.3	Resolution limitation	56
3	Main achievements	57
4	Correlated maps to describe IMT in VO₂	58
1	Transition temperature maps	60
2	Hysteresis width maps	60
3	Transition width maps	60
4	Tc maps reproducibility	61
5	Correlations between maps	63
6	Deliberate pixel selection in search of specific thermal hysteresis characteristics	63
7	Analysis of parameters involved in the IMT	65
8	Main achievements	69
5	Ramp Reversal Memory	70
1	Following the Ramp Reversal Memory temperature protocol	71
2	Finding Tc maps differences with RRM	74
3	Mapping memory accumulation	79
4	Explaining RRM with a minimal model of point defect motion	83
5	Main achievements	85
6	Using Deep Learning for pattern recognition in VO₂	86
1	Hamiltonian models that could describe pattern formation	87
2	Synthetic images dataset	93
3	Model architecture	95
3.1	Outliers detection method	95
4	Vetting the Deep Learning model with experimental data	98
5	Classifying VO ₂ images acquired with optical set-up	102
6	Main achievements	105
	Conclusion and future work	106
	List of publications	111
	Bibliography	112

List of Figures

1.1	Comparison between the von Neumann and Neurmorphic architectures, depicting the operational differences. Taken from [12].	2
1.2	A biological neuron in comparison to an artificial neural network : (a) human neuron ; (b) artificial neural network in mathematical representation implemented in software ; (c) artificial neural network representation for implementation in hardware ; and (d) Deep Neural Networks structure. Example as a classifier, taking the pixel of an image as input, with two hidden layers of neurons, and giving the classification as a probability.Taken from [13].	4
1.3	a) Schematic representation of a biological neuron receiving input spikes from other neurons and triggering an ouput action potential when the membrane potential reaches the threshold value. b) The LIF artificial neurons based on Lapique’s model reproduce the evolution of the membrane potential thanks to a Resistance Capacitance (RC) circuit accumulating electrical charges. The Mott artificial neuron sketched in panel (c) reproduces the LIF behavior thanks to the accumulation of correlated metallic sites. Taken from [18].	7
1.4	a) Schematic of the emulated neural network. (b) Experimental setup featuring four spin-torque nano-oscillators connected in series and coupled through emitted microwave currents. Two microwave signals, fA and fB, encode inputs via a strip line, generating microwave fields. Total oscillator network output is recorded using a spectrum analyzer. (c) Microwave output from the oscillator network : light blue shows emissions without, and dark blue with, applied microwave signals. Peaks correspond to oscillator emissions ; narrow red peaks denote input frequencies fA and fB. (d) Evolution of oscillator frequencies as external source A frequency varies. Oscillators phase-lock to inputs near their natural frequencies, aligning their outputs with input frequency during locking. (e) Experimental synchronization map based on external signal frequencies fA and fB, illustrating different synchronization states. (f) Inputs applied to the system depicted in the (fA, fB) plane, where each color represents a different spoken vowel associated with various speakers’ data points (Taken from [35].)	13

1.5	(a) Caloritronic Neuron refers to a type of artificial neuron that uses the thermoelectric effect to generate electrical signals. In this design, a VO ₂ junction is placed under a Ti(titanium) heating strip above it. Spiking neuron : (b) Spikes, or brief pulses of electrical activity, are used as input and pass through the Ti heating strip. (c) As the input spikes pass through the Ti heating strip, heat build up which causes the VO ₂ junction to switch between its insulating and metallic states, generating an output spikes in the process. (d) Histograms of the integration time (time it takes for the output spike to occur), as a function of input pulse amplitude may show strong variability, as indicated by the red arrow (adapted from [53]). ReLU Mott Neuron : (e) The Ti strip is heated progressively in this configuration. (f) As the Ti strip heater heats up, the VO ₂ junction changes from an insulator to a metal state. This process happens progressively, with small patches switching in the VO ₂ junction. (g) The resulting output current from the VO ₂ junction is used to generate a ReLU(Rectified Linear Unit) curve. This curve can show sudden changes in the output current, as some patches switch abruptly due to local IMT avalanches. These jumps can increase as the device size is reduced (adapted from [59]).	15
1.6	Various recent methods to create synaptors in VO ₂ . Ohmic impedance coupling, achieved through (a) ion bombardment [63], (b) E-field breakdown [64], and (c) three terminal gating. Full impedance coupling using breadboard resistors and capacitors [65]. (d) Thermally induced coupling has been achieved using two VO ₂ neuroresistors separated by 12μm [33, 66].	16
1.7	a) Schematic illustrating the scope of the thesis	17
2.1	(a)Schematic depictions of the crystal structures of the low- temperature monoclinic M1, intermediate M2, and high-temperature tetragonal rutile R phases. V-V distances are highlighted. (b)Molecular orbital diagram depicting the electronic structure of the monoclinic and tetragonal phases of VO ₂ . The left MO diagram corresponds to the undistorted metallic phase of VO ₂ , whereas the diagram on the right shows the altered MO diagram upon transition to the distorted insulating phase of VO ₂ . Taken from [67].	21
2.2	(a) Hysteresis graph depicting the drop in resistance upon the IMT in a VO ₂ thin film.(b)Micrographs of the VO ₂ samples used for the experiment of the present work. There is a color change between the insulating (light gray) and metallic phases (dark gray).	24
2.3	The current vs. voltage characteristic of a VO ₂ device presents three regions: at first, the device is in its insulating state. As the voltage drop across the device is high enough to trigger the phase transition, the material undergoes the phase change and a negative differential resistance regime is formed. Lastly, the device stabilizes in its metallic state. The measurement was conducted sourcing a current and measuring the voltage across a VO ₂ device. Taken from [113].	26
2.4	(a) Temperature-dependent optical reflectance and transmittance spectra for the 30-nm VO ₂ film thickness for temperatures of 20, 60, 70, 80, and 99°C. (b) Optical transmittance at 1550nm for 8.6, 12.5, 18, 30, 44, and 57-nm VO ₂ film thicknesses shows the hysteretic nature of the transition (red: heating, blue: cooling) . Taken from [114].	27
2.5	Schematic diagram of the IMT in the VO ₂ film. (a)The metallic domains start to form nucleation droplets in the film surface sporadically, as T approaches T _c . (b)The domains grow larger and start to form clusters as T increases further.(c) Above T _c , the metallic domains form an infinite cluster. Taken from [134].	29

2.6	(I) Images of the near-field scattering amplitude over the same $4\mu\text{m} \times 4\mu\text{m}$ area obtained by SNOM operating at the infrared frequency $\omega = 930\text{ cm}^{-1}$. These images are displayed for representative temperatures in the insulator-to-metal transition regime of VO_2 to show percolation in progress. The metallic regions (light blue, green, and red colors) give higher scattering near-field amplitude compared with the insulating phase (dark blue color). Taken from [84]. (II) Work function maps using KPFM at (a) 285, (b) 305, (c) 335 and (d) 355K during heating. The color scale is the same for all images. The larger work function (red) represents the insulating phase and the smaller work function (blue) represents the metallic phase. (e) The surface morphology of the region used to obtain the work function maps. The scale bar is 100 nm. Taken from [130].	30
2.7	Illustration of the hierarchical feature representation within CNNs. A Comparison of concepts contained in different network levels (neuron, channel, and layer). b Visualization of CNN filters from different layers of an imageNet pretrained VGG16 network. Note that the filter representations become more and more complicated as filter positions move deep along the network. The early layer filter representations are relatively primitive, while the top layer filter representations are highly complicated. The VGG16 architecture is plotted using the plot neural net library. Filter representations are visualized using the convolutional neural network visualizations library. Taken from [148].	37
2.8	Convolutional neural network structure	38
2.9	Schematic diagram of the IMT in the VO_2 film. (a) STM spectroscopic images of $\text{La}_{1-x}\text{Ca}_x\text{MnO}_3$ (with x of about 0.3) showcasing the insulating (paramagnetic, light colors) and metallic (ferromagnetic, dark colors) of a thin film of $0.61\mu\text{m} \times 0.61\mu\text{m}$. [150] (b) Images of the near-field scattering amplitude of $4\mu\text{m} \times 4\mu\text{m}$ thin film of VO_2 showing that the metallic regions (light blue, green, and red colors) and the insulating phase (dark blue color) [84]. (c) High-resolution co-localized near-field images of coexisting phases antiferromagnetic insulator (blue) to paramagnetic metal (red) phase; $6\mu\text{m} \times \mu\text{m}$ [151]. (d) MFM images of a LPCMO $8\mu\text{m} \times 8\mu\text{m}$ thin films showing the antiferromagnetic (blue) and the ferromagnetic (red) phases [152]. (e) The AFM domain map at 130K (warming cycle) is binarized to highlight the AFM domains insulating (yellow) and paramagnetic-metallic domains (blue) [153]. (f) Na-CCOC images ($4\text{ nm} \times 4\text{ nm}$) of $\Delta^2 R$ (Laplacian) computed from R maps. Large R (yellow) means that the corresponding tunneling spectrum is more symmetric, whereas low R (blue) means that it is more asymmetric [154].	39
3.1	Experimental set-up displaying the microscope hardware, optics, and temperature controller to perform the characterization of the samples.	43

3.2	Schematics of the microscope and image analysis created specifically to measure spatial maps of clusters in VO ₂ during the IMT while recording resistivity R(T) simultaneously. The sample was positioned on a Peltier heater or Linkam Thms350V temperature controller to apply temperature ramps (bottom left). The sample height was varied by steps of 80nm via a piezoelectric actuator placed under it or in the objective. The best-focused images were chosen post-experiment using an image compression method and Tenengrad function. The height focus of the sample was thus controlled within 80nm throughout the experiment. Fine <i>xy</i> plane drift correction within a single pixel was performed post-experiment. Camera sensitivity was normalized throughout the recording. Using this fully stabilized image series, black and white thresholds were applied for each pixel individually, accurately determining if it is in the metallic or insulating state. We use this information to construct spatial maps of the local transition temperature T _c , hysteresis width ΔT _c and transition width δT _c . The map size displayed in this figure is 33.6 μm × 27.6 μm.	45
3.3	The structure of the primary planes of the sapphire crystal corresponding to the structure system of sapphire. Taken from [165].	45
3.4	Micrographs of the VO ₂ samples used for the experiment of the present work. The samples have different electrodes geometry. Green colored area represents VO ₂ ; pink area, gold electrodes; and blue area, sapphire substrate. The white bar is 10 μm wide. (a) Sample A prepared by RF magnetron sputtering on a r-cut sapphire substrate. (b) and (c) Sample B (84 nm) and C (136 nm), both prepared by sol-gel method on a c-cut sapphire substrate.	46
3.5	Tenengrad of a stack of 20 micrographs. The sharpest image corresponds to the maximum Tenengrad value.	48
3.6	Flowchart displaying the logic of the Labview program for the automatic acquisition of the sharpest micrographs.	49
3.7	Flowchart followed to process raw micrographs and obtain single-pixel time trace of the VO ₂ area.	52
3.8	Pair connectivity correlation length ξ _{pair} vs. temperature during the warming branch of an extremal hysteresis loop, as a function of different threshold values for determining metal and insulator domains in sample A. The correlation length diverges when the system is closest to criticality.	55
3.9	(a) Single pixel time trace of intensity. The blue curve is the raw time trace of the measured optical intensity of pixel (127,734) in sample A. The orange curve is a Gaussian convolution (σ=2.5) of the same time trace over 3 frames. The double crossing at the midway is eliminated in the smoothed data set. (b) Binary black and white image (frame 260) of the sample generated by thresholding at midway the single pixel time traces as presented in (a). (c) Smoothed out binary black and white image (frame 260) of the sample generated by thresholding at midway the 3 frame convoluted single pixel time traces as presented in (a). Frame 260 map size is is 33.6 μm × 27.6 μm.	56

4.1	(a) Optical image of VO ₂ sample A during the insulator (light gray) to metal (dark gray) transition (warming cycle), two gold leads are seen at the top and bottom. These electrodes also display some structure (spots) due to gold surface imperfections. Sapphire substrate is the dark surface. Scale bar is 10 μ m. (b) Single pixel intensity curve defining critical temperature T _c , hysteresis width ΔT_c and transition width δT_c . T _c were determined at midways as explained in the main text. Hysteresis width was determine by taking the temperature differences between heating and cooling cycles T _c ^{up} -T _c ^{down} . Transition width was determined by fitting (smooth curve) the single time trace to a hyperbolic tangent: $-\frac{1}{2}(\tanh(\frac{T-T_c}{\delta T_c})-1)$. (c) Local critical temperature T _c map, (d) ΔT_c maps, (e) δT_c map (presented here for the temperature ramping up branch). Image are 27.6 μ m high. Histograms (with mean and standard deviation of maps a), b) and c) are shown in Fig. 4.2.	59
4.2	Histograms of maps presented in Fig. 4.1 and 4.3. (a) T _c maps (upon warming); (b) ΔT_c map; (c) δT_c map and (d) and (e) two difference maps T _{c2} - T _{c1} and T _{c3} - T _{c2}	61
4.3	(a) Three T _c maps while cycling through the IMT (warming) at 1°C/min. (b) Difference maps T _{c2} -T _{c1} and T _{c3} -T _{c2} between cycles. Global patterns are generally reproducible ($\sigma_{T_c}/T_c = 0.6^\circ\text{C}/68^\circ\text{C} = 1\%$). However some small regions present deviations up to $\pm 2^\circ\text{C}$. Maps size is 33.6 $\mu\text{m} \times 27.6 \mu\text{m}$	62
4.4	Correlations between T _c (upon warming), ΔT_c and δT_c . Each of the 666,000 pixels (900x740) is represented. T _c vs. ΔT_c (panel (a) shows a slight diagonal trend meaning that pixels with low T _c tend to have low ΔT_c (<i>i.e.</i> close to zero) and <i>vice versa</i> (see red dashed line.)	62
4.5	T _c map (33.6 $\mu\text{m} \times 27.6 \mu\text{m}$) with six pixels chosen to illustrate specific characteristics in the hysteresis loops. The table shows the numerical values of T _c , ΔT_c and δT_c for each pixel. The numbers in bold highlight the unique characteristic of each pixel.	64
4.6	(a) Room temperature XRD patterns of VO ₂ : Sample B epitaxy (preferentially oriented, red curve) and Sample C non epitaxy (gray curve). (b) Hysteresis loop of Sample B (gray curve) and Sample C (red curve). (c) and (d) Critical temperature values T _c ^{up} , T _c ^{down} , and ΔT_c , derived from the electrical characterization of Sample B and C respectively.	66
4.7	T _c maps of VO ₂ samples: (a) Sample B Preferentially oriented (Epitaxy), (b) Sample C Non preferentially oriented (Non epitaxy) at the same scale (temperature range of 10 °C), (c) Zoom over the range of temperatures for the epitaxy samples. It is observed that the epitaxy sample is more homogenous in T _c values over a range of 10 °C than the non epitaxy one. The analyzed area of the VO ₂ samples is 15 $\mu\text{m} \times 15 \mu\text{m}$	67
4.8	Histograms of VO ₂ samples: (a) Sample C ΔT_c of , (b) Sample C δT_c , (c) Sample B ΔT_c at same scale, to show the sharpness difference in the distribution of the samples B and C, (d) Sample B δT_c	68

5.1	(a) Ramp Reversal temperature protocol. Major loop labels are as follows: ML1-W stands for Major Loop 1 upon warming; ML1-C stands for Major Loop 1 upon cooling, and similarly for other major loops. In the subloops, temperature is varied repeatedly between a low temperature of $T_{Ln} = 59.5^{\circ}\text{C}$ and a high temperature of $T_{Hn} = 68^{\circ}\text{C}$, through a total of $n=11$ complete subloops. (b) Average intensity <i>vs.</i> frame number. Intensity is on a grayscale of 0 (black) to 255 (white), after accounting for illumination variation (detailed elsewhere). The light gray dashed line follows the average intensity at the end of each subloop. Inset: Fit of the average intensity at the end of each subloop (<i>i.e.</i> at T_{Hn}), <i>vs.</i> subloop index n , to an exponential saturation. The time constant is $n_{\tau} = 3.1 \pm 0.5$ subloops.	71
5.2	(a) Hysteresis curves of average intensity <i>vs.</i> temperature throughout the Ramp Reversal protocol of Fig. 5.1. (d) Zoom showing the progressive increase after each subloop of the averaged intensity around the high temperature turning point $T_H=68^{\circ}\text{C}$	72
5.3	(a) and (b) $R(T)$ measurement of the metal-insulator transition during the full ramp reversal sweep. ML1, ML3, ML4 curves overlap as seen previously. ^[182] (c) At $T_H=68^{\circ}\text{C}$, resistance rises from $30\text{k}\Omega$ at T_{H0} to $53\text{k}\Omega$ at T_{H11} with a characteristic time of 2.2 subloops. (d) $\Delta R/R$ between ML1 and ML2 reaches 350% increase around 68.8°C	73
5.4	(a) T_c map acquired during the warming branch of the first major loop (called ML1-W). The analyzed area of the VO_2 sample has a map size of $33.6 \mu\text{m} \times 28 \mu\text{m}$ ($900 \text{ pixels} \times 750 \text{ pixels}$). (b) T_c map acquired during the warming branch of the second major loop (ML2-W) after 11 subloops memory training. (c) Histograms of ML1-W and ML2-W maps. (d) Plot of the average transition temperature and standard deviation for all 4 major loops.	75
5.5	(a) Difference in T_c maps between ML4-W and ML1-W. (b) Difference in T_c maps when cycling through two transition $[n]$ and $[n-1]$ as presented in Chapter 3; (c) Difference in T_c maps between ML4-W and ML2-W (<i>i.e.</i> with ramp reversal memory). Panels (d) (e) and (f) are corresponding histograms. Maps size is $33.6 \mu\text{m} \times 28 \mu\text{m}$ ($900 \text{ pixels} \times 750 \text{ pixels}$).	76
5.6	(a) T_c maps from ML1-W and ML2-W (as shown in Fig. 5.4) side by side with T_c maps ML3-W and ML4W after ramping the sample to high temperatures. The frame color code (green or black) is the same as in Fig. 5.1 and Fig. 5.4. (b) Thresholded difference between the T_c maps of ML1-W and ML2-W (left panel) and between ML4-W and ML2-W (right panel). T_c has risen in red regions and has lowered in blue regions. White regions ($\pm 0.1^{\circ}\text{C}$ around 0°C) identify where T_c only changes within the temperature resolution ($\sim 0.17^{\circ}\text{C}$), and thus the temperature remains the same within error bars. Maps size is $33.6 \mu\text{m} \times 28 \mu\text{m}$ ($900 \text{ pixels} \times 750 \text{ pixels}$).	77

5.7	Experimental ML1-W maps thresholded at the average $T_c = 68.13^\circ\text{C}$. White patches have high T_c ; black patches have low T_c . (b) Difference between ML2-W and ML1-W T_c maps, thresholded at $\Delta T_c = 0^\circ\text{C}$. White patches in this panel, T_c became higher when passing from ML1 to ML2; Black patches, T_c became lower when passing from ML1 to ML2. (b) incorporating temperature resolution considerations. A two color difference map is used here for simplicity. (c) 4 color maps using (a) and (b). Orange patches have a high ML1 T_c and an even higher T_c in ML2. Cyan patches have a low ML1 T_c and an even lower ML2 T_c . In dark gray regions, a high ML1 T_c changed to a lower ML2 T_c . In light gray regions, a low ML1 T_c changed to a higher ML2 T_c . As the sample is cycled through the ramp reversal protocol, some extreme T_c 's become more extreme as seen by the presence of orange and cyan patches in (c). Maps size is $33.6 \mu\text{m} \times 28 \mu\text{m}$ ($900 \text{ pixels} \times 750 \text{ pixels}$).	78
5.8	Memory maps: (a) Experimental evolution of the spatial map of metal and insulator domains upon training with successive temperature subloops. Top left panel: Metal and insulator patches right before the first subloop begins, at TH0. Metallic patches are colored dark gray, and insulating patches are colored light gray. Image is $28 \mu\text{m}$ high. (b) Bottom panels show the corresponding histograms during training and reset.	80
5.9	Memory maps as shown in Fig.5.8 at different TH. VO_2 area is $33.6 \mu\text{m} \times 28 \mu\text{m}$ ($900 \text{ pixels} \times 750 \text{ pixels}$).	81
5.10	Exponential fit for all TH. There is a peak in the time constant for TH= 69°C while the amplitude peaks around $68 - 69^\circ\text{C}$, however the changes between these two temperatures are within error bars.	82
5.11	Accumulated memory maps: (a) Experimental and (b) simulated averaged metal and insulator domains at the end of each subloop. The images are a direct average over 10 subloops of the THn-TH0 images. Dark gray denotes regions that are metallic at TH; light gray denotes regions that are insulating at TH. Yellow regions are places where the insulator advanced as compared to TH0. Blue regions are places where the metal advanced as compared to TH0. Light yellow regions are typically regions that became insulating only at the end of the 10 subloops. Bright yellow regions however are regions that became insulating at the beginning of the subloops. Red contours mark the original metal-insulator boundaries at TH0, before the subloops begin. Maps size is $33.6 \mu\text{m} \times 28 \mu\text{m}$.	85
6.1	Typical critical configurations generated from simulations of clean and random field Ising models and percolation models. Each simulation image is 100×100 pixels.	92
6.2	Symmetry reduction method, as described in the text.	94
6.3	Convolutional Neural Network. The multi-dimensional output 2b is flattened into a one-dimensional array (3a) before it is fed into the fully connected layer. We use the Adam (Adaptive moment estimation) optimization algorithm to train the network. The output label is determined using softmax activation on the output layer.	96
6.4	Error in the training and validation set vs. the number of epochs. Epochs correspond to the number of times the training set went through a training process. To prevent overfitting we chose epoch=4 for testing with experimental images. Training/Validation accuracy = $99.64\%/99.67\%$.	97

6.5	Distribution of values of the output nodes for each class in the last fully connected layer, for all of the training sets. These clusters inhabit a 7-dimensional 'model' space. The two representations in the figure are projections of the same 7-dimensional information onto two different 3-dimensional subspaces.	98
6.6	Classification results of our deep learning model applied to SNOM images on a thin film of VO ₂ . The top row shows the thresholded data showing insulating (white) and metallic (black) patches. The total percentage of classifications for a particular model are reported in the bar charts of panels (a)-(d). Classification percentages that fall within 1σ of a cluster in the training set are indicated in parentheses. Classifications that fall more than 1σ away from the edge of the corresponding cluster in the training set are colored darker in the bar chart. SNOM images are 4 μm × 4 μm (256 × 256 pixels).	99
6.7	Distribution of values of the output nodes for each class in the last fully connected layer, for the VO ₂ SNOM data, superimposed on the distribution for the training sets shown in Fig. 6.5. Results for the VO ₂ data that are within one 7-dimensional standard deviation of a training set are indicated by orange dots. Results for the VO ₂ data that are farther away are indicated by black dots.	101
6.8	Classification results of our deep learning model applied to new 28 μm × 28 μm optical microscopy images of a VO ₂ thin film showing metallic(black) and insulating (white) patches. The total percentage of classifications for a particular model are reported in the bar charts of panels (a)-(e). Classification percentages that fall within 1σ of a cluster in the training set are indicated in parentheses. Classifications that fall more than 1σ away from the edge of the corresponding cluster in the training set are colored darker in the bar chart.	103
6.9	Distribution of relative weights of each class in the last fully connected layer, for the VO ₂ optical data (square sample presented in Fig. 6.8), superimposed on the distribution for the training sets shown in Fig. 6.5. Results for the VO ₂ data that are within one 7-dimensional standard deviation of a training set are indicated by orange dots. Results for the VO ₂ data that are farther away are indicated by black dots.	104
6.10	All CNN predictions from optical data during a temperature ramp up of data presented in Fig. 6.8. Darker colors denote classifications that are more than 1 standard deviation from the identified training set.	105
7.11	An overview of the applications derived from the optical characterization setup reveals that T _c maps have been used to identify hysteresis features in VO ₂ samples synthesized using different methods, such as sol-gel and RF sputtering. The sol-gel samples were provided by Z. Fang from ESPCI, while Professor Schuller from USCD supplied the RF sputtering samples. These maps not only enhance our understanding of the RRM mechanism but also serve as a valuable tool in other areas. For instance, thresholded images that distinctly depict the insulating and metallic phases are utilized in the deep learning classifier, the tracking of avalanches, and RRM.	110

List of Tables

1.1	Examples of materials and devices for Resistive Switching-based non-volatile memory for neuromorphic computing based on [20]	14
2.1	Characterization methods and their characteristics to study phase transitions on VO ₂	33
4.1	IMT characteristics of VO ₂ thin films on Sapphire substrates.	65

Chapter 1

Introduction

1 The Rise of Artificial Intelligence and Neuromorphic Computing

Artificial Intelligence(AI) refers to the capability of machines to perform tasks traditionally associated with human cognition [1][2]. Today, with vast amounts of data, rapid computational power, and improved algorithms, computers can efficiently perform many cognitive tasks, such as writing, playing games, recognizing patterns, and describing images[3]. The evolution from using an abacus to ultra-fast calculations on modern supercomputers mirrors the journey from simple tools to sophisticated reasoning machines, a reminiscence of Leibniz's *calculus ratorator*, transforming the mechanization of arithmetic into the mechanization of thought[4].

AI has an impact now in most industries, including pharmaceutical, defense, and energy, among others. It has also been responsible for scientific breakthroughs like the protein folding fast prediction by AlphaFold [5]. AI utilizes more complex models as it can solve more complex tasks, and for this reason, there is a need for more efficient and powerful computational frameworks [6].

However, traditional computing architectures, based on the von Neumann model, face limitations in processing speed and energy efficiency when tasked with AI workloads. For instance, if we continue with the current ways of computation, the integration of AI into search tools like Google could dramatically increase their electricity demand, potentially tenfold. According to the latest report of the International Energy Agency in 2024, a typical Google search uses 0.3 Wh of electricity, whereas an OpenAI ChatGPT request consumes 2.9 Wh. With 9 billion searches conducted daily, this shift would require nearly 10 TWh of additional electricity annually [7]. By 2026, the AI industry's electricity consumption is expected to be at least ten times what it is today.

The usage of energy for the AI workload occurs in two key stages: training and inference. Training models, which involve processing vast amounts of data, currently account for 20% of AI's energy use. However, once these models are deployed in the inference phase to solve real-world problems, they consume the remaining 80% [8]. As AI becomes integral to diverse

Neuromorphic computing offers several advantages:

1-Highly Parallel Computations: Neurons in a neuromorphic system are highly interconnected, allowing for massive parallelism, similar to the brain's neural networks. However, current neuromorphic operations are simpler compared to the sophisticated parallel programming achieved in Von Neumann architectures.

2-Unified Processing and Memory: There is no separation between processing and memory. Neurons and synapses both process and store information, reducing the need for frequent data access and mitigating the memory wall issue.

3-Energy Efficiency: Neuromorphic systems reduce energy consumption by minimizing data access. They are designed to compute only when necessary, leveraging event-driven computation, meaning they process information only when data is available. This leads to extremely efficient computation since neurons and synapses are active only when spikes occur, and spikes are typically sparse.

4-Scalability: Neuromorphic hardware is scalable. By adding more neuromorphic chips, the number of neurons and synapses can be increased, as demonstrated by large-scale systems like SpiNNaker and Loihi.

5-Robustness Against Noise: Neuromorphic systems are inherently robust against noise, contributing to their reliability and efficiency.

1.2 Neuromorphic computing implementation approaches

The first approach to implementing neuromorphic computing involves mapping Artificial Neural Network (ANN) algorithms, which are the algorithms currently used in AI, to be executed using available Complementary Metal-Oxide-Semiconductor (CMOS)-based electronic devices.

To understand how ANNs work, one can draw a parallel with biological neural networks. Biological neurons consist of three main parts: dendrites, which receive signals from other neurons; the soma or cell body, which acts as the CPU where signals are integrated and processed; and axons, which transmit the processed signals to other neurons through synapses (Fig. 1.2(a)). Synapses function as connectors, transferring signals from the axon terminal of one neuron to the dendrites of the next neuron.

ANNs simplify this complex behavior into a mathematical model consisting of weighted sums and activation functions (Fig. 1.2(b)). In an ANN, there are multiple inputs x_i , with synapses acting as valves for information, determining the flow of data through the network and guiding input information to the relevant output. These synapses can transmit information both positively and negatively, represented by real-valued synaptic weights w_i . The weights indicate the importance of each connection. The network performs a weighted sum operation,

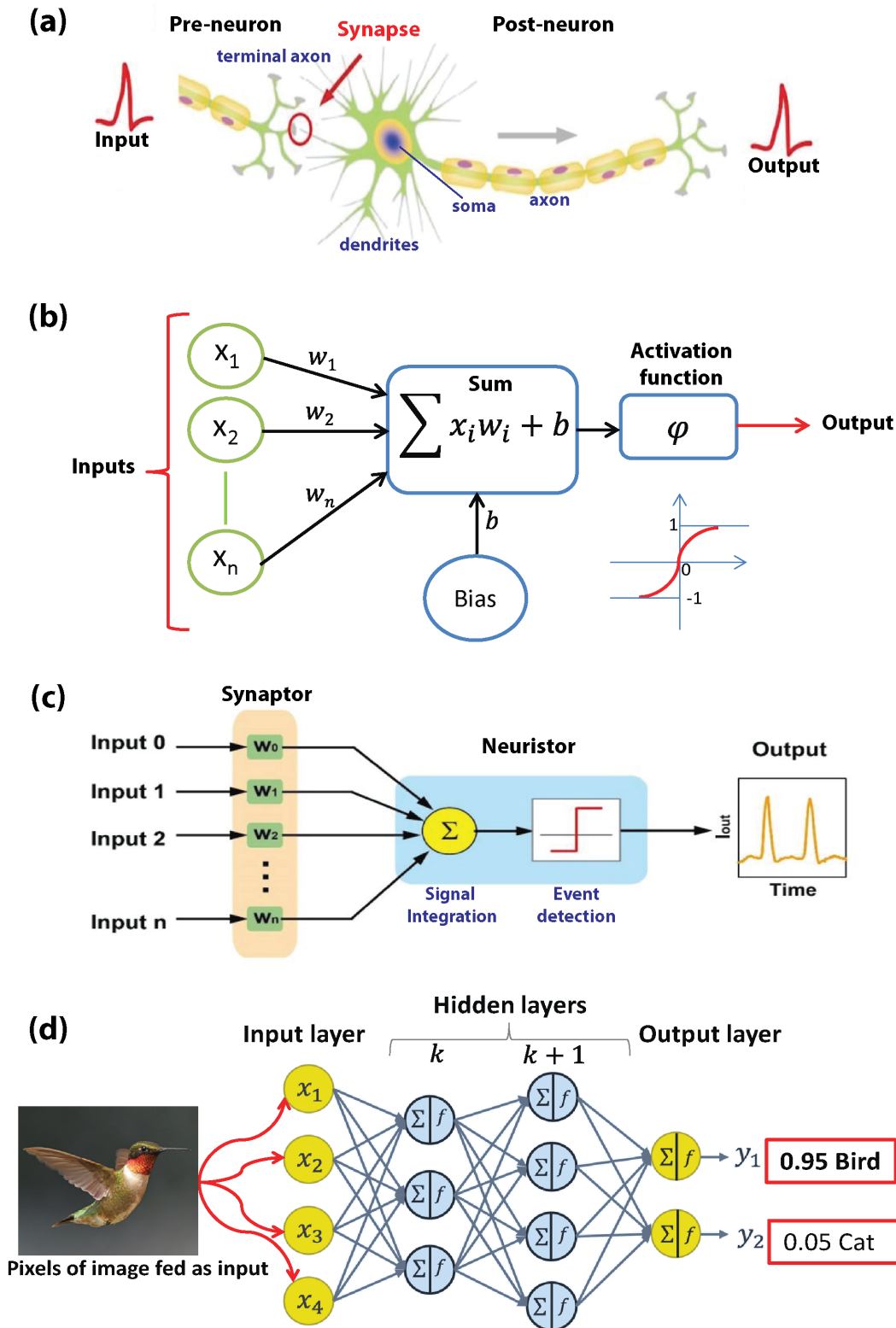


Figure 1.2 – A biological neuron in comparison to an artificial neural network: (a) human neuron; (b) artificial neural network in mathematical representation implemented in software; (c) artificial neural network representation for implementation in hardware; and (d) Deep Neural Networks structure. Example as a classifier, taking the pixel of an image as input, with two hidden layers of neurons, and giving the classification as a probability. Taken from [13].

followed by a nonlinear activation function, such as a sigmoid or a rectified linear unit (ReLU). This nonlinearity allows the neural network to approximate complex nonlinear functions. The hardware equivalent is presented in Fig. 1.2 (c), where the device in charge of accumulating memory (weights) is called **synaptor**, and the signal integration and activation that produces the output is performed by a **neuristor**. The mechanism is analogous to the accumulation of action potentials in biological neurons and to the spike transmission that occurs when a biological neuron reaches a threshold.

The most implemented neural networks today are known as **Deep Neural Networks (DNNs)** because they consist of many layers of neurons, ranging from four layers to hundreds (Fig. 1.2(d)). A special class of DNNs is convolutional neural networks (CNNs), which typically handle images and other types of high-dimensional data, and reduce this data to a few output classes, identifying, for instance, whether an image contains a bird or a cat [14].

In an ANN, the input to a neuron in layer $k+1$ is the output of neurons in layer k multiplied by the synaptic weights. This process is crucial for the functioning of artificial neural networks. During the training phase, the weights are initially chosen randomly, and the network learns the optimal weights through a process called supervised learning. In **supervised learning**, labeled examples are presented to the network, and its output is compared with the desired output to compute an error. This error is then backpropagated through the network, adjusting each weight in proportion to its contribution to the error. After several training iterations, the network minimizes the error and can generalize to new, unseen examples what we call inference phase. Algorithm 1 illustrates the process of learning in a simple ANN with one hidden layer.

Implementing neuromorphic architectures using only CMOS technology presents significant challenges. Emulating each neuron requires dozens of transistors, and additional external memories are necessary for synapses. Although transistors are tens of nanometers in size, CMOS-based artificial neurons and synapses are typically several micrometers wide. This size discrepancy limits the integration density of physical neurons and synapses. To address these challenges, two scalable architectures have been proposed for mapping DNNs on-chip using physics: hybrid CMOS/memristive[15] systems and photonic systems [16].

Some hybrid systems, such as those in BrainScale[17], use analog electronics to physically implement neurons. For example, the membrane potential of each neuron is represented by the charge stored in a capacitor, and neurons emit spikes when the capacitor's voltage reaches a preset threshold (Fig. 1.3(a)). These systems are hybrid because the spike is not an analog action potential but a digital spike event communicated through a network that digitally implements the synaptic connections.

These silicon neuromorphic computing systems require capacitors for compact neuron representation, but miniaturizing these capacitors remains a significant challenge. In some designs, capacitors representing neuron membrane potentials occupy up to 70% of the chip's area. The miniaturization is constrained by the dielectric constant of CMOS-compatible materials. While silicon excels in memory storage, it does not easily mimic neuron-like behavior. Developing efficient and feasible neuromorphic hardware solutions **necessitates exploring materials that can naturally mimic synapses and neurons**.

Algorithm 1 Learning the function $f(x) = x^2$

Neural network architecture:

Input layer: 1 neuron

Hidden layer: 2 neurons (ReLU activation)

Output layer: 1 neuron

Step 1: Initialization

Initialize weights and biases:

$$W_1 = [0.1, -0.2], b_1 = [0.0, 0.0]$$

$$W_2 = [0.3, 0.4], b_2 = 0.0$$

Step 2: Forward PassPass input $x = 1$ through the network:

$$h_1 = \text{ReLU}(x \cdot W_{1,1} + b_{1,1}) = \text{ReLU}(0.1) = 0.1$$

$$h_2 = \text{ReLU}(x \cdot W_{1,2} + b_{1,2}) = \text{ReLU}(-0.2) = 0.0$$

$$y_{\text{pred}} = h_1 \cdot W_{2,1} + h_2 \cdot W_{2,2} + b_2 = 0.03$$

Step 3: Calculate ErrorTrue output $y = 1$

$$\text{Error} = \frac{1}{2}(y_{\text{true}} - y_{\text{pred}})^2 = 0.47045$$

Step 4: Backward Pass (Gradient Descent)Learning rate $\alpha = 0.1$

Compute gradients and update weights and biases:

Gradients for W_2, b_2 :

$$\frac{\partial \text{Error}}{\partial W_{2,1}} = -0.097, \frac{\partial \text{Error}}{\partial W_{2,2}} = 0.0$$

$$\frac{\partial \text{Error}}{\partial b_2} = -0.97$$

$$\text{Update: } W_{2,1} = 0.3097, W_{2,2} = 0.4, b_2 = 0.097$$

Gradients for W_1, b_1 :

$$\frac{\partial \text{Error}}{\partial W_{1,1}} = -0.299409, \frac{\partial \text{Error}}{\partial W_{1,2}} = 0$$

$$\frac{\partial \text{Error}}{\partial b_{1,1}} = -0.299409, \frac{\partial \text{Error}}{\partial b_{1,2}} = 0$$

$$\text{Update: } W_{1,1} = 0.1299409, W_{1,2} = -0.2, b_{1,1} = 0.0299409, b_{1,2} = 0.0$$

Step 5: IterateRepeat steps 2-4 for multiple iterations to minimize error.

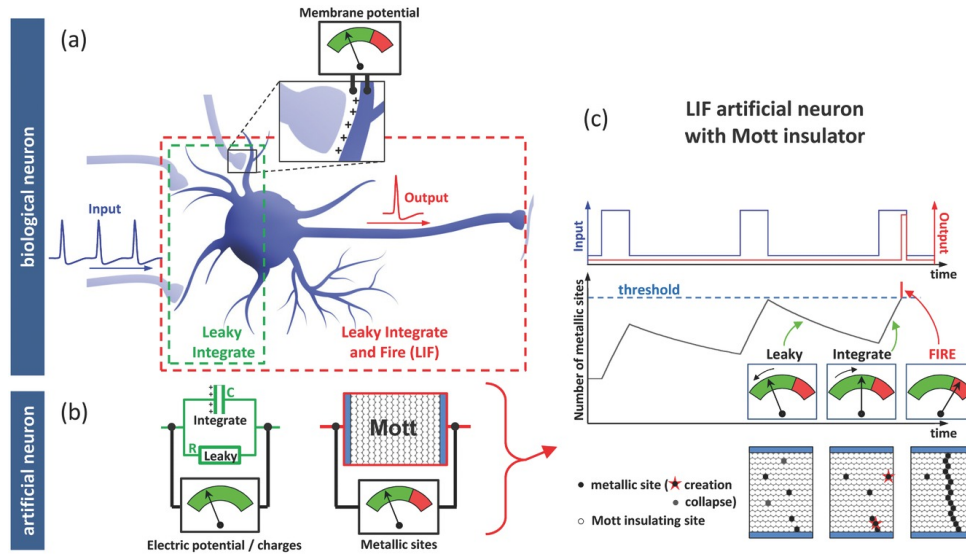


Figure 1.3 – a) Schematic representation of a biological neuron receiving input spikes from other neurons and triggering an output action potential when the membrane potential reaches the threshold value. b) The LIF artificial neurons based on Lapicque’s model reproduce the evolution of the membrane potential thanks to a Resistance Capacitance (RC) circuit accumulating electrical charges. The Mott artificial neuron sketched in panel (c) reproduces the LIF behavior thanks to the accumulation of correlated metallic sites. Taken from [18].

1.3 Neuromorphic materials

Even though CMOS technology can produce full neuromorphic circuits, including artificial neurons and synapses, as discussed in the previous chapter, large capacitors are necessary to form a time constant of the spiking. These capacitors occupy most of the chip’s real estate, limiting scalability. Many reviews attempt to list materials that naturally behave as artificial synapses and neurons (see for example [19, 20, 21, 22].) Below we present selected information useful for the comprehension of this thesis manuscript.

1.4 Non-volatile Switching - Artificial Synapse

In neuromorphic circuits, the device that serves as the equivalent of a synaptor is the memristor, a combination of the words "memory" and "resistor." This type of non-volatile memory can regulate the flow of electrical current and remember the amount of charge that has previously flowed through it [23]. Essential characteristics of memristors for neuromorphic computing, along with comparisons of different switching mechanisms, are discussed in the reviews by Chen et al. [22] and Li et al. [21]. Among the most studied synaptor materials, one can identify the following [20]:

- Oxides (TiO_2 , TaO_2 , HfO_2 , see Table 1.1 for full list);
- Phase Change Memory such as Chalcogenide glasses ($\text{Ge}_2\text{Sb}_2\text{Te}_5$ (GST));
- Ferroelectrics;

— VO₂ ion bombardment, E-field breakdown, gating, thermal coupling.

Oxides

One of the most common methods to achieve non-volatile memory is through the creation and manipulation of nanoscale conductive filaments induced by an electric field. These filaments bridge two metallic electrodes separated by an insulating oxide. Examples of such oxides include hafnium oxide (HfO₂) and titanium dioxide (TiO₂), which exhibit resistance-switching characteristics, scalability, and compatibility with traditional silicon-based circuits. The dynamic adjustment of resistance states in these oxides allows for the storage and processing of information in a manner analogous to the modulation of synaptic strengths. The scalability of these materials ensures that they can be integrated into dense, high-performance neuromorphic architectures, facilitating the development of compact and efficient artificial intelligence hardware. A comprehensive table with materials that are promising for these devices can be found in [20], and a summary is presented in Table 1.1.

MRAM

Magnetoresistive Random Access Memory (MRAM) and Spin Transfer Torque Magnetoresistive Random Access Memory (STT-MRAM) are emerging as pivotal technologies in the realm of neuromorphic devices, which aim to mimic the neural structures and processing capabilities of the human brain. Traditional MRAM utilizes magnetic fields to manipulate the magnetic states of memory cells, consisting of Magnetic Tunnel Junctions (MTJs) where two ferromagnetic layers are separated by an insulating layer [24, 25]. This magnetic state manipulation translates to different resistance levels, enabling data storage.

On the other hand, STT-MRAM advances this concept by employing spin-transfer torque. A typical STT cell includes a non-magnetic layer sandwiched between two nanomagnetic layers, one with fixed magnetization (M_{fixed}) and the other with free magnetization (M_{free}). When a current is injected, spin torque rotates M_{free} , changing the device resistance through the magnetoresistance effect [26]. The magnetizations can be aligned parallel (P state) or antiparallel (AP state) based on current polarity, with SET and RESET processes controlled by sweeping DC currents [27]. STT-MRAM, in particular, stands out due to its lower power consumption and scalability, enabling more compact and efficient neuromorphic architectures. Furthermore, the potential of both MRAM and STT-MRAM to be developed into multistate (or multilevel cell, MLC) memories adds a layer of versatility [28, 29]. This capability is crucial for neuromorphic computing, where the synaptic weights and neural activations are often represented in an analog or multi-level digital form. The multi-resistance states of MRAM and STT-MRAM can closely emulate the variable strength of synapses, thus enabling more accurate and efficient neural network implementations.

Phase Change Memory such as Chalcogenide glasses

Phase Change Material (PCM), particularly utilizing chalcogenide glasses such as $\text{Ge}_2\text{Sb}_2\text{Te}_5$ (GST), is a promising candidate for memristor technology in neuromorphic devices [30]. PCM operates by switching between amorphous and crystalline states, which correspond to high and low resistance levels, respectively. This capability allows PCM to mimic synaptic functions in neuromorphic systems by providing a non-volatile, multistate memory element that can store and process information similarly to biological synapses. The precise control over the resistance states in GST enables the fine-tuning of synaptic weights, essential for learning and adaptation in neuromorphic circuits. Additionally, PCM's high endurance, scalability, and fast switching times make it suitable for the demanding requirements of neuromorphic computing, where rapid and reliable synaptic updates are crucial for real-time processing and learning tasks. Overall, the integration of GST-based PCM in neuromorphic devices enhances their ability to perform complex, brain-like computations with greater efficiency and accuracy.

1.5 Volatile Switching - Artificial Neuron

The second part of neuromorphic circuit are neuristors. A neuristor, a term coined from the combination of the words "neuron" and "transistor," is a device that has been designed to imitate the spiking behavior of neurons. These neuristors have been intended to replicate the complex functions of biological neurons, including the integration and transmission of signals. Most circuits implement a memristor that is often complemented by a Resistance Capacitance circuit to fully emulate neural behavior. This combination emulates the Leaky, Integrate, and Fire (LIF) behavior of biological neurons (Fig 1.3 (a)-(b)). The LIF model mimics the accumulation of electric charge through the cellular membrane, a fundamental function of neuron behavior. Increases in the membrane potential, a direct result of synaptic processes, are typically modeled as current pulses. However, when the voltage reaches a certain threshold, the neuron fires an output electric spike. The nature of this output spike, analogous to the action potential in biological neurons, and the subsequent reset of the capacitor charge is generally not considered part of the model.

New generations of ANN algorithms are being implemented in hardware. Spiking Neural Network (SNNs), which employ spiking neurons based on the LIF model. The primary distinction between SNNs and previous generations of ANNs lies in signal dynamics. SNNs rely on the temporal dynamics (frequency and interval) of binary incoming spikes, whereas earlier models use spatial dynamics (amplitude of the signals) [21, 14, 31, 32]. In SNNs, the inputs are unipolar, time-dependent spike trains that are weighted by synapses and activated by neurons. This process leverages Spike-Timing-Dependent Plasticity (STDP), where synaptic changes are linked to the relative timing of firing events between pre- and post-synaptic neurons. An example of how STDP works is as follows: if a post-synaptic neuron fires a voltage spike after the pre-synaptic neuron, the latter is considered to have directly influenced the depolarization of the former. The

synaptic strength is increased according to the time delay (Δt) between the two firing events, with the increase being most significant when $\Delta t \sim 0$, meaning the post-synaptic neuron fires almost immediately after the pre-synaptic neuron. Conversely, the synaptic strength is reduced if the post-synaptic neuron fires before the pre-synaptic neuron ($\Delta t < 0$). SNNs allow saving energy since they are activated only when an event in the form of a spike occurs. Among the most studied neuristor materials, one can identify the following [20]:

- Metal-insulator transition: Transition metal oxides (vanadates: VO_2 , V_2O_3 ; nickelates: ReNiO_3 ; manganites: LCMO , PCMO ; NbO_2 ; GaTa_4Se_8 ; $\text{NiS}_{2-x}\text{Se}_x$);
- TaO_x [20].

Transition Metal Oxides

Few materials have a neuron-like behavior, but it has been found that Mott insulators allow the implementation of neurons in hardware providing an alternative to traditional silicon capacitors. Even upon miniaturization, Mott materials retain their physical phase transition. Instead of accumulating charges, these insulators accumulate metallic sites which eventually form a pathway in the material to conduct electricity (Fig 1.3 (c)). This process is carried out by a single-component device based on a Mott insulator compound down to the nanometers [33]. Transition metal oxides such as VO_2 , V_2O_3 , NbO_2 and NdNiO_3 undergo a natural Insulator-to-metal transition (IMT) transition, creating a so-called Negative Differential Resistance (NDR) during the transition that is further explained in Chapter 2.

Spin Torque Oscillator (STO)

A large class of oscillators, including Spin Torque Oscillators (STOs) and spin-Hall oscillators, rely on the oscillatory motion of magnetic moments (spins) in ferromagnetic materials. These oscillators utilize magnetic thin films to achieve high-frequency (in the gigahertz regime) and high-Q oscillations. Despite their high oscillation frequency making them excellent candidates for high-speed computing applications and neuromorphic circuits, the interconversion efficiency between electric and magnetic degrees of freedom is relatively low, leading to high power requirements.

STOs perform at high frequencies with low power consumption (10^{-15} J/cycle). The oscillations are driven by the precession of the magnetic moment in a thin magnetic film, excited by a spin-polarized current or the spin Hall effect. This precession alters the device's resistance, and the frequency can be controlled by an alternating current. The primary challenge lies in designing an efficient interconnection scheme. This requires converting magnetic signals to electrical signals and vice versa, or relying on techniques like dipolar or spin wave coupling. One proposed design involves using an RC filter to pick up the STO signal, process it through a summing node, and reconvert it to a magnetic signal via magnetic-field coupling. This conversion typically results in a small voltage signal (mV range). Additionally, demonstrated coupling schemes

show interaction between closely-spaced devices, although this limits system reconfigurability.

1.6 Combining Neuristors and Synaptors on Single Chip

Oxides

Some studies have been able to combine two of these elements on a single chip. Duan et al. [34] implemented a 4×4 fully memristive SNN by integrating volatile NbO_x memristor-based neurons and nonvolatile TaO_x memristor-based synapses in a single crossbar array, showing capabilities in pattern recognition through online learning using a simplified δ -rule and coincidence detection. A simulation based on the experimental of a 3-layer version of the memristive network achieved 83.24% accuracy in classifying MNIST handwritten digits, demonstrating practical application potential.

Coupled STO

Romera et al. [35] successfully trained a compact neural network comprising four STOs to identify spoken vowels. By dynamically adjusting the frequencies of these oscillators through real-time learning mechanisms, they achieved robust synchronization among the devices. This synchronization proved crucial in achieving high recognition rates for the vowel classification task. Their results illustrate the potential of leveraging the inherent oscillatory and synchronization properties of spintronic nano-oscillators in developing efficient hardware implementations of neural networks capable of sophisticated pattern recognition tasks. The description of the network and the recognition results are shown in Fig. 1.4.

In another example, the coupling between STOs is achieved through a combination of MTJs and electrical input signals [36]. This system integrates two MTJs acting as non-volatile magnetic memories (weights) and a larger nanopillar functioning as the STOs(neuron). The coupling mechanism involves programming the MTJs into various resistance states, which modulate the input signals applied to the STO. The resistances of the MTJs change based on their magnetization states (parallel or antiparallel), affecting the current flow through the STO. This current flow, in turn, influences the oscillation behavior of the STO, enabling it to perform complex computational tasks required in neuromorphic computing.

Silicon Photonics

The process of creating artificial neurons and synapses using Vertical Cavity Surface Emitting Lasers (VCSELs), Mach-Zehnder Modulator (MZMs), and PCMs involves several integrated steps on a silicon photonic chip [37]. It begins with VCSELs generating continuous laser light. This light is then modulated into precise optical pulses using MZMs, which split the light into two paths, apply a varying electrical signal to create interference, and recombine the light, thereby

modulating its intensity, phase, or frequency. These optical pulses travel through waveguides, which direct and shape them, ensuring they reach the synaptic components. The pulses then interact with PCMs such as GST integrated into the waveguides. The GST switches between amorphous and crystalline states when exposed to optical pulses; a short, intense pulse melts the GST to the amorphous state, and a longer, moderate pulse crystallizes it back. This state change alters the optical properties of the GST, effectively adjusting the synaptic weight, simulating the synaptic strength adjustments in biological synapses during learning. The learning process, **STDP**, is implemented by controlling the timing of optical pulses; if a pre-synaptic pulse arrives just before a post-synaptic pulse, the synaptic weight increases (potentiation), and if it arrives just after, the synaptic weight decreases (depression). This integration of light generation, modulation, and synaptic learning on a single chip facilitates efficient, high-speed neuromorphic computing.

The architectures above all present state of the art in implementing fully integrated neuromorphic systems in various fields. Although outstanding, their design remains complex and utilizes many materials. Finding a single material that can perform both functions remains an ongoing challenge. Interestingly, TaO_2 [20] and TaO_x [38] have been used in artificial synapses and neurons independently but have not been integrated on the same chip. This is probably due to the fact that the spiking behavior found in TaO_x is not due to a metal-insulator transition but rather from a rapidly changing insulating state with temperature [38].

In the following sections, we will elaborate on why VO_2 is considered an excellent single-material candidate and explain the reasons for focusing on this material throughout the majority of this thesis.

Why vanadium Dioxide?

Vanadium dioxide (VO_2) distinguishes itself among the transition metal oxides considered for neuromorphic devices due to its impressive **IMT** near room temperature and neuristor-like spiking behavior. Furthermore, its demonstrated synaptic memory capabilities make it a material of significant interest in the field of neuromorphic computing.

VO_2 as a neuristor

Vanadium dioxide has potential for constructing neuristors capable of performing basic spiking and other neuron functions, such as activity, **LIF**, reset, and rate coding. Del Valle et al. [53] demonstrated that the Joule heating-induced IMT in VO_2 (explained with more details in the following chapters) nanogaps can mimic these neuron functionalities by sending a train spikes in a controlled manner (Fig. 1.5.) Another report explored "thermal VO_2 neuristors" application in spiking oscillators to achieve reconfigurable electrical dynamics similar to those on biological neurons [33].

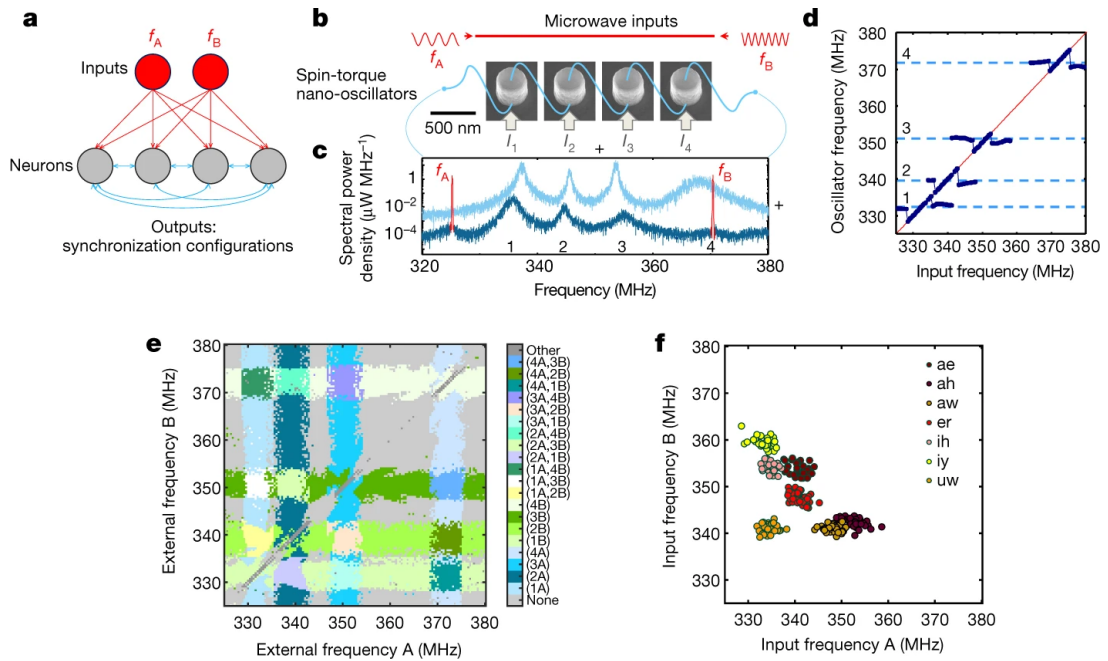


Figure 1.4 – a) Schematic of the emulated neural network. (b) Experimental setup featuring four spin-torque nano-oscillators connected in series and coupled through emitted microwave currents. Two microwave signals, f_A and f_B , encode inputs via a strip line, generating microwave fields. Total oscillator network output is recorded using a spectrum analyzer. (c) Microwave output from the oscillator network: light blue shows emissions without, and dark blue with, applied microwave signals. Peaks correspond to oscillator emissions; narrow red peaks denote input frequencies f_A and f_B . (d) Evolution of oscillator frequencies as external source A frequency varies. Oscillators phase-lock to inputs near their natural frequencies, aligning their outputs with input frequency during locking. (e) Experimental synchronization map based on external signal frequencies f_A and f_B , illustrating different synchronization states. (f) Inputs applied to the system depicted in the (f_A , f_B) plane, where each color represents a different spoken vowel associated with various speakers' data points (Taken from [35].)

Table 1.1 – Examples of materials and devices for Resistive Switching-based non-volatile memory for neuromorphic computing based on [20]

Material/ System	Device Structure	RS Mechanism	Key Characteristics	ref
HfO ₂	Pt/HfO ₂ /TiN	Filamentary (Oxygen vacancies)	Low power, good endurance	[39, 40]
TiO ₂	Pt/TiO ₂ /Pt	Filamentary (Oxygen vacancies)	Simple structure	[41, 42, 43]
Ta ₂ O ₅	Pt/Ta ₂ O ₅ /Ta	Filamentary (Oxygen vacancies)	Multilevel switching, high speed	[44, 45]
Ag ₂ S	Ag/Ag ₂ S/Pt	Filamentary (Metal migration)	Low power, high switching speed	[46]
NiO	Pt/NiO/Pt	Filamentary (Oxygen vacancies)	High endurance, good retention	[47, 48]
SiO _x	Poly-Si/ poly-Si	Filamentary (Metal migration)	CMOS compatible, high speed	[49]
SrTiO ₃	Pt/SrTiO ₃ /Nb:SrTiO ₃	Interface-type	High endurance	[50]
Graphene oxide	Au/Graphene oxide/ITO	Filamentary (Oxygen vacancies)	Flexible, transparent	[51]
WO _x	Pt/WO _x /Pt	Filamentary (Oxygen vacancies)	High endurance, good retention	[52]

Another neuromorphic computing paradigm is Oscillatory Neural Network (ONNs). Those networks draw inspiration from the collective synchronization of human brain neurons through oscillations, leveraging phase computing where information is encoded in the phase relationship between oscillators [54]. VO₂ acts as an oscillator neuron within ONNs, enabling the creation of energy-efficient and compact neural networks. For instance, binary information can be represented by the phase difference between oscillators, enhancing the robustness to noise and energy efficiency since they can potentially limit voltage amplitude [55].

Yi et al. [56] reported that VO₂ neurons possess various excitability classes and can emulate biological neuronal dynamics, demonstrating their potential for neuromorphic cortical computing. Khandelwal et al. [57] highlighted the superior energy conversion coefficients of VO₂ neuristors due to their significant contrast in resistance, optical refractive index, and density during the IMT, making them viable alternatives for micro-electromechanical systems (MEMS) applications. Nunez et al. [58] proposed an architecture for ONNs using VO₂-based nano-

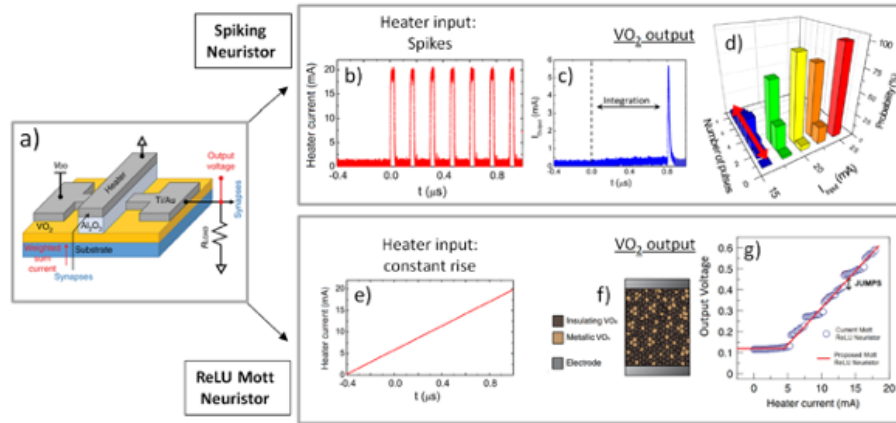


Figure 1.5 – (a) Caloritronic Neuron refers to a type of artificial neuron that uses the thermoelectric effect to generate electrical signals. In this design, a VO_2 junction is placed under a Ti(titanium) heating strip above it. Spiking neuron: (b) Spikes, or brief pulses of electrical activity, are used as input and pass through the Ti heating strip. (c) As the input spikes pass through the Ti heating strip, heat build up which causes the VO_2 junction to switch between its insulating and metallic states, generating an output spikes in the process. (d) Histograms of the integration time (time it takes for the output spike to occur), as a function of input pulse amplitude may show strong variability, as indicated by the red arrow (adapted from [53]). ReLU Mott Neuron: (e) The Ti strip is heated progressively in this configuration. (f) As the Ti strip heater heats up, the VO_2 junction changes from an insulator to a metal state. This process happens progressively, with small patches switching in the VO_2 junction. (g) The resulting output current from the VO_2 junction is used to generate a ReLU(Rectified Linear Unit) curve. This curve can show sudden changes in the output current, as some patches switch abruptly due to local IMT avalanches. These jumps can increase as the device size is reduced (adapted from [59]).

oscillators, emphasizing robustness and tolerance to device variability for pattern recognition applications.

VO_2 as a synaptor

The IMT in VO_2 has been extensively utilized in memristors [60, 56, 61, 62]. This transition enables VO_2 to switch between two distinct phases with vastly different electrical properties. Recently, new methods for creating microscopic synapse-like connections in VO_2 have been explored, including ion bombardment, electrical field breakdown, gating, and thermal coupling (Fig. 1.6). Ghazikanian et al. [63] have shown that the location and shape of filaments form through percolating during the IMT under an electric field, and results in large resistance changes, are influenced by hard-to-control parameters, such as grain boundaries or intrinsic defects, making the switching process susceptible to cycle-to-cycle and device-to-device variation. By using focused Ga^+ ion beam irradiation to selectively engineer defects in VO_2 and V_2O_3 thin films, they demonstrated control over the position and shape of metallic filaments, significantly

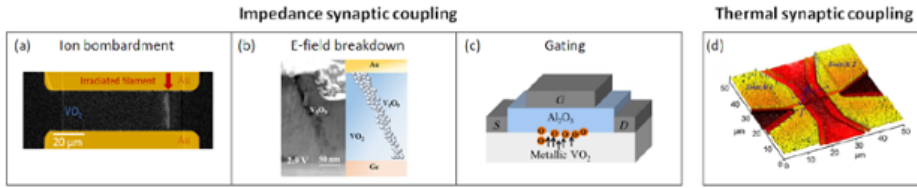


Figure 1.6 – Various recent methods to create synaptors in VO_2 . Ohmic impedance coupling, achieved through (a) ion bombardment [63], (b) E-field breakdown [64], and (c) three terminal gating. Full impedance coupling using breadboard resistors and capacitors [65]. (d) Thermally induced coupling has been achieved using two VO_2 neuroresistors separated by $12\mu\text{m}$ [33, 66].

reducing the switching power in these materials. Cheng et al. [64] have focused on the IMT in VO_2 and its resistive switching properties. They used in situ transmission electron microscopy, electrical transport measurements, and numerical simulations on $\text{Au}/\text{VO}_2/\text{Ge}$ vertical devices to study the electroforming process. They observed the formation of V_5O_9 conductive filaments with a pronounced IMT and found that vacancy diffusion can erase the filament, allowing the system to "forget."

Anouchi et al. [65] demonstrated a nonvolatile memristive three-terminal transistor based on VO_2 . An ultrathin VO_2 layer was incorporated into a metal-oxide-semiconductor field-effect geometry using alumina as the gate dielectric. They demonstrated that the channel's resistance could be modified in a nonvolatile and reversible fashion through the field effect, contingent on the gate voltage being applied at the metallic state of VO_2 . This study provides a proof of principle for developing high-performance electronic synaptic transistors utilizing Mott materials, which simplify fabrication and enable integration with silicon-based architectures.

While each method marks significant progress, major challenges remain:

- Ion bombardment is tunable but not rewritable and requires sophisticated material preparation [63].
- Electrical field breakdown is easily achievable in any device but is not reconfigurable or tunable due to the uncontrolled stochasticity in filament formation [64].
- Gating devices are slow and heavily dependent on sample quality, relying on electric-field-induced ion motion towards interfaces [65].
- Thermal coupling is not reconfigurable, being fixed by the initial sample lithography [66, 33].

Thus, developing new microscopic methods that are tunable, non-stochastic, fast, and reprogrammable is essential to truly mimic analog synapse behavior in VO_2 and other transition metal oxides.

As such, VO_2 can emulate the dynamic behavior of neurons and synapses, contributing significantly to the development of devices that can learn and adapt in manners akin to the human brain, marking a significant milestone in the field of neuromorphic computing.

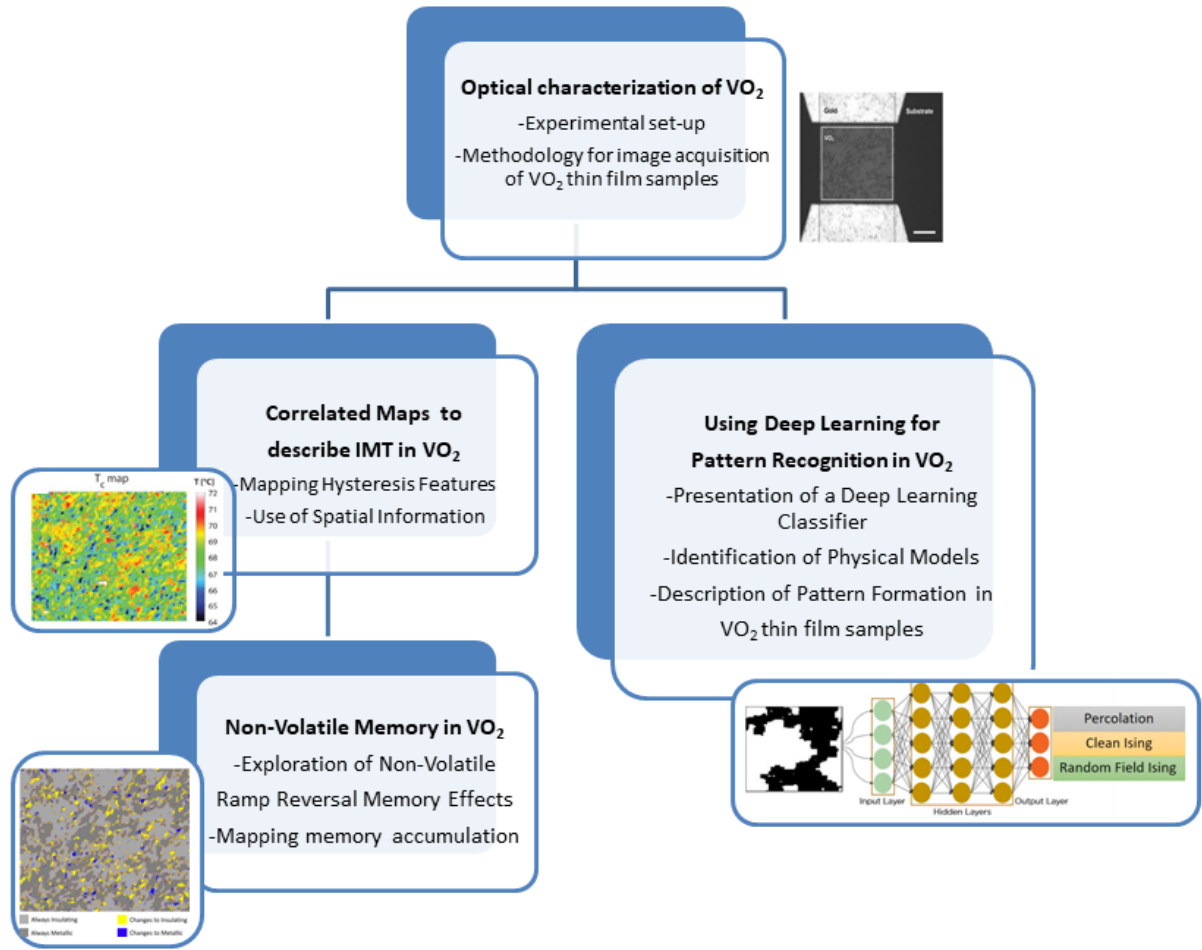


Figure 1.7 – a) Schematic illustrating the scope of the thesis

2 Aim of the thesis

The aim of this thesis is to investigate the insulating-to-metal transition (IMT) in vanadium dioxide (VO₂) and explore its potential applications in neuromorphic computing. By building a new optical characterization method for VO₂, this work seeks to bridge the gap between traditional electrical and surface probes measurements, and incorporate spatial information that facilitates the tailoring of devices and enhances the understanding of material behavior during its phase transition. The thesis aims to deepen the understanding of VO₂ IMT and how this material can be utilized to emulate biological neural networks, particularly how to create and understand non-volatile memory in VO₂, hence contributing to the development of novel computing paradigms that mimic the functionality of the human brain (Fig 1.7.)

Furthermore, this thesis explores machine learning techniques to analyze and interpret the complex patterns observed in VO₂ during its phase transition, with the help of Prof. Erica Carlson's group. By implementing a deep learning classifier, the study aims to identify underlying physical models and diagnose the proximity to criticality in quantum materials. The integration

of spatial information and temperature protocols in the study of non-volatile memory in VO₂ also aims to provide new insights into the mechanisms of memory in this material. Overall, this research aspires to contribute i) to the broader field of quantum materials by offering novel methodologies and perspectives on the IMT in VO₂; ii) to the field of machine learning by providing new applications in materials physics; and iii) to the neuromorphic computing field by providing a new characterization method that extracts features of VO₂ thin films that are relevant for tailoring the performance of devices.

Objectives

- Develop a new optical technique to track phase separation during the VO₂ insulator-to-metal transition.
- Use this new method to investigate ramp reversal memory, a new procedure to create synaptic memory in VO₂.
- Use a large dataset of fractal images generated by this new optical technique to demonstrate how machine learning (ML) help understand the physical interactions present in the system.

Here is the structure followed to accomplish the aim of the thesis:

Chapter 1: Introduction

The first chapter contextualizes the study of VO₂ for artificial intelligence, discusses VO₂ potential as neuristors and memristors, and presents the scope of this thesis.

Chapter 2: Background on the Insulating-to-Metal Transition in VO₂ and Machine learning

In this chapter, we introduce the insulating-to-metal transition (IMT) in VO₂ and explore the characteristics that make this material compelling for applications in neuromorphic computing. We review various characterization methods to study the dynamics of VO₂ IMT. The second part of this chapter is devoted to define machine learning and deep learning techniques, like convolutional neural networks, and how those these tools are promising in the field of materials science, in particular for image processing and pattern recognition.

Chapter 3: Optical Characterization of VO₂

This chapter describes the setup used to characterize VO₂ thin film samples, detailing the hardware and software employed during the automated experimental acquisition of images capturing the IMT in VO₂. We outline the post-experiment image processing workflow used to align images and track the IMT over time to determine the local critical temperature.

Chapter 4: Correlated Maps to Describe IMT in VO₂

Following the methodology described in the previous chapter, we extract various features of the IMT from single-pixel time traces. Here, we demonstrate how spatial information allows us to map hysteresis features and how optical characterization complements traditional electrical

measurements in studying the IMT. Also, we present examples for VO₂ thin film samples synthesized with different methods.

Chapter 5: Non-Volatile Memory in VO₂

Building on the spatial information obtained during the VO₂ IMT, we applied a temperature protocol known as Ramp Reversal Memory, which permits observing the effect of non-volatile memory in VO₂. We mapped the accumulation of metallic and insulating patches coexisting near criticality and explored how this aids in understanding the mechanisms behind memory in this material. This chapter combines both electrical and spatial information to study memory in VO₂.

Chapter 6: Using Deep Learning for Pattern Recognition in VO₂

Many quantum materials exhibit interesting fractal patterns near criticality. This chapter presents a deep learning classifier designed to identify a physical model that describes pattern formation in VO₂. This approach is promising for diagnosing proximity to criticality in quantum materials that exhibit a clear phase separation.

Conclusions and future work

In the final chapter, we summarize the key findings and contributions of this thesis. We present the IMT in VO₂ and its potential for neuromorphic computing applications. We discuss how optical characterization techniques can contribute to a comprehensive understanding of VO₂ properties. The chapter also shows the interdisciplinary approach combining material science and machine learning using a deep learning classifier to study the underlying physics driving VO₂ IMT. This chapter aims to provide a direction for future studies that can build upon the results of this thesis.

Chapter 2

Background on the Insulating-to-Metal Transition in VO₂ and Machine learning

The first part of this chapter gives insights into the insulator-to-metal transition (IMT) in vanadium dioxide (VO₂), detailing its impact on electrical and optical properties. We begin by discussing the fundamental aspects of the IMT, including the associated thermal hysteresis and structural phase changes. Next, we delve into various fabrication methods for VO₂ thin films, with a focus on RF magnetron sputtering and sol-gel techniques. Finally, we examine the characterization methods used to study VO₂, emphasizing optical techniques and their role in understanding phase transitions and inhomogeneities at different scales.

1 IMT in VO₂ films

Vanadium dioxide (VO₂) is a canonical strongly correlated material that exists in various polymorphic phases [68]. One of its most intriguing characteristics is the reversible IMT coupled with a structural phase transformation. This transformation occurs as VO₂ changes from a low-temperature insulating phase (VO₂(M)) to a metallic phase (VO₂(R)) near room temperature ($T_c \approx 340$ K).

The IMT leads to sudden changes in physical properties such as resistivity and optical transmittance [69, 70]. VO₂ has been proposed for use in thermochromic window elements with switchable infrared reflectivity, functioning as "smart windows"[71, 72]. These windows increase heating and air-conditioning efficiency by being infrared-transparent at low temperatures and infrared-reflective at higher temperatures, without compromising visible light transparency. Another promising application is the Mott field-effect transistor [73], which can switch between insulating and metallic phases via gate voltage application, ideally with fast turnover. Additional practical applications of VO₂ include thermally sensitive switching, infrared switching [74], infrared polarizers [75], fiber optic waveguides, optical data storage media[76], and electro-optical sensing elements [77].

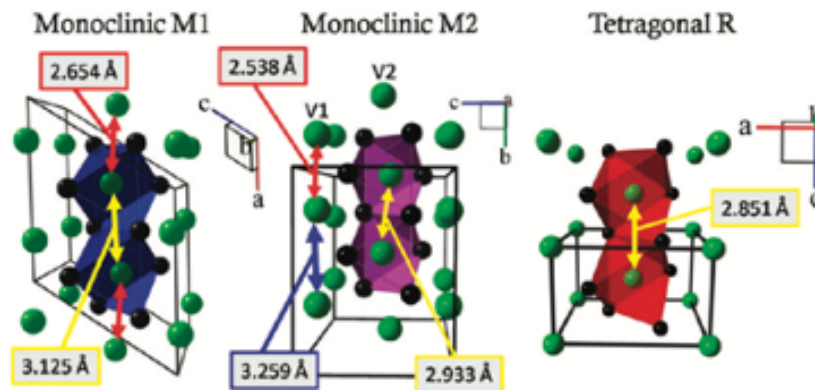
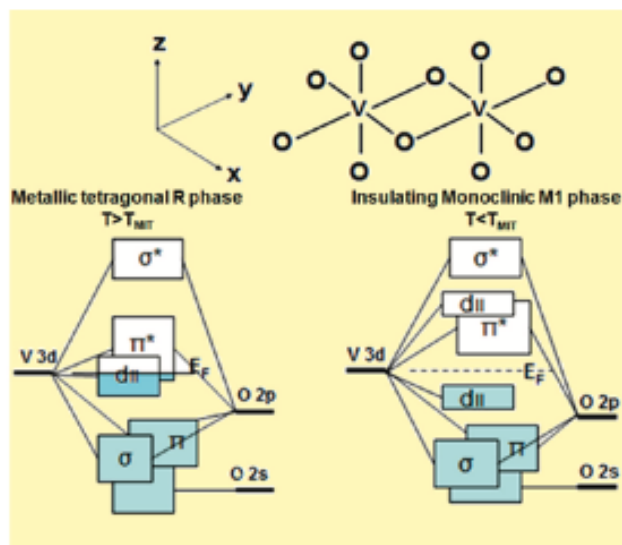
(a) Crystal structures**(b) Electronic structures**

Figure 2.1 – (a) Schematic depictions of the crystal structures of the low-temperature monoclinic M1, intermediate M2, and high-temperature tetragonal rutile R phases. V-V distances are highlighted. (b) Molecular orbital diagram depicting the electronic structure of the monoclinic and tetragonal phases of VO₂. The left MO diagram corresponds to the undistorted metallic phase of VO₂, whereas the diagram on the right shows the altered MO diagram upon transition to the distorted insulating phase of VO₂. Taken from [67].

Structural phase transformation

Above the transition temperature (T_c), VO₂ exhibits a rutile tetragonal structure where each vanadium atom is connected to six adjacent oxygen atoms, forming an octahedral shape (Fig. 2.1(a)). This metallic R-phase belongs to the P₄2/mnm space group, characterized by lattice parameters $a = b = 4.553\text{\AA}$ and $c = 2.849\text{\AA}$ [78]. The c/a ratio is smaller than that of an ordinary rutile compound, bringing the vanadium atoms closer along the c -axis, with V-V distances of approximately 2.85\AA [67][79].

Below T_c , VO₂ adopts a monoclinic crystal structure (Fig. 2.1(a)) in the P₂₁/c space group, with lattice parameters $a = 5.75\text{\AA}$, $b = 4.52\text{\AA}$, $c = 5.38\text{\AA}$, and $\beta = 122.60^\circ$ [78]. This transition, which is first-order with a latent heat of about 1020 cal/mol, involves a significant reduction in symmetry. The insulating state is marked by a zigzag arrangement along the c -axis due to the breaking of overlapping bonds, leading to a band gap change from 0 to 0.65 eV [80]. During this transition, the unit cell doubles in size due to the pairing and tilting of the VO₆ octahedra along the c -axis, resulting in the monoclinic M1 phase with distinct V-V bond distances of 2.65 and 3.12 Å[81].

Mechanistic aspects of phase transformation

Since its discovery in 1951 by Morin [82], there is a debate between which mechanism describes the best this phase transition: The Peierls model and Mott-Hubbard model [83]. The Peierls model explains that the structural distortion enhances the bonding between neighbouring V atoms due to the change in the V-V dimers distance in the polymorphs passing from a localized d-orbital in the V-V dimers in VO₂(M) to a shared-orbital between all vanadium atoms in VO₂(R) (Fig. 2.1(b)). Alternatively, the Mott-Hubbard model states that MIT would occur when the electron density(n_e) and Bohr radius(a_H) satisfy $n_e 1/3a_H \approx 0.2$ and gives more emphasis to the abnormal low conductivity in the metallic phase. Since this transition is very fast (few picoseconds) both theories are advised to explain it.

It is still unclear whether the structural phase transformation is necessary for the electronic metal-insulator phase transition. However, current evidence suggests that the two phenomena might be independent if the material achieves a sufficient carrier density. In other words, a metallic phase could potentially be induced without a structural phase transformation if the excitation of carriers through optical, thermal, or gate-voltage methods reaches a certain threshold density. This finding is crucial for understanding the nature of the phase transition [67].

1.1 Electrical properties of the IMT

Depending on the VO₂ films, the IMT results in a resistivity change of several orders of magnitude (Fig. 2.2 (a)). There are several stimuli that can induce the IMT. Here, we are going to discuss how thermal and electrical triggers, and different kind of irradiations affect the

electrical properties on VO₂.

Thermally-induced phase transition

The IMT in VO₂ happens as a function of the temperature, so naturally the first method described is a thermal induction. When applying a temperature sweep, we can induce the IMT on VO₂ films, by changing the phase when temperature goes beyond the specific T_c , and conversely, cooling down from a higher temperature. One characteristic of the thermally induced IMT in VO₂ is thermal hysteresis, which is a common feature of first-order phase transitions [84]. This phenomenon is observed in both the resistance and optical properties of VO₂ when the temperature is cycled across the T_c in both heating and cooling branches [85]. The hysteresis width can range from a few degrees to tens of degrees in macroscopic materials and can be less than 1°C in single crystals [86]. Factors such as the crystalline structure (single crystal vs. polycrystalline), presence of defects, and doping affect hysteresis width [87, 88, 89].

Electrically-induced phase transition

Several studies support the theory that the electrically-driven phase transition in VO₂ is triggered by Joule heating. Mun et al. [90] and Radu et al. [91] demonstrated that increased ambient temperature reduces the power needed for the transition, indicating a temperature-triggered process. Lee et al. [92] found similar results using low-frequency input signals. Zimmers et al. [93] used fluorescent particles to monitor local temperature, finding it consistent with the expected phase transition temperature of 68°C, showing that the transition mainly has thermal origin.

However, some evidence suggests a non-thermal transition mechanism. Gopalakrishnan et al. [94] proposed that the phase transition occurs below the critical temperature, with Joule heating subsequently raising the temperature above T_c . Fast voltage or light pulse measurements [95, 96] suggest a transition too rapid for a thermal process. The phase transition often proceeds through filament formation [97], with Li et al. [98] showing filament temperatures can reach T_c . Aetukuri [99] argued that insulating resistance dependence on temperature supports a Joule heating mechanism.

Recent studies, such as Kalcheim et al. [100], suggest defects play a crucial role. They found that in high-quality VO₂ nanowires, the transition is temperature-driven, but in defected wires, the transition occurs before reaching T_c , likely due to the Poole-Frenkel effect. This indicates that the phase transition mechanism in VO₂ devices remains unclear, especially for those on lattice-mismatched substrates where defects significantly impact the IMT.

Photo-induced phase transition

A number of studies demonstrate that the application of different types of irradiation, including electron beams[101], X-Rays[102], and UV light[103, 104, 105], can alter the electrical

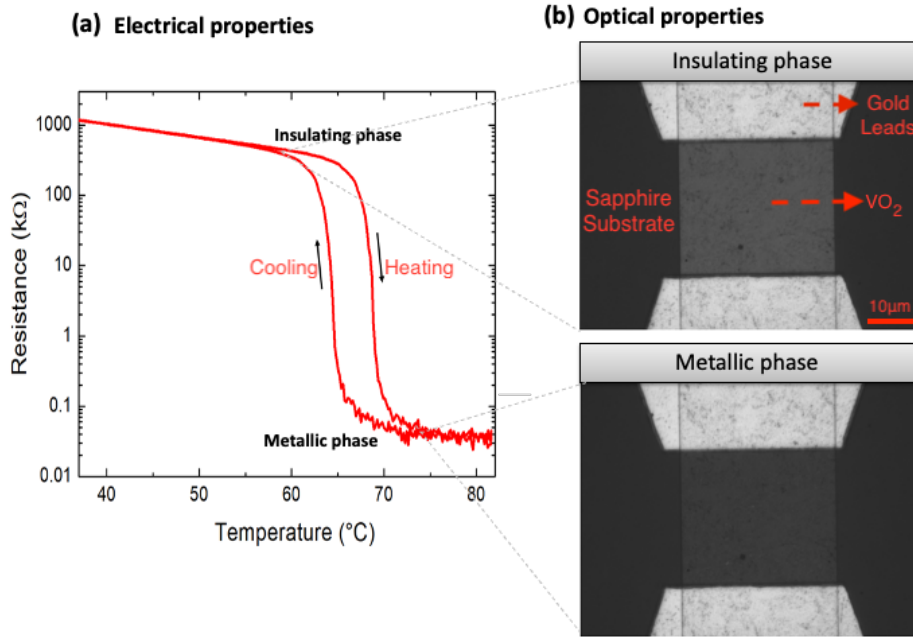


Figure 2.2 – (a) Hysteresis graph depicting the drop in resistance upon the IMT in a VO_2 thin film. (b) Micrographs of the VO_2 samples used for the experiment of the present work. There is a color change between the insulating (light gray) and metallic phases (dark gray).

properties of VO_2 . In the context of in-sensor computing, Li et al. in [104] engineered VO_2 films with oxygen stoichiometry under UV irradiation to achieve non-volatile, multi-level control. This enabled the creation of a neuromorphic UV sensor that integrates sensing, memory, and processing at room temperature, proving its potential for silicon-compatible and wafer-scale integration. The sensor demonstrated linear weight updates with optical writing, increasing metallic phase proportion nearly linearly with light irradiation. An artificial neural network using this sensor improved recognition accuracy from 24% to 93%, highlighting the potential for advanced neuromorphic vision systems.

Dietze et al. [102] observed a significant resistivity decrease in VO_2 upon localized X-ray illumination at room temperature, without transitioning to the high-temperature tetragonal phase. The transition reverted over tens of hours at room temperature but fully recovered in minutes with thermal cycling. This behavior was modeled using random local-potential fluctuations and discrete recombination sites, shedding light on residual photoconductivity mechanisms in VO_2 . Zhang et al. [101] demonstrated that focused electron beam irradiation could lower the IMT temperature of VO_2 nanowires to room temperature without prepatterning. This radiolysis-assisted IMT (R-IMT) technique created a gradual IMT zone several times the beam size, allowing precise control over the metal/insulator phase ratio. This process offers potential for precisely engineering nanodomains with diverse electronic properties in functional material-based devices, promising advancements in renewable energy, information storage, and sensor technologies.

Wegkamp et al. [106] investigated the ultrafast dynamics of the photoinduced phase transition (PIPT) in VO₂ from monoclinic insulator to rutile metal. Using femtosecond time-resolved photoelectron, optical, and coherent phonon spectroscopy, they disentangled electronic and crystallographic contributions to the IMT. Their findings highlighted two non-equilibrium dynamics branches: an instantaneous collapse of the insulating gap and a lattice potential symmetry change initiating the crystallographic transition. They proposed that the PIPT threshold in optical experiments is likely driven by lattice potential changes rather than the IMT itself, predicting a transiently metallic, monoclinic state of VO₂ that decays on ultrafast timescales.

Note that various methods have also been able to change the IMT on VO₂, such as ion bombardment [107], electrical gating [108], strain [109], and doping [89].

Current-Voltage Characteristics of Coplanar VO₂ Devices

To analyze the current-voltage (I-V) characteristics of VO₂ devices, we focus on coplanar devices whose architectures are similar to those studied in this thesis (Fig. 2.2).

In 1971, Duchene et al. [110] introduced a coplanar VO₂ device structure consisting of a VO₂ film on a substrate with metallic electrodes separated by gaps of 30 – 200 μm. The I-V characteristics of these devices exhibit two distinct regions: a linear pre-switch region and a nonlinear switched region. The latter is caused by Joule heating, which leads to electrothermal instability and dynamic equilibrium at lower voltages. Most of the current flows through a highly conductive thermal filament in the high-temperature phase of VO₂, **which can be optically observed due to a significant change in the refractive index.**

Figure 2.3 shows a classic non-equilibrium example of I-V curve of a VO₂ device. Initially, the device is in its insulating state, acting as a high impedance resistor. As the applied voltage increases, the power dissipated as Joule heat raises the local temperature of the device. Upon reaching a threshold voltage (V_{TH}), the device undergoes an insulator-to-metal transition. During this transition, the measured voltage decreases even as the current increases, a characteristic of negative differential resistance (NDR) [111]. NDR occurs when an increase in voltage results in a decrease in current through the device. After the transition, the device stabilizes at a low resistance value. When the applied voltage is subsequently lowered, the device reaches a threshold voltage (V_{TL}) for the metal-to-insulator transition, switching back to its high impedance state.

The stability of the switching properties in VO₂ coplanar devices is influenced by an interface layer between the VO₂ film and substrates like quartz or sapphire. This layer, typically 500 – 1000 Å thick, consists of VO₂ doped with substrate metal atoms [112]. For thin films on sapphire substrates, this interface layer does not affect the conductivity transition. The stability of electrothermal switching is correlated with the electronic state of the film-substrate interface.

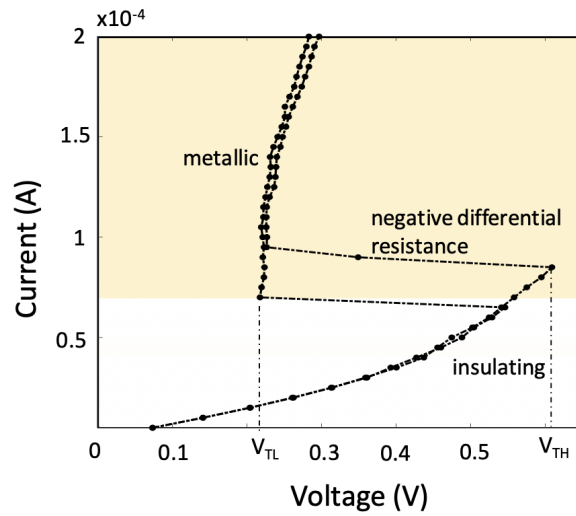


Figure 2.3 – The current vs. voltage characteristic of a VO₂ device presents three regions: at first, the device is in its insulating state. As the voltage drop across the device is high enough to trigger the phase transition, the material undergoes the phase change and a negative differential resistance regime is formed. Lastly, the device stabilizes in its metallic state. The measurement was conducted sourcing a current and measuring the voltage across a VO₂ device. Taken from [113].

Thus, quartz substrates exhibit stable switching due to a well-delocalized interface, while sapphire substrates show unstable switching with irreversible changes due to localized electronic states [112].

Optical properties of the IMT

In our study, we observed a reflectance difference of 20-30% between the insulating and metallic phases of VO₂, enabling far-field optical characterization. This difference was also noted by Currie et al. in the visible spectrum (red curve representing the insulating phase before the IMT and green curve representing the metallic phase after the IMT). Temperature-dependent optical transmittance and reflectance measurements were performed in [114] using a broad-spectrum source with coarse temperature intervals (10°C), as shown in Fig. 2.4(a). Additionally, measurements at a single wavelength (1550 nm) with finer temperature resolution (<1°C) were conducted to capture optical hysteresis more precisely, as illustrated in Fig. 2.4(b).

The most significant changes in optical transmittance and reflectance occurred in the infrared region, as shown in Fig. 2.4(a). Due to spectra weight conservation, in the visible region, the optical transmittance and reflectance exhibited a small change opposite to the infrared trends. In Fig. 2.4(b), the slope of the phase transition during heating becomes steeper as the film thickness increases from 8.6 to 30 nm.

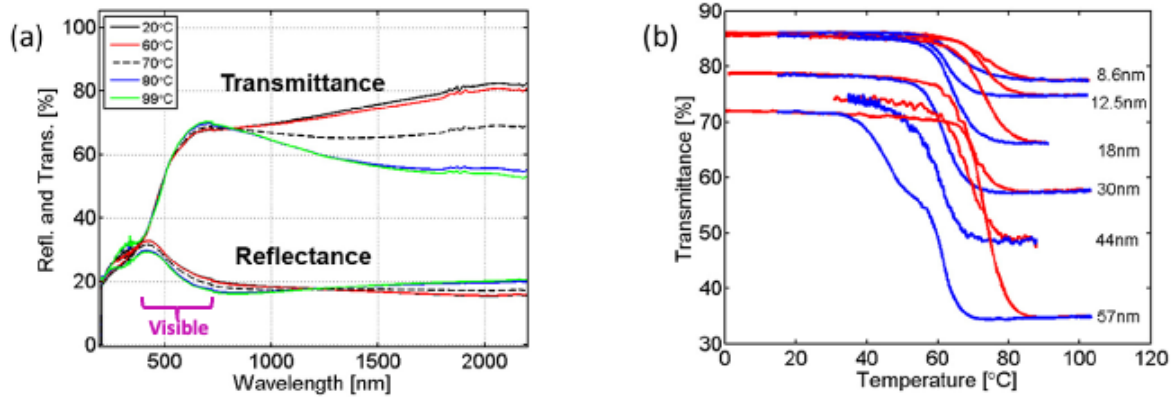


Figure 2.4 – (a) Temperature-dependent optical reflectance and transmittance spectra for the 30-nm VO₂ film thickness for temperatures of 20, 60, 70, 80, and 99°C. (b) Optical transmittance at 1550nm for 8.6, 12.5, 18, 30, 44, and 57-nm VO₂ film thicknesses shows the hysteretic nature of the transition (red: heating, blue: cooling) . Taken from [114].

1.2 Fabrication methods of VO₂ thin films

For some VO₂ thin films practical applications, they must exhibit sharp hysteresis loops, high transition contrast, and significant resistance drops during the IMT. However, achieving these desirable characteristics is often hindered by phase inhomogeneity due to non-stoichiometry and interfacial mismatch between the film and the substrate. Depending on the application, phase inhomogeneity can also be explored since it can broaden the hysteresis loop and reduce the transition contrast. In this section, we briefly introduce fabrication methods for VO₂ thin films.

RF Magnetron Sputtering

RF magnetron sputtering is a widely used technique for depositing VO₂ thin films [115]. In this method, Argon ions are accelerated by an RF electric field to bombard a vanadium target, causing the ejection of vanadium atoms which then deposit onto the substrate to form a thin film. This method has been shown to produce high-quality films with good control over thickness and composition, although it requires careful optimization to minimize phase inhomogeneity and interfacial mismatch.

- Precursors: Typically, a high-purity vanadium target is used.
- Substrates: Common substrates include quartz, sapphire, and silicon. The choice of substrate affects the film’s crystallinity and phase purity.

Key Parameters:

- RF Power: Influences the sputtering rate and energy of ejected atoms.

- Argon Gas Pressure: Affects the mean free path of sputtered atoms and their deposition rate.
- Substrate Temperature: Critical for ensuring proper film crystallization and stoichiometry.
- Oxygen Partial Pressure: Essential to achieve the correct oxidation state of vanadium.

Sol-Gel Method

The sol-gel method is a solution-based technique involving the preparation of a vanadium-containing sol, which is then deposited onto the substrate and transformed into a gel [81]. This gel is subsequently dried and annealed to form a crystalline VO₂ film. The sol-gel method offers several advantages, including low-cost and large-area film production. It allows for precise control over the chemical composition and stoichiometry of the films. However, the quality of the films can be highly dependent on the precursor materials, the pH of the sol, the deposition conditions, and the annealing parameters. Proper optimization is required to achieve films with sharp IMT characteristics and minimal defects.

- Precursors: Common precursors include vanadium alkoxides, vanadium chloride, and vanadium acetylacetonate.
- Substrates: Typically, silicon wafers, glass, and sapphire substrates are used.

Key Steps:

- Sol Preparation: Mixing the vanadium precursor with a solvent (e.g., ethanol) and stabilizing agents.
- Deposition: Techniques like spin-coating or dip-coating are used to apply the sol onto the substrate.
- Gelation: The sol transitions into a gel as it undergoes hydrolysis and condensation reactions.
- Drying and Annealing: The gel is dried to remove the solvent and annealed at high temperatures to form crystalline VO₂.

Chemical Vapor Deposition (CVD)

CVD involves the reaction of vapor-phase chemicals to deposit solid thin films on a substrate [72].

- Precursors: Vanadium oxytrichloride (VOCl₃) and oxygen.
- Substrates: Commonly used substrates include silicon and sapphire.
- Key Parameters: Reaction temperature, gas flow rates, and chamber pressure.

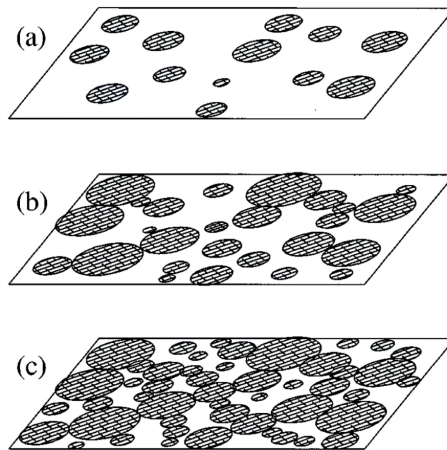


Figure 2.5 – Schematic diagram of the IMT in the VO₂ film. (a) The metallic domains start to form nucleation droplets in the film surface sporadically, as T approaches T_c . (b) The domains grow larger and start to form clusters as T increases further. (c) Above T_c , the metallic domains form an infinite cluster. Taken from [134].

Pulsed Laser Deposition (PLD)

PLD utilizes a high-energy laser pulse to ablate a target material, which then deposits onto a substrate [116].

- Targets: Various target materials can be used, including vanadium metal, V₂O₅, and VO₂.
- Substrates: Quartz, silicon, and sapphire.
- Key Parameters: Laser energy, pulse frequency, oxygen pressure, and substrate temperature.

1.3 Characterization methods to study VO₂ IMT

Optical studies of phase-separated systems, such as VO₂, are complex due to their inherent inhomogeneities [135]. Advances in infrared (IR) and optical microscopy have enabled imaging of phase-separated regions in strongly correlated materials [84, 136]. Nanometer-scale inhomogeneities can be detected using near-field techniques, which achieve spatial resolutions of 8–10 nm, below the diffraction limit [118, 137]. The highest spatial resolution in infrared experiments is achieved using near-field instruments based on atomic force microscopes coupled to IR lasers, which can probe local conductivity at the nanoscale, but limited to a few scans. For larger inhomogeneities and tracking fractal patterns, on the order of tens of microns, conventional microscopy is effective.

Macroscopic probes

Historically, many studies have described the thermal hysteresis observed in VO₂ systems, but the dynamic evolution, such as spinodal decomposition and domain growth, received lit-

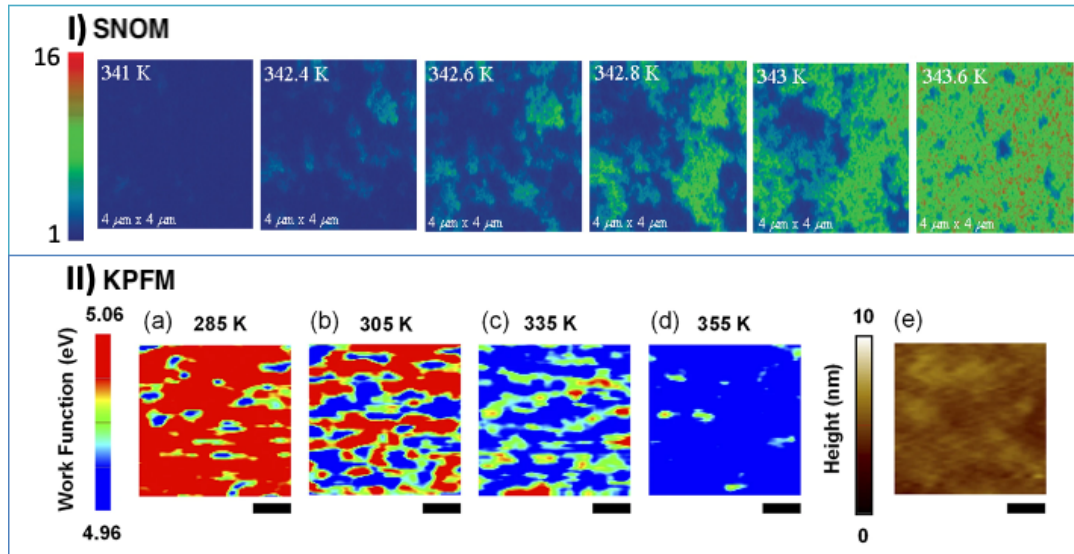


Figure 2.6 – (I) Images of the near-field scattering amplitude over the same $4\mu\text{m} \times 4\mu\text{m}$ area obtained by SNOM operating at the infrared frequency $\omega = 930\text{ cm}^{-1}$. These images are displayed for representative temperatures in the insulator-to-metal transition regime of VO_2 to show percolation in progress. The metallic regions (light blue, green, and red colors) give higher scattering near-field amplitude compared with the insulating phase (dark blue color). Taken from [84]. (II) Work function maps using KPFM at (a) 285, (b) 305, (c) 335 and (d) 355 K during heating. The color scale is the same for all images. The larger work function (red) represents the insulating phase and the smaller work function (blue) represents the metallic phase. (e) The surface morphology of the region used to obtain the work function maps. The scale bar is 100 nm. Taken from [130].

the attention until the mid-1990s. Choi et al. [134] investigated the temperature-dependent IR properties of a VO₂ film near the critical temperature (T_c). They obtained the dielectric constant and conductivity from reflectance and transmittance spectra in the 1600–400 cm⁻¹ frequency region, at temperatures between 20°C and 90°C. They found that the dielectric constant on the insulating side increases as the temperature approaches T_c . To explain this behavior, they introduced a composite-medium model, considering the film as an inhomogeneous medium composed of metallic and insulating domains. They treated the IMT in VO₂ as a percolation transition, attributing the dielectric anomaly near T_c to increased capacitive coupling between the metallic grains near the percolation threshold.

Following this description, low-temperature insulating phase can exist above T_c as a metastable phase, just as the high-temperature metallic phase can exist below T_c . As temperature rises, metallic phase nucleation droplets form across the sample, leading to spinodal decomposition and phase separation, rather than a sudden transition from one phase to the other. As temperature increases further, metallic droplets cluster and eventually form a large connected cluster, creating a conductive pathway through the sample (Fig. 2.5(a-c)).

Local probes

Near-field measurements, SNOM, have revealed the percolative nature of the IMT in VO₂ ([84] cited 1672 times on Google Scholar.) These scans show that metallic regions nucleate and grow with increasing temperature, eventually interconnecting (Fig. 2.6 I). This phase separation is influenced by intrinsic factors like the first-order nature of the transition and extrinsic effects such as local strain, deviations from stoichiometry, and grain boundaries.

In VO₂, electrically constrained paths have shown resistance avalanches, which were interpreted in terms of the universality class of uncorrelated percolation by Ramirez et al. [138]. Liu et al. in [139] argued that the first-order metal-insulator transition in VO₂ is also near a critical endpoint that can be reached by tuning disorder. By applying cluster network analysis techniques to the SNOM on VO₂ images acquired with the already mentioned method by Qazilbash et al. in (Fig. 2.5, [84]), they demonstrated, using six different critical exponents, that the critical endpoint of the Mott transition falls within the universality class of the random field Ising model. This finding reveals an interplay between interaction between domains and disorder in these systems. Moreover, the random field Ising universality class has also been shown to account for the spatial structure of locally oriented domains observed via STM on cuprate superconductors [140], which also exhibit a clear phase separation.

Kelvin Probe Force Microscopy (KPFM) has also been particularly versatile for investigating local surface potential under ambient conditions. KPFM results provide the local surface work function of a specific area without the need for numerical analysis [141]. KPFM measurements of the local surface work function (WS) have been used to reveal the phase transition behaviors of VO₂/TiO₂ thin films [130]. WS maps show the spatial distribution of metallic and insulating domains during the transition, with the evolution of the metallic domain fraction explaining the temperature dependence of resistivity based on the 2D percolation model (Fig. 2.6 II). The

KPFM measurements also revealed the fractal nature of the domain configuration. According to percolation theory, metallic clusters form a fractal surface, which can explain the impedance spectra; however, explicit experimental evidence for this has been lacking. The domain size is tens of nanometers at intermediate temperatures. The perimeter and area of the metallic domains follow power-law behaviors, with a power exponent larger than 1/2 suggesting that the metallic domains are fractal objects.

Time resolved probes

Recent experimental studies have indicated that the electronic IMT in VO₂ often precedes the structural phase transition [125], motivating time-resolved optical and structural studies. Ultrafast optical spectroscopy, spanning from the far infrared to the visible spectrum, and time-resolved X-ray and electron diffraction studies have been used to investigate the IMT in VO₂. These experiments aim to discern the relative influence of structural distortions and correlation effects on the IMT, leveraging the temporal resolution of ultrafast optical spectroscopy.

All the above considerations raise the question of how to directly observe the metallic and insulating domain configurations of VO₂ thin films and their evolution throughout the transition. Conventional techniques like X-ray Diffraction (XRD), photoemission spectroscopy, and optical spectroscopies provide macroscopic-scale averages. However, nanoscale probe-based tools such as Scanning Tunneling Microscopy (STM) and scanning probe microscopy (SPM) offer superior spatial resolution. The dielectric constant from optical spectra and the lattice constant from diffraction patterns can be obtained only after model-based fittings, in which the associated sample states and fitting parameters are chosen subjectively. Scanning Near-field Optical Microscopy (SNOM) and hard X-ray nanoprobe (HXN) measurements have been used to observe metallic and insulating domains in VO₂ thin films as they undergo the IMT [124]. Different methods to study the IMT transition macroscopically and dynamically are summarized in Table 2.1.

Characterization Method	Characteristics	Resolution	Applications	Ref.
Optical Spectroscopy	Probes anisotropy in macroscopic specimens; effective for materials with inhomogeneities smaller than light wavelength	Macroscopic	Studying anisotropic properties in phase-separated systems	[117]
Atomic Force Microscopy (AFM)	Coupled with IR lasers for high-resolution spatial mapping	8–10 nm	Probing local conductivity and phase transitions at the nanoscale	[118, 119]
Time-Resolved Spectroscopy	Investigates ultra-fast dynamics of phase transitions	Subpicosecond	Studying photoinduced phase transitions; discerning structural and electronic contributions to IMT	[120, 121, 106, 122]
X-ray Diffraction (XRD)	Provides averaged structural information at the macroscopic scale	Macroscopic	Investigating structural phase transitions and lattice distortions	[123, 124, 125]
Photoemission Spectroscopy	Probes electronic structure and properties	Macroscopic	Studying electronic phase transitions	[126, 120, 127]
Scanning Tunneling Microscopy (STM)	Offers superior spatial resolution for investigating local electronic properties	Nanoscale	Probing local electronic properties	[128, 129]
Kelvin Probe Force Microscopy (KPFM)	Measures local surface work function under ambient conditions	Nanoscale	Mapping spatial distribution of metallic and insulating domains; studying local phase transition behavior	[130]
Scanning Near-Field Optical Microscopy (SNOM)	Combines optical and near-field techniques for high-resolution imaging of phase-separated regions	8–10 nm	Studying optical properties and phase separation at the nanoscale	[84, 124, 119]
Time-Resolved X-ray Diffraction	Provides temporal and structural information of phase transitions	Subpicosecond to 15 ps	Investigating structural changes during photoinduced phase transitions	[131, 132]
Time-Resolved Electron Diffraction	Offers high temporal resolution for studying dynamics of phase transitions	Subpicosecond	Investigating rapid structural changes	[133]

Table 2.1 – Characterization methods and their characteristics to study phase transitions on VO₂.

2 Machine learning in materials science

The field of materials science has developed significantly, moving beyond conventional methods. It now involves the use of mathematical theories, computer simulations, and experimental research. The initial approach was based solely on instinct, without any concrete scientific foundation. The second stage in this transformation involved the use of mathematical models and physical principles like thermodynamics. The introduction of computers marked the third stage, allowing for the simulation of intricate real-world scenarios.

Machine learning (ML) is an expansive domain within the field of artificial intelligence that has emerged as a game-changer in materials science research by enabling rapid and precise analysis of complex material properties, predicting new materials with desired characteristics, and optimizing fabrication processes. It equips computers with the ability to learn from and interpret data in order to make informed decisions or predictions. With the current data availability and new technologies that provide insights into the molecular and atomic behavior of materials, machine learning enhances discovery, design, and performance prediction. As these technologies advance, they hold immense potential to transform our understanding, utilization, and innovation within materials science.

We now have the ability to construct models that can accurately predict the microscopic properties of materials, allowing for atomic-scale behavior prediction with unseen precision and speed. These models utilize sophisticated algorithms for materials characterization and imaging, thereby enabling comprehensive information extraction from large datasets. Moreover, these data-driven insights facilitate the identification of hidden correlations and trends within material property analyses. The use of predictive models accelerates the process of materials discovery and design, fostering the rapid development of novel compounds with custom-made properties.

However, to fully exploit the potential of ML in materials research, several challenges must be addressed. Key among these is the acquisition of high-quality data and the integration of domain knowledge into the ML models. Advanced algorithms are needed to account for the intricate relationships and complex behaviors exhibited by materials to ensure accurate predictions.

ML comprises an array of techniques and methods, which are primarily classified into two categories: supervised and unsupervised learning. In supervised learning, as the name suggests, the system learns through supervision in the form of labeled data [142]. The model is trained using a designated dataset where the correct output is known and provided. This helps the model to learn and understand the correlation between the input features and the corresponding output. It is analogous to learning with a teacher who provides guidance and corrects the student when they make a mistake.

On the other hand, unsupervised learning works with unlabeled data, uncovering hidden structures, patterns, and relationships within the data without any pre-existing labels or classifications to guide the process. It resembles to learning on one's own without any explicit instructions or guidance. This ability to learn from raw, unstructured data allows unsupervised learning to reveal deeper, often surprising insights, making it particularly useful in exploratory analysis, anomaly detection, or understanding complex phenomena.

In the following subsections, our primary focus will be on supervised learning.

2.1 Supervised learning

Supervised learning algorithms are used extensively in classification tasks, such as spam detection, where emails are classified as 'spam' or 'not spam', and image classification, which involves categorizing images into predefined classes. These tasks require the algorithm to learn from labeled training data and apply this learned knowledge to classify new, unseen data. During the training step, the algorithm identifies patterns within the training dataset, which consists of sample sets and labels. Then, it transforms these patterns into a mathematical model. In the inference step, This model is used to make predictions about samples not encountered during the training phase.

Another application example of supervise learning is in regression tasks such as predicting house prices. In these cases, the algorithm learns from a dataset of known prices and property features (like square footage, number of bedrooms, etc.) and models the relationship between these features and the price. Once trained, this model can predict the price of a house given its features. Common supervised learning algorithms include Linear Regression, Logistic Regression, Decision Trees, Random Forests, Support Vector Machines (SVMs), and Neural Networks.

2.2 Deep learning

Deep learning (DL) is a subset of machine learning characterized by the use of artificial neural networks with multiple layers, known as deep neural networks (DNNs), to model complex patterns in data [143]. Unlike shallow learning, which typically involves models with one or two nonlinear feature transformation layers (such as Gaussian Mixture Models, Logistic Regression, and Support Vector Machines), deep learning can have many layers, enabling it to learn hierarchical representations of data.

DL builds on linear regression and activation functions to create interconnected classifiers. While the theoretical understanding of the relationship between model performance, complexity, and computational requirements in deep learning is still evolving, it is clear that DL relies heavily on processing power. This is due to the problem of over-parameterization, which becomes more pronounced as more training data is used to improve model performance.

Large amounts of data are better handled with DL, besides it is particularly well-suited for complex pattern recognition tasks such as image recognition, natural language processing, and speech recognition. Its ability to learn hierarchical representations from raw data makes it highly effective in these domains. Some of the most popular deep learning algorithms include Convolutional Neural Networks (CNNs) for image-related tasks, Recurrent Neural Networks (RNNs) for sequential data, and Transformer models like GPT (Generative Pre-trained Transformer) for natural language processing.

The advantages of DL include its ability to automatically extract features from raw data, reducing the need for manual feature engineering. It also has the capacity to model intricate patterns and dependencies in data, which makes it particularly powerful for tasks that involve

large and complex datasets. As computational power and data availability continue to increase, the potential applications and impact of deep learning are expected to grow significantly.

2.3 Machine learning in image processing

ML has revolutionized image processing, leading to a wide range of applications. This progress is largely due to improved data accessibility and increased processing capabilities [144]. Modern ML systems interpret image data in ways similar to the human brain's processing of visual information. DL, in particular, has greatly influenced this field through its ability to independently learn hierarchical representations from raw image data [145].

For instance, it is possible to identify and precisely localize objects within images, which is particularly advantageous for computer vision applications, such as the detection of defective products in a production line or the protection of pedestrians on the roads [146]. Image classification is key in several AI applications, including the detection of anomalies in chemical analysis. Precise boundaries are drawn in a process called image segmentation [147], which has been used to tag different objects within an image. There are also generative models in which the algorithm encodes underlying patterns and creates new visual representations based on them. These models have been particularly used in the discovery of new compounds with specific features, for example, in pharmaceutical applications, that are feasible to work in nature.

DL methodologies are also used for image understanding and analysis, which involves identifying features and corresponding data from images for interpretation. Technologies such as Convolutional Neural Networks (CNNs), Residual Neural Networks (ResNet), and Advanced Convolutional Neural Networks for Machine Vision can be employed for this purpose. This process typically involves extracting knowledge representation from the image data, conducting real-time examination and processing of the image based on the extracted representation, and exploring intricate patterns to discover features.

During this thesis, we are going to process images from optical microscopy, and for this reason, we are going to focus on CNNs.

2.4 Convolutional neural networks

Convolutional Neural Networks (CNNs) are a type of DNN known for their highly structured organization and translation invariance, ensuring that the network can recognize objects regardless of their position in the frame. In a CNN, a large number of neurons are arranged first into channels and then into layers, creating a systematic, hierarchical transformation of input data as it passes through the network.

Different components of the CNN learn different information. For example, different network components like neurons, channels, and layers tend to learn different concepts [149]. The complexity of CNN filter representations also increases gradually as the filter positions move deeper into the network (Fig. 2.7). The hierarchical representation in CNN components results in the convolution layers of a CNN performing feature learning, while the final fully connected layers are considered to perform prediction.

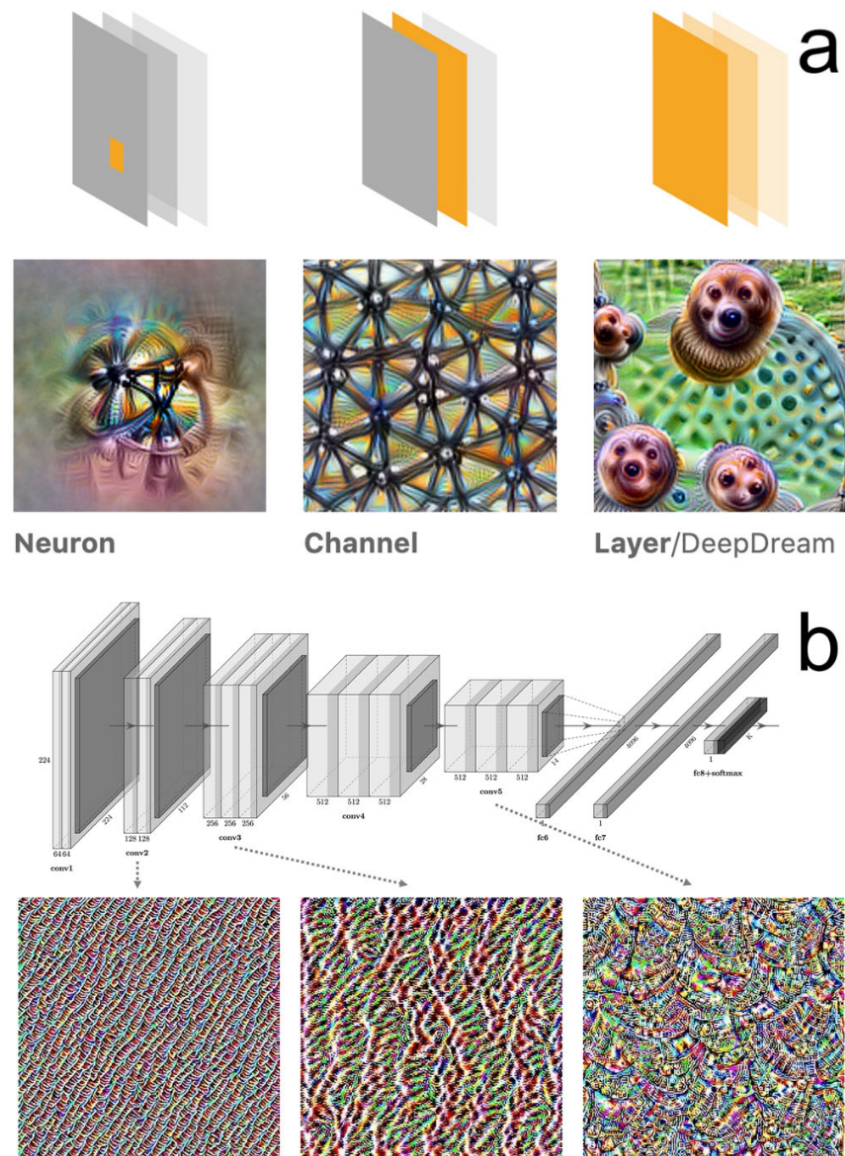


Figure 2.7 – Illustration of the hierarchical feature representation within CNNs. A Comparison of concepts contained in different network levels (neuron, channel, and layer). b Visualization of CNN filters from different layers of an imageNet pretrained VGG16 network. Note that the filter representations become more and more complicated as filter positions move deep along the network. The early layer filter representations are relatively primitive, while the top layer filter representations are highly complicated. The VGG16 architecture is plotted using the plot neural net library. Filter representations are visualized using the convolutional neural network visualizations library. Taken from [148].

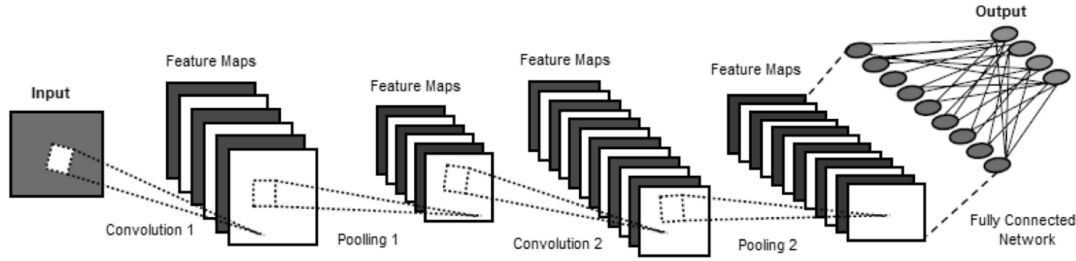


Figure 2.8 – Convolutional neural network structure

A CNN is particularly suited for processing data with a grid-like topology, such as an image. Each neuron in a CNN works within its own receptive field, similar to how neurons in the human brain process visual data. The layers of a CNN are designed to detect simpler patterns first (like lines and curves) and more complex patterns (like faces and objects) further along, essentially mimicking the way humans visually perceive the world.

A typical CNN architecture consists of three main layers (Fig. 2.8): a convolutional layer, a pooling layer, and a fully connected layer. The convolutional layer, the core building block of a CNN, carries out most of the network’s computational load. This layer performs a dot product between two matrices, one being the set of learnable parameters or the kernel, and the other being the restricted portion of the receptive field.

CNNs consist of three primary types of layers: convolutional layers, pooling layers, and fully connected layers. Each type of layer has a distinct function in processing and transforming the input data.

Convolutional Layer

The core building block of a CNN, this layer performs a convolution operation that involves sliding a set of learnable filters (kernels) over the input data. Each filter captures specific features such as edges, textures, and patterns. The convolution operation produces a feature map, which preserves the spatial information of the learned features at various positions in the input.

Convolution layers leverage sparse interactions, parameter sharing, and equivariant representations, reducing computational requirements and enhancing statistical efficiency.

Pooling Layer

This layer reduces the spatial dimensions of the feature maps, lowering the number of parameters and computations in the network. Common pooling operations include Max pooling, which selects the maximum value in a region, and average pooling, which calculates the average value in a region.

Fully Connected Layer

Neurons in this layer are fully connected to all neurons in the previous layer, similar to a traditional neural network. This layer maps the learned features to the output, performing classification or regression tasks. It integrates the features extracted by the convolutional and pooling layers, enabling complex decision-making processes.

To introduce non-linearity into the network, activation functions are applied after convolutional layers. Common activation functions include:

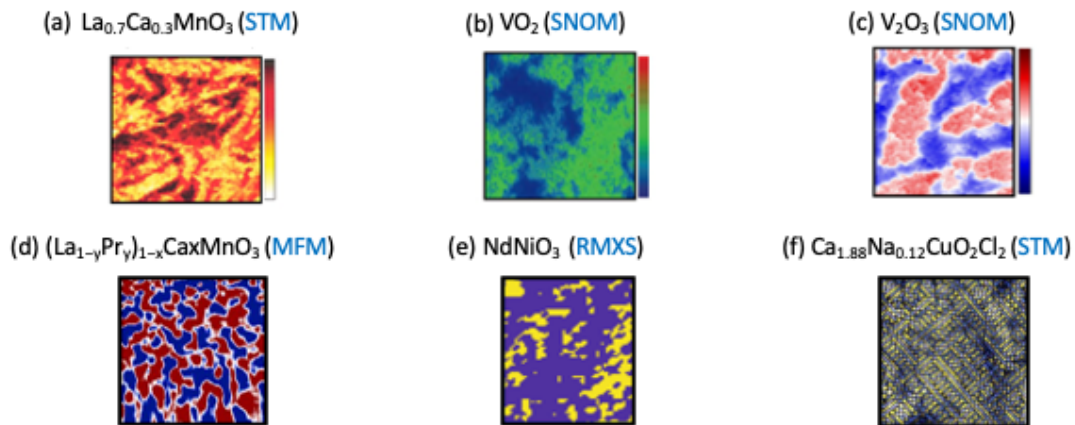


Figure 2.9 – Schematic diagram of the IMT in the VO_2 film. (a) STM spectroscopic images of $\text{La}_{1-x}\text{Ca}_x\text{MnO}_3$ (with x of about 0.3) showcasing the insulating (paramagnetic, light colors) and metallic (ferromagnetic, dark colors) of a thin film of $0.61\mu\text{m} \times 0.61\mu\text{m}$. [150] (b) Images of the near-field scattering amplitude of $4\mu\text{m} \times 4\mu\text{m}$ thin film of VO_2 showing that the metallic regions (light blue, green, and red colors) and the insulating phase (dark blue color) [84]. (c) High-resolution co-localized near-field images of coexisting phases antiferromagnetic insulator (blue) to paramagnetic metal (red) phase; $6\mu\text{m} \times \mu\text{m}$ [151]. (d) MFM images of a LPCMO $8\mu\text{m} \times 8\mu\text{m}$ thin films showing the antiferromagnetic (blue) and the ferromagnetic (red) phases [152]. (e) The AFM domain map at 130K (warming cycle) is binarized to highlight the AFM domains insulating (yellow) and paramagnetic-metallic domains (blue) [153]. (f) Na-CCOC images ($4\text{ nm} \times 4\text{ nm}$) of $\Delta^2 R$ (Laplacian) computed from R maps. Large R (yellow) means that the corresponding tunneling spectrum is more symmetric, whereas low R (blue) means that it is more asymmetric [154].

Sigmoid: Compresses the output to a range between 0 and 1.

$$f(x) = \frac{1}{1 + \exp(-x)} \quad (2.1)$$

Tanh: Maps the output to a range between -1 and 1, zero-centered.

$$f(x) = \frac{\exp(x) - \exp(-x)}{\exp(x) + \exp(-x)} \quad (2.2)$$

ReLU (Rectified Linear Unit): Allows for faster and more reliable convergence.

$$R(x) = \max(0, x) \quad (2.3)$$

2.5 Material characterization and imaging

Materials characterization and data analysis play a crucial role in understanding material behaviors, optimizing for specific purposes, discovering new materials, and furthering materials science research. Analyses that involve ML face challenges due to the frequently short training sets used for ML models [155].

Materials science has evolved to encompass mathematical theory, simulations, and exper-

imental research. Material properties can be characterized using both macroscopic and microscopic descriptions. Computational modelling and experimental measurement are the most common techniques for examining these properties. However, they involve complex procedures and setups, making it difficult to accurately represent the intricate logical connections between a material's qualities and the factors affecting them. Given these complexities, the development of intelligent and high-performance prediction models is crucial for accurately predicting material properties efficiently, both in terms of time and computational resources.

Recent advancements in high-resolution imaging techniques provide novel opportunities for ML to swiftly and quantitatively analyze functional materials both statically and dynamically [156]. This complements traditional methods such as modeling, simulations, and synthesis.

By utilizing surface probes such as Atomic Force Microscopy (AFM), STM, and SNOM, we can reveal intricate electronic pattern formations spanning multiple length scales on the surfaces of correlated quantum materials. Some examples of those are pattern formations are shown in Fig. 2.9. VO₂, with its self-similar metal and insulator domains across various scales, serves as a prime example. Similarly, manganites exhibit pattern formations where ferromagnetic and antiferromagnetic regions coexist over multiple length scales [152]. The electronic glass in cuprates features unidirectional stripe domains forming fractal patterns with correlations extending over four orders of magnitude in length scale [154]. Additionally, magnetic domains in NdNiO₃ display fractal textures [153].

Also, modern imaging methods, such as scanning transmission electron microscopy Scanning Transmission Electron Microscopy (STEM), STM, and AFM allow for direct visualization of atomic-level structures and functional features in complex materials. Concurrently, enhancing ML-driven image recognition facilitates real-time data analysis, reduces workflow bottlenecks in materials development, and aids in knowledge extraction using physics-informed models.

For instance, a study by Ma et al. [157] employed an ML approach to map microstructure images to processing conditions in uranium-molybdenum nuclear fuel alloy, achieving a strong classification accuracy with an F1 score of 95.1%. This method successfully differentiated between micrographs related to ten distinct thermo-mechanical processing conditions. Another study by Ziatdinov et al. [158] used Gaussian process regression-based extrapolation for contact KPFM, incorporating an interactive Google Colab notebook for comprehensive analysis. Vasudevan et al. [159] demonstrated the use of Bayesian inference to enhance the reliability of interpreting scanning probe microscopy data in ferroelectric thin films, highlighting the integration of prior material knowledge and model selection within the Bayesian framework.

Studies have demonstrated the effective use of CNNs in analyzing images from material characterization methods. Kondo et al. in [160] used heat maps to understand semantic features from microstructure images to predict the ionic conductivity of yttria-stabilized zirconia (YSZ), a solid electrolyte ceramic material. Their CNN model employed a technique similar to class activation mapping (CAM) and gradient-weighted class activation mapping (Grad-CAM). The model's design connected the top convolution layer to the first fully connected layer via global average pooling (GAP), creating clear correspondences between convolution filters and fully connected layer neurons. This setup allowed the authors to generate heat maps showing regions

contributing to high or low ionic conductivity. They found that voids in the microstructure were indicative of low ionic conductivity, while defect-free areas correlated with high conductivity. These findings aligned with experimental evidence and increased confidence in the CNN model's ability to capture physically reasonable features. Additionally, the heat maps helped in determining the optimal representative volume element (RVE) size for the material, guiding further characterization and data collection.

Oviedo et al. in [161] applied a similar heat map explanation technique to diagnose model errors in predicting the space group and crystallographic dimensionality of thin-film materials from XRD spectra. Their CNN architecture included three 1D convolution layers, a GAP layer, and a final dense layer with softmax activation, treating XRD patterns as 1D pseudo-image inputs. Heat maps were generated for individual XRD patterns and averaged within each space group class to identify patterns. Comparing these heat maps allowed the authors to investigate misclassifications. They observed that the heat map of a correctly classified input closely matched the average heat map of its space group class. In contrast, the heat map of a misclassified input resembled the average heat map of the incorrect class, revealing the lack of discriminative features in some inputs. This method confirmed the CNN's effectiveness in analyzing and interpreting XRD patterns, despite the differences between spectrum and image data.

In summary, machine learning is a powerful tool in materials science, providing new ways to analyze data, understand materials, and predict their properties. These advancements enable more efficient research and development, paving the way for innovative materials and applications.

Chapter 3

Optical characterization of VO₂

High spatial resolution characterization techniques such as surface probes, namely *AFM* [162], *KPFM* [130], *SNOM* [84], and *STM* [163], have been used to image VO₂ intricate patterns near criticality. While these techniques allow a resolution of a few nanometers, they are limited in showing and tracking the formation of the metallic/insulating phases over a wide temperature range in a single experiment, and they take a lot of time to scan larger surfaces. Not only the scanning time presents a drawback, but also the technical aspects of each characterization method. For instance, *STM* lacks resolution near room temperature and lacks accuracy as the temperature is modified [164]. Conductive *AFM* allows the construction of an *IMT* temperature map of a VO₂ sample, by scanning it at 25 different temperatures around the transition temperature, however, the substrate must be conductive which sets constraints to the geometry of the device [162]. Therefore, displaying the dynamics of the metallic/insulating phase formation near room temperature requires a more adaptable technique with more time(temperature) resolution.

We aim to use a time-resolved characterization method to study VO₂ during its *IMT*, taking advantage of:

- the optical contrast in the visible spectrum,
- the well-defined phase separation between metallic and insulating sites,
- the observation of critical behavior across different length scales.

In this chapter, the experimental set-up to obtain hundreds micrographs of VO₂ for a whole hysteresis loop in a single experiment is presented, including details on the equipment used for the measurements, the methods followed, the challenges we faced during the experiments, and ways to overcome them, and a description of the software used to automate the process of acquiring the digital images.

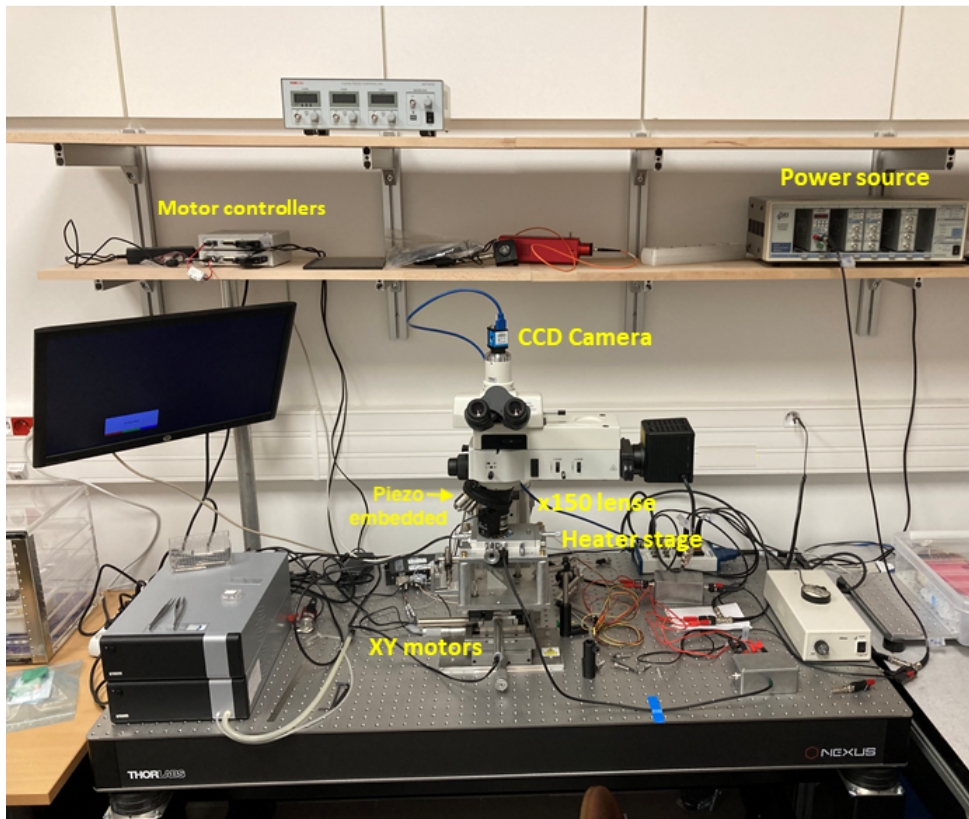


Figure 3.1 – Experimental set-up displaying the microscope hardware, optics, and temperature controller to perform the characterization of the samples.

1 Materials and methods

1.1 Instrumentation- experimental set-up

Microscope hardware The experimental set-up (Fig. 3.1) consists of a thin film VO₂ sample placed on a Peltier heater or a Linkam's temperature control system stage under a Nikon reflected light microscope (epi-illumination). Micrographs are captured using a Charge-coupled device (CCD) camera while the temperature is ramped up and down for a defined number of cycles.

Optics. The samples were measured around the focal point of 1mm in the visible range using a magnification $M = 150$ dry Olympus objective lens with a numerical aperture of $NA = 0.9$. The theoretical lateral resolution is estimated to be $Resolution(r) = \lambda/(2NA) = 278nm$ in the visible range using the Rayleigh criterion. Images were captured with a CCD camera (DMK 33UX252) and stored with 2048×1536 - pixel resolution in BMP format.

Motors. The sample holder can be translated in the X-Y directions in two ways: manually, using the stage control knobs, and automatically, controlling two stepper motors through LabVIEW drivers in a computer. For focusing purposes, the objective is moved in the vertical axis using a PI PIFOC piezo nanofocusing system (PD72Z1C), also controlled in the computer.

Temperature controller. The temperature control is performed by a LINKAM control system THMS350V which uses a 100 Ohm platinum sensor (Pt100) with a temperature stability $<0.1^\circ\text{C}$. This equipment is capable of working for a broad range of temperatures ($<-195^\circ\text{C}$ to 350°C with LNP96 cooling pump). In the experiments, we used a temperature range of 27°C to 90°C . We specified and set parameters for the applied temperature protocols such as starting and end temperature for each ramp, waiting time in between ramps, and temperature rate using the manufacturer software.

In addition to the applied temperature control, we placed a Pt100 resistance thermometer close to the sample which at 0°C has a resistance of 100Ω . The output reading from this sensor was recorded in a Labview program described in details in Fig. 3.6.

The most simple temperature protocol consists on ramping the temperature up making sure it surpassed the critical temperature T_c and ramping the temperature down, to obtain the hysteresis loop.

1.2 VO₂ samples

VO₂ thin films are used in all the experiments since they are able to dissipate heat through the substrate and to withstand the distortions caused by repeatedly applying heating and cooling cycles, hence a small lattice distortion along the c-axis is produced.

We used samples prepared with two different preparation methods and substrate orientations:

Sample A

Vanadium dioxide thin films were prepared by reactive RF magnetron sputtering of a V₂O₃ target ($> 99.7\%$, ACI Alloys, Inc.) on an r-cut sapphire substrate. A mixture of ultrahigh purity (UHP) argon and UHP oxygen was used for sputtering. The total pressure during deposition was 4mTorr, and the oxygen partial pressure was optimized to 0.1mTorr (2.5% of the total

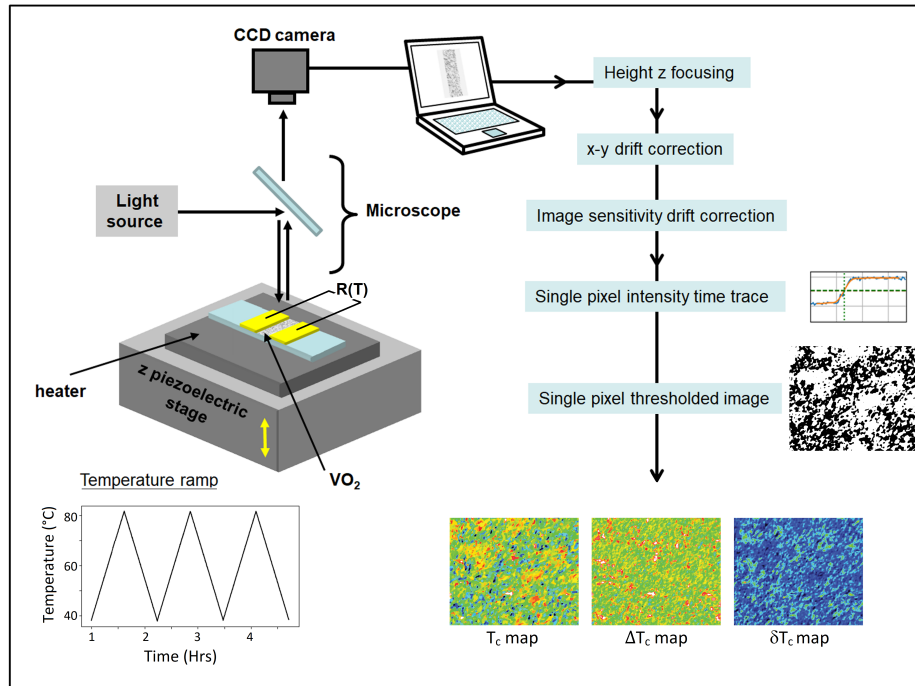


Figure 3.2 – Schematics of the microscope and image analysis created specifically to measure spatial maps of clusters in VO_2 during the IMT while recording resistivity $R(T)$ simultaneously. The sample was positioned on a Peltier heater or Linkam Thms350V temperature controller to apply temperature ramps (bottom left). The sample height was varied by steps of 80nm via a piezoelectric actuator placed under it or in the objective. The best-focused images were chosen post-experiment using an image compression method and Tenengrad function. The height focus of the sample was thus controlled within 80nm throughout the experiment. Fine xy plane drift correction within a single pixel was performed post-experiment. Camera sensitivity was normalized throughout the recording. Using this fully stabilized image series, black and white thresholds were applied for each pixel individually, accurately determining if it is in the metallic or insulating state. We use this information to construct spatial maps of the local transition temperature T_c , hysteresis width ΔT_c and transition width δT_c . The map size displayed in this figure is $33.6\ \mu\text{m} \times 27.6\ \mu\text{m}$.

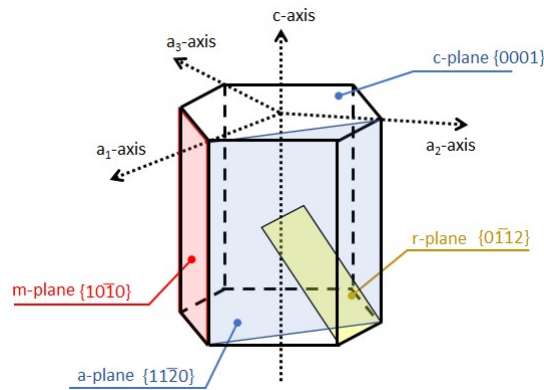


Figure 3.3 – The structure of the primary planes of the sapphire crystal corresponding to the structure system of sapphire. Taken from [165].

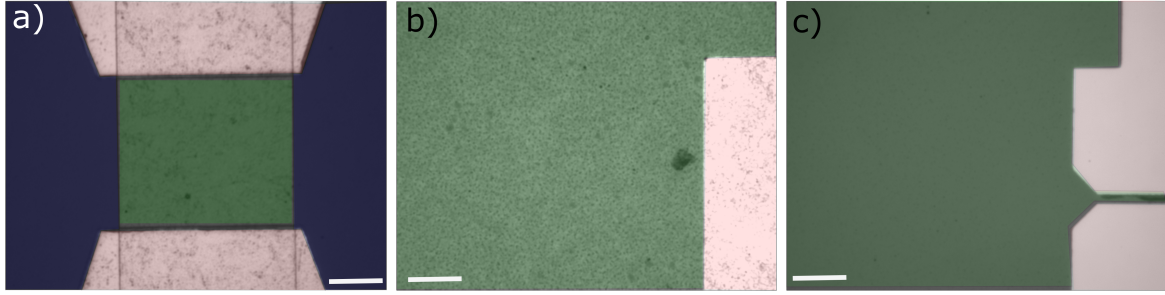


Figure 3.4 – Micrographs of the VO₂ samples used for the experiment of the present work. The samples have different electrodes geometry. Green colored area represents VO₂; pink area, gold electrodes; and blue area, sapphire substrate. The white bar is 10 μm wide. (a) Sample A prepared by RF magnetron sputtering on a r-cut sapphire substrate. (b) and (c) Sample B (84 nm) and C (136 nm), both prepared by sol-gel method on a c-cut sapphire substrate.

pressure). The substrate temperature during deposition was 600 °C while the RF magnetron power was kept at 100W. Sample is 100nm thick. For samples prepared in a similar fashion with thickness of 100nm and 150nm, grain sizes were 40nm and 130nm respectively. The sample is found to have a relative 27% optical change in the visible range when passing the IMT. Gold electrodes were deposited on top of the film, separated by 30 μm (Figure 3.4 a.) The VO₂ area of the simple after lithography and Reactive-ion etching is 30 μm \times 35 μm and show a clear IMT above 68 °C as evidenced by a drop in resistivity of 4 orders of magnitude.

Sample B and C

The VO₂ films of different thickness (84 nm (B), 136 nm(C)) were grown on a c-cut sapphire substrate (Al₂O₃, (0001)) by a sol-gel method. Vanadium pentoxide (V₂O₅, 99%, Acros Organics) and oxalic acid (H₂C₂O₄, $\geq 99.0\%$, Sigma-Aldrich) were selected as the starting materials. Specifically, 5 mmol V₂O₅ and 15 mmol H₂C₂O₄ were evenly mixed in a three-necked flask. Next, for the film with a thickness of 84 nm, the mixed powder was dissolved by 25 mL of ethanol whilst stirring. For the film with a thickness of 136 nm, the mixed powder was dissolved by 20 mL of ethanol whilst stirring. The solution was heated at 120 °C for 12 h under reflux, then the deep blue precursor solution was formed. C-cut sapphire substrate was cleaned ultrasonically in soapy water, acetone, and ethanol, followed by a 30-minute ozone cleaning to ensure that substrates have a good hydrophilicity. Subsequently films were coated on the sapphire substrate at a spin rate of 3000 rpm for 50 s. Then the as-prepared films were dried at 100 °C for 3 minutes to remove the excess solvent, followed by an annealing process. For the 84 nm and 136 nm films, annealing was performed at 450 °C for 90 minutes and 300 minutes under vacuum conditions, respectively.

Sapphire substrate

All samples used in the present work have Sapphire (Al₂O₃) as the substrate (Figure 3.3.)It exhibits unique properties such as large linear thermal expansion coefficient around room temperature ($\sim 5.5 \times 10^{-6}/\text{K}$), and light transmitting properties. During processes like thin-film

deposition, lithography, and annealing, the substrate and the films deposited on it undergo temperature changes. The ability to manage thermal expansion ensures that the substrate can handle the thermal stresses without deforming or causing damage to the thin films. A large linear thermal expansion coefficient in sapphire is important when applying several temperature ramps because it ensures mechanical stability, thermal compatibility with other materials, maintains optical integrity, and enhances process efficiency. All these are reasons why it is extensively used in SoS chips integrated circuits and photovoltaics. The R-plane is the non-polar plane of sapphire which is highly suitable for optical applications since it has a low optical index.

1.3 Image acquisition

In this work, we developed an image acquisition workflow which automates the process of capturing the micrographs during an experiment. The automated microscopy has many advantages: increased productivity, gathering more data in less amount of time; higher reproducibility, ensures the experiment is performed following the same steps; more reliability, as it reduces manual operation it is less likely to introduce human errors.

However, the automation of the image acquisition presented two main challenges. Firstly, capturing the best-focused micrographs out of a stack of images, and secondly, having the sample in place and focus until the temperature protocol finishes, since we have thermal drift in all directions.

Thermal drift compensation

z direction: During the collection of images we observed a drift in the axial position, as we are taking a stack of images we needed a fast response, that is the reason to use a piezo since it has a high precision and exhibits low hysteresis.

xy direction: A piezo response is faster, but it has a limited travel distance. That is the reason why for x-y directions, we use two stepper motors integrated to the stage, one for each direction. We keep the samples in a set starting position with a variation of maximum 20 pixels between each image. This variation will ensure the VO₂ area is kept a margin from the edge of the CCD where the camera sensitivity can change significantly.

Selection of best-focused images

Capturing well-focused images is key for any automatic microscopy system [166], and in particular for this application where blurred images could introduce problems in the alignment and tracking of each pixel over time. To get images in focus, we used a spatial domain focus measure, the Tenenbaum gradient *Tenengrad* (eq. 3.1) [167][168]. This method assumes that a higher gradient represents sharper edges, meaning a large intensity difference between neighboring pixels. It relies on the maximization of the sum of the squared Sobel gradient magnitude value (eq. 3.2), for the vertical (S_x) and horizontal (S_y) components.

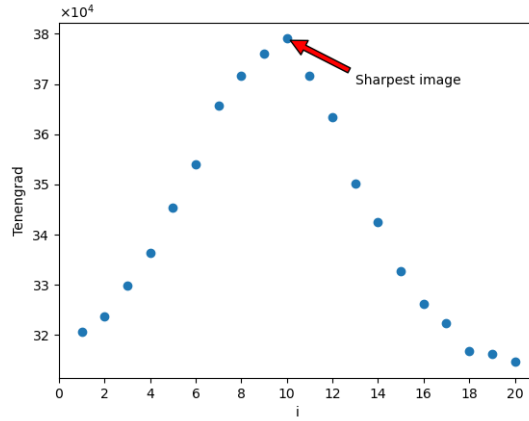


Figure 3.5 – Tenengrad of a stack of 20 micrographs. The sharpest image corresponds to the maximum Tenengrad value.

$$F_{Tenengrad} = \sum_{i=2}^{M-1} \sum_{j=2}^{N-1} (\nabla S(x, y))^2 \quad (3.1)$$

$$\nabla S(x, y) = \sqrt{\nabla S_x(x, y)^2 + \nabla S_y(x, y)^2} \quad (3.2)$$

The criteria followed to select the best images for further analysis included: (i) the sharpest image has a clear maxima in the gradient in comparison with the blurrier images. (ii) this is found approximately in the middle of the stack, if xy repositioning works properly and if temperature ramp is lower than 5 °C/min. We achieved the criteria taking the z-series at steps of 1 μm. Fig 3.5 displays an example for the selection of the sharpest image out of a stack of 20 micrographs.

In the case of a camera the focal depth will vary according to number of pixels of CCD, magnification M , and numerical aperture NA . We can compute the theoretical smallest distance that can be resolved e using eq. 3.3 where P is the pixel size of the CCD sensor. Considering that the camera uses a sensor with a pixel size of 15 μm we found a theoretical $e = 0.2 \mu\text{m}$.

$$2P = Me \quad (3.3)$$

Following the equation 3.4 that relates the depth of field (DOF) and numerical aperture of a microscope objective, suggested for Nikon microscopes, from the previous result, we get a $DOF = 0.618 \mu\text{m}$. The steps taken are smaller than two times the theoretical DOF, therefore finding the sharpest image in between is possible.

$$DOF = \frac{\lambda \eta}{NA^2} + \frac{\eta e}{M(NA)} \quad (3.4)$$

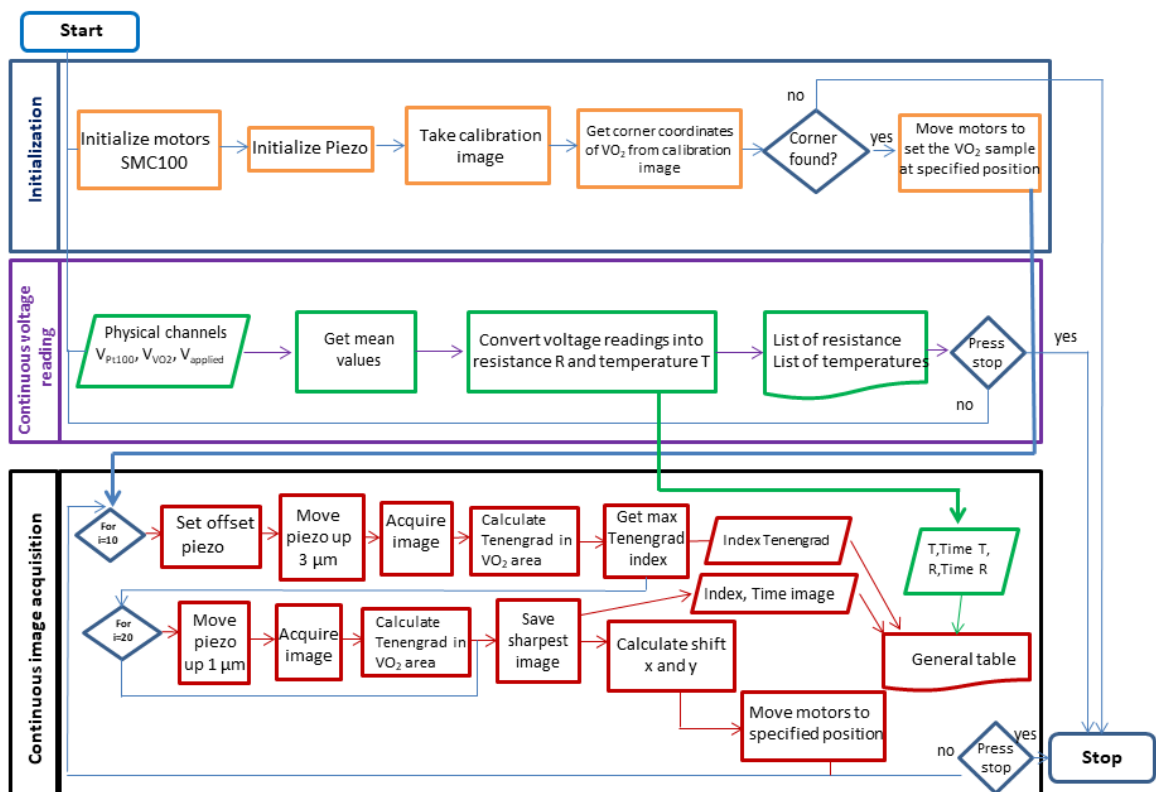


Figure 3.6 – Flowchart displaying the logic of the Labview program for the automatic acquisition of the sharpest micrographs.

1.4 Imaging workflow for micrographs automated acquisition

To start acquiring images with the microscope, we first make sure the sample is correctly placed in the Peltier heater. This helps us see the borders of the electrodes clearly and acts as our starting point. We do this part manually by adjusting knobs in the x and y directions. After that, we launch a program in LabVIEW, following the steps shown in details in the flowchart in Figure 3.6. Once LabVIEW is running, we use a pre-set temperature protocol that heats and cools the sample at specific rates (typically 1 °C/min, but it can go up to 5 °C/min). This is done with through the utilization of Linkam's software.

Initialization

The program begins by setting up the directories for saving the images. Next, it positions the stage at an initial location by activating the two stepper motors. It also initializes the voltage output responsible for adjusting the piezo in the z-axis. A calibration image is then captured to set coordinates for tracking the edges of the VO₂ sample. Once the program identifies these corners, it uses them as references to move the motors and position the sample at specified coordinates. The program stops if encounters difficulty identifying any of the corners.

Continuos voltage reading

Three physical channels are created as voltage analog inputs via a National Instruments acquisition card. The first channel, *VPt100*, measures the voltage drop across the Pt100 sensor, enabling the conversion to temperature. Additionally, we apply a voltage of 1.3 V between the gold electrodes of the sample, denoted as *Vapplied*. The resulting voltage drop across the VO₂ sample is then measured and converted to determine the current resistance in the VO₂. This readings are run continuously and saved in .txt files as lists of resistance and temperatures once the program started even when is not acquiring images.

Continuos image acquisition

For continuous image acquisition, a series of images along the z-axis is captured. Initially, the piezo is lowered to a starting position, and micrographs are taken in increments of 3 μ m. This action brings the sample in and out of focus. The Tenengrad is then calculated for each image, and the index of the image with the largest gradient is determined. This process is repeated for ten cycles. A more refined scan to identify the sharpest image is subsequently conducted by moving the piezo in 1 μ m steps. During this step, the Tenengrad is calculated, and the mean grayscale is recorded. The image with the highest gradient, indicating sharpness, is kept. This process is iterated for a total of 20 cycles. The resulting index, time of micrograph acquisition, temperature, resistance, and their corresponding times are recorded in a .txt file named "general table."

Additionally, the Tenengrad of the last image is calculated to correct for temperature drift,

provided it exceeds 20 pixels. It is essential to note that there may be a backlash of xy motors when changing directions, especially during transitions from heating to cooling or vice versa in the ramping process. The entire image selection process permits the selection of one image every 10 seconds. Thus, we have chosen a temperature rate of 1 °C/min to have 6 images/ °C.

2 Image processing for applications

We ran most of the image processing codes on Purdue University’s supercomputing facilities due to the large dataset requiring extensive memory. We have access to these resources thanks to our collaboration with Professor Erica Carlson’s group.

2.1 Obtaining single pixel time trace

The correct alignment of the micrographs is crucial for the analysis and applications described in the following chapters, since we are tracking changes in intensity for each single pixel at a certain recorded temperature to analyze the dynamics of VO₂ MIT over time. Each pixel represents a 37 nm wide sample. The flowchart in Figure 3.7 illustrates the operations over the raw micrographs to obtain the single pixel time traces.

Divide temperature cycles

First, we take the file containing the frame number and the recorded temperature associated to the images to get the initial and last frame for every warm and cooling ramp. The function finds the temperature local minima and maxima to return the turning points. We then create a new file with temperature and frame information for every hysteresis loop in the temperature protocol.

High frequency noise was filtered in the temperature data taken using the Pt100 by fitting a linear slope through the large temperature sweeps. This matched the internal temperature sensor slope of the Linkam Thms350V temperature controller.

Collect all raw images

We treat the images as 2D arrays in Python using the numpy library. We collect the raw micrographs with full field of view saving them in 3D numpy memory arrays. The third dimension correspond to the frame number associated with the image.

Fit background illumination

Before alignment, it is important to decrease as much as possible the effect of the field curvature on the CCD surface, which is a common aberration in optical microscopy. We take a micrograph of only the sapphire area of the sample. In the python script the code generates a fitted surface of a paraboloid, the function returns the optimized parameters for the used background. The VO₂ area is centered experiencing shifts from the center of the micrograph of $\pm 1\mu m - 2\mu m$. Hence, we assume it is in the center of the paraboloid.

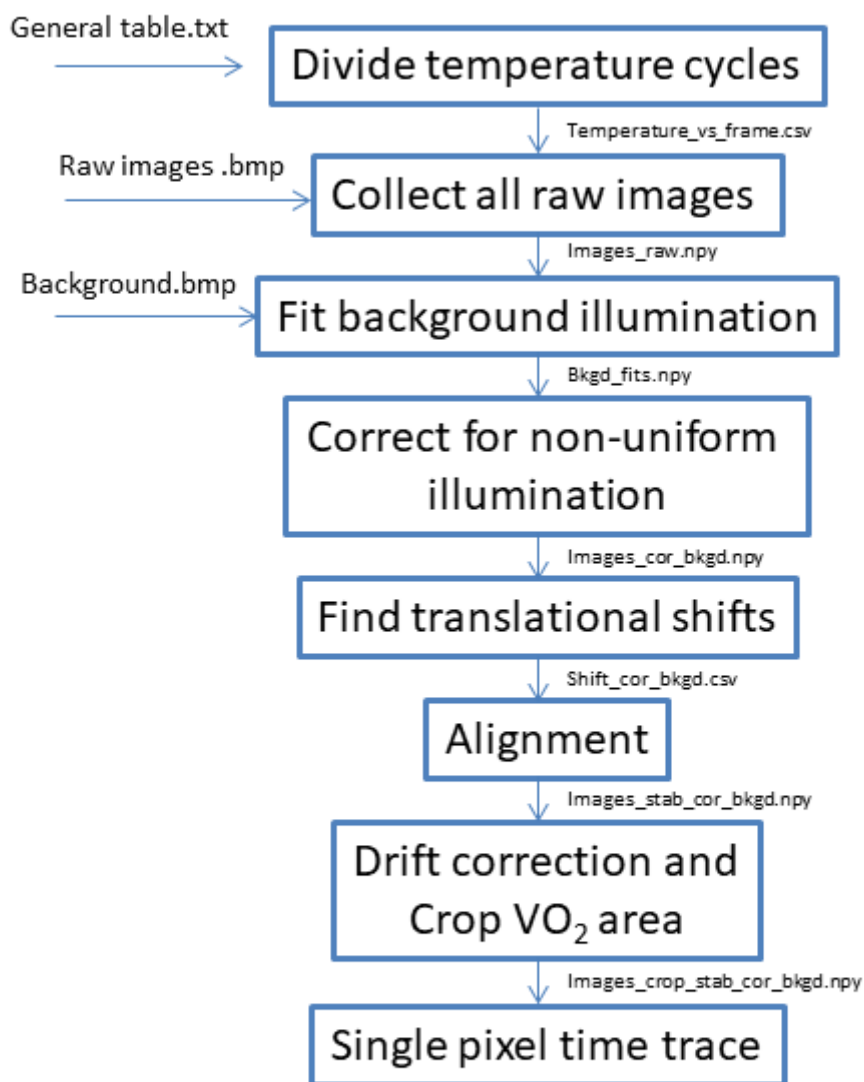


Figure 3.7 – Flowchart followed to process raw micrographs and obtain single-pixel time trace of the VO₂ area.

Correct for non-uniform illumination

Each frame is divided by the calculated change in illumination according to the fitted surface data of the background. This procedure is performed over the raw images.

Find translational shifts

The code used to find the shifts in the X and Y axes is based on the method mentioned in [169]. This method relies on upsampled cross-correlation of all image points. It detects a cross-correlation peak by a FFT (fast Fourier transform) and further enhances the shift estimation by performing upsampling of the Discrete Fourier Transform (DFT.) We defined to compute it within a hundred of a pixel. We registered the shifts in a .csv file.

A mathematical formula for cross-correlation in image processing is presented in Eq. 3.5, where r is the reference image and f is the image to be aligned. The images are normalized by subtracting the mean and dividing by the standard deviation.

$$\text{Crosscorrelation} = \frac{1}{n} \sum_{x,y} \left(\frac{1}{\sigma_f \sigma_t} f(x,y)r(x,y) \right) \quad (3.5)$$

Alignment

Taking the .csv file from the previous step, we aligned the images taking into account the shifts for each direction, obtaining a new image size depending on the maximum shift in each axis.

Drift correction and crop VO₂ area

Once the images are properly aligned we select the VO₂ area to analyze. The variations we observe in reflected intensity from the VO₂ region are primarily due to changes in local reflectivity due to the IMT. However, there can be other contributions to this spatial variation, including effects such as surface height variations from sample warping, variations in film thickness, minor surface defects, and even shadows cast from the 150nm thick gold leads. There can even be differences in pixel sensitivity in the camera itself. Because each of these contributions is independent of temperature (i.e. constant in time), their effects can be distinguished from that of the temperature driven IMT.

The strategy we employed to decrease the effects of drift in the VO₂ mean intensity (VO₂[i]) caused by variations in illumination involves division by the change in a selected sapphire area. This approach is based on the fact that sapphire's reflectivity exhibits minimal changes within the range of temperatures applied. However, we found a change in reflectivity of ~ 2% related to the automatic repositioning of the objective. There are also external factors that contribute to sapphire's reflectivity changes such as ambient light and lamp illumination changes. To take into consideration this variability, we computed a linear regression correlating the sapphire mean intensity (Sapphire[i]) with the frame number i . We select the initial point of the linear regression (LRSapphire[0]) to estimate the change of the average sapphire reflectivity on each frame assessed following the equation 3.6.

$$CorrectedIntensityVO_2[i] = \frac{VO_2[i] \times LRSapphire[0]}{Sapphire[i]} \quad (3.6)$$

Alignment for sample B and C There is an extra step to perform for flat samples with small number of signatures to detect. We apply a Sobel filter to threshold the edges, so the peaks are detectable when applying the cross correlation. Then the standard protocol for alignment is followed.

Single pixel time trace

We can visualize the intensity with respect to the frame number to obtain the single pixel trace over time. We observe a step down indicating that VO₂ switches from high intensity insulating to low intensity metallic for the warming ramp, and equivalently a step up when cooling down. Therefore we can obtain a complete hysteresis loop in terms of relative intensity for each single pixel (a 37 nm wide VO₂ sample), finding a novel way to characterize this material during the IMT when conventional methods involve electrical measurements of the global resistance change.

2.2 Time domain convolution

Automation of the micrographs capture allows us to obtain a series of images (~ 500 images at $1^\circ\text{C}/\text{min}$ for a complete hysteresis loop) sufficient to have enough points in the time trace to filter high frequency noise. By applying a convolution filter based on a Gaussian operator ($\sigma = 2.5$), we are able to isolate the changes in local reflectivity due to the IMT and significantly reduce the white noise.

Figure 3.9 shows a single pixel's time trace transitioning from fully insulating to fully metallic. We observe that the raw time trace is noisy in the transition midpoint. If we apply a 3-point convolution, the time trace becomes smoother and it only crosses the midpoint once in comparison to the raw time trace. We perform this method to reduce the noise of the images classified by the deep learning classifier which is explain in details in Chapter6.

Finding Tc

VO₂ samples with well-characterized transition temperatures enable control and manipulation of the material's behavior so that it can be used in devices and study the emergent phenomena in the critical temperature range. The method to get the Tc for each pixel consists on smoothing the raw time trace with a 11-point convolution, then taking the minimum and maximum intensity value, and selecting the midpoint. A frame number is associated to the midway point intensity, and also referred to a recorded temperature.

In order to know at what intensity to set the threshold between metal and insulator in each pixel, a.k.a Tc, we calculate the pair connectivity correlation length in a series of images, as a function of different intensity thresholds. It quantifies how the probability that two pixels are in the same connected cluster decreases with distance. Near the critical point, the pair connectivity correlation length diverges, indicating long-range correlations. In Figure 3.8, we plot the evolu-

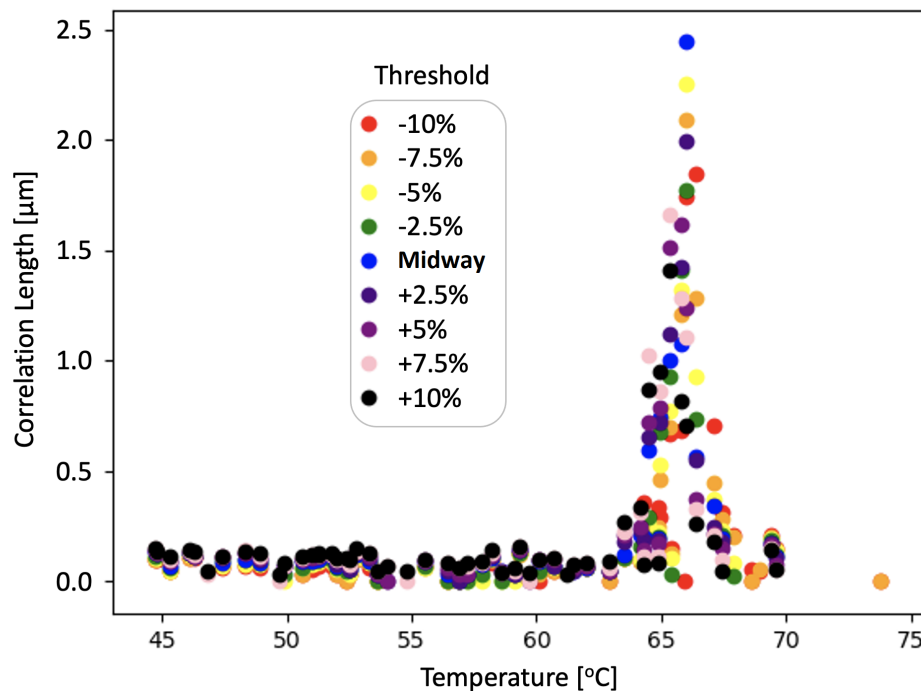


Figure 3.8 – Pair connectivity correlation length ξ_{pair} vs. temperature during the warming branch of an extremal hysteresis loop, as a function of different threshold values for determining metal and insulator domains in sample A. The correlation length diverges when the system is closest to criticality.

tion of the pair connectivity correlation length during the warming branch of a hysteresis loop. Circles are depicted with colors representing different threshold values. Each pixel’s threshold is set by a percentage of the difference between the saturated metal and saturated insulator values of intensity. Pixel’s threshold set at the midway point are depicted in blue for that temperature range and presents the longest correlation length.

Liu et al. in [170] studied spatial complexity in VO_2 during its IMT using SNOM images. They set the theoretical threshold according to the longest correlation length since it is an indicator of the system’s proximity to criticality. For this reason, we set the threshold at the midway point (blue circles in Figure 3.8). We verified this result computing the derivative to calculate the inflection point for each transition, and we found the same frame number.

Getting scaled and binary images

Scaled images are obtained by applying a linear normalization of the images to bring the intensity values to another range so there is consistency in the dynamic range for each set of images. The advantage of scaling the image is that it suppresses temperature-independent spatial variations that are not due to the IMT. The transformation takes each pixel of the 2D grayscale images $I : \{\mathbb{X} \subseteq \mathbb{R}^2\} \rightarrow \{Min, \dots, Max\}$ with intensity values in the range (Min, Max) into a new set of images $I_N : \{\mathbb{X} \subseteq \mathbb{R}^2\} \rightarrow \{NewMin, \dots, NewMax\}$ with intensity values in the range (0, 255).

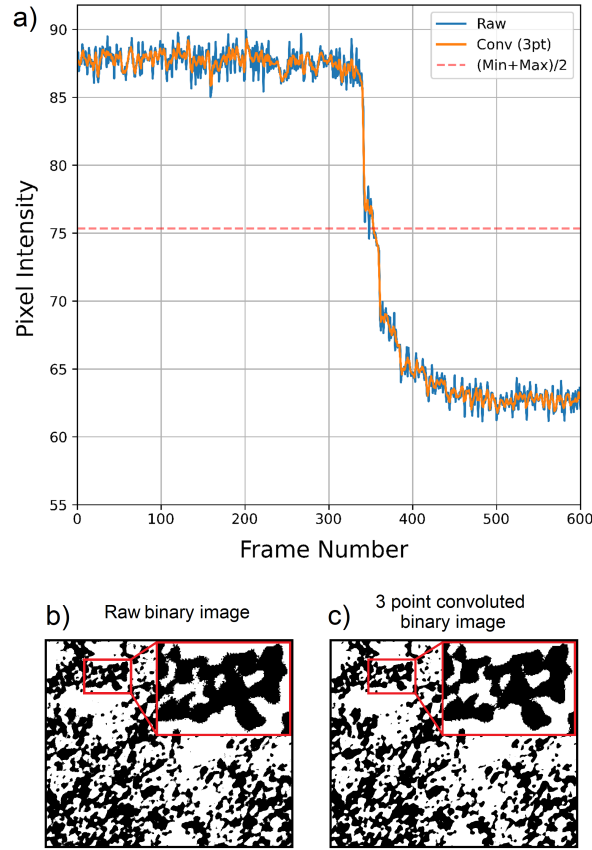


Figure 3.9 – (a) Single pixel time trace of intensity. The blue curve is the raw time trace of the measured optical intensity of pixel (127,734) in sample A. The orange curve is a Gaussian convolution ($\sigma=2.5$) of the same time trace over 3 frames. The double crossing at the midway is eliminated in the smoothed data set. (b) Binary black and white image (frame 260) of the sample generated by thresholding at midway the single pixel time traces as presented in (a). (c) Smoothed out binary black and white image (frame 260) of the sample generated by thresholding at midway the 3 frame convoluted single pixel time traces as presented in (a). Frame 260 map size is $33.6 \mu\text{m} \times 27.6 \mu\text{m}$.

The formula to compute the linear normalization is

$$I_N = (I - Min) \frac{NewMax - NewMin}{Max - Min} + NewMin \quad (3.7)$$

Binary images showing metallic and insulating domains are useful to track the dynamics and pattern formation during the IMT. We took the criterion discussed previously where every intensity value higher than T_c becomes a 1 (white, insulating), and every intensity lower than this threshold becomes a 0 (black, metallic).

2.3 Resolution limitation

The optical characterization method presented here, like all imaging techniques, is limited by its resolution. For example, the resolution of SNOM is 15 nm, while that of optical imaging is 300 nm. This means that any metal-insulator domains smaller than these resolutions will

be averaged within each pixel's signal. Given our pixel size of approximately 37 nm, signals from adjacent pixels will overlap and convolve, leading to a loss of finer details. This averaging effect is analogous to a real-space block renormalization procedure. In such a procedure, smaller structures are grouped into blocks, and their properties are averaged, simplifying the system by treating these blocks as single units.

3 Main achievements

This technique enables the optical measurement of phase separation, opening up new possibilities for studying this phenomenon. The development of an automatic image acquisition setup that operates while ramping the temperature enhances the efficiency and precision of data collection. Additionally, the workflow established for post-acquisition image processing, including alignment and obtaining single-pixel time traces, allows for the determination of local critical temperatures and the study of VO₂ dynamics.

High-resolution optical microscopy used in this technique permits measurements over longer length scales and finer temperature steps compared to other characterization methods. The technique can operate across a broad temperature range, from -195°C to 350°C , accommodating various experimental conditions. It also supports a wide range of sample sizes, from $10 \times 10\mu\text{m}$ up to $100 \times 100\mu\text{m}$, making it versatile for different research needs.

Chapter 4

Correlated maps to describe IMT in VO₂

In the previous chapter, we found the methodology for the optical characterization that allows us to obtain T_c for each single pixel of the analyzed sample for a complete hysteresis loop. Therefore, we can map T_c for all pixels for a warming, a cooling ramp, or both. By mapping T_c , we can identify the mean transition temperature and which areas of the sample switch at higher or lower temperatures. We can also map other features present in the hysteresis loop which provides a better description of the sample like the sharpness and broadness of the IMT. Those maps are going to be described in the subsequent sections.

A typical acquired optical image of VO₂ during its IMT is shown in Fig. 4.1 (a). This image corresponds to VO₂ in an insulating state (light gray) that will undergo a color change (dark gray) above T_c . The two gold electrodes are the trapezoidal pads in the upper and bottom of the image, and the darkest area corresponds to the sapphire substrate. The gold presents structures similarly to the VO₂ which are invariant with time. These inherent structural irregularities play a crucial role in facilitating image alignment through the utilization of the cross-correlation algorithm, thereby effectively compensating for any spatial drifts along the xy plane at the pixel level.

Once the whole set of images is aligned, we have the intensity value for each temperature assigned to a frame, what we refer to as single pixel intensity time trace (4.1 (b).) Given the susceptibility of grayscale values to fluctuations in illumination conditions, normalization of intensity is indispensable to ensure uniformity and accuracy in data representation.

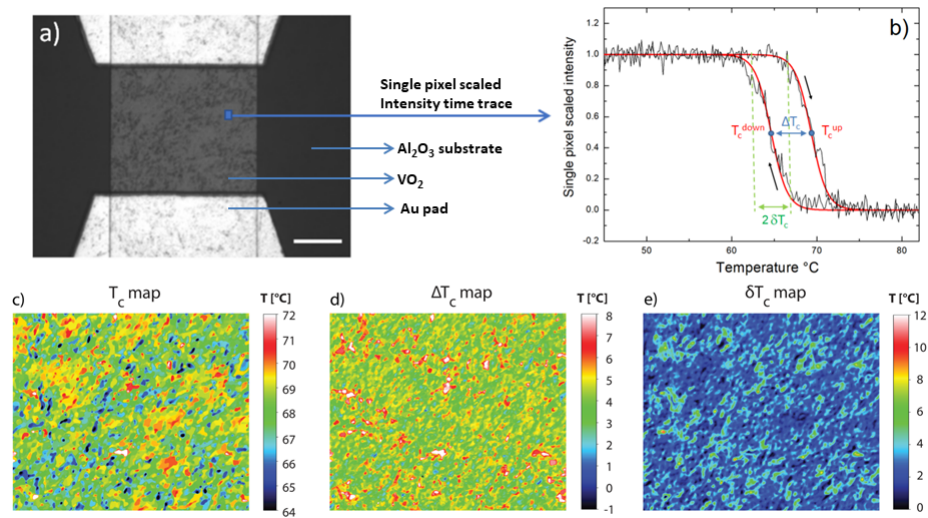


Figure 4.1 – (a) Optical image of VO₂ sample A during the insulator (light gray) to metal (dark gray) transition (warming cycle), two gold leads are seen at the top and bottom. These electrodes also display some structure (spots) due to gold surface imperfections. Sapphire substrate is the dark surface. Scale bar is 10 μm. (b) Single pixel intensity curve defining critical temperature T_c , hysteresis width ΔT_c and transition width δT_c . T_c were determined at midways as explained in the main text. Hysteresis width was determined by taking the temperature differences between heating and cooling cycles $T_c^{up} - T_c^{down}$. Transition width was determined by fitting (smooth curve) the single time trace to a hyperbolic tangent: $-\frac{1}{2}(\tanh(\frac{T-T_c}{\delta T_c})-1)$. (c) Local critical temperature T_c map, (d) ΔT_c maps, (e) δT_c map (presented here for the temperature ramping up branch). Image are 27.6 μm high. Histograms (with mean and standard deviation of maps a), b) and c) are shown in Fig. 4.2.

1 Transition temperature maps

The **local critical temperature** T_c map in VO₂ sample A is shown in Figure 4.1(c). This map shows a significant spatial variability in T_c , displaying intricate pattern formation across tens of microns, similar to SNOM sub-micron measurements [84] but acquired with a fast imaging speed that allows for a broader range of temperatures at finer time steps. During SNOM measurements, the tip could interact with the near-field of the sample, in contrast, the optical characterization method uses non-invasive illumination. The spatial variation in T_c coupled with the precise knowledge of where they are located can be exploited to optimize memory elements by addressing specific regions of the sample.

2 Hysteresis width maps

The **hysteresis width** ΔT_c map found in Fig. 4.1 (d) is obtained by subtracting $T_c^{up}-T_c^{down}$ (see the caption of Fig.4.1 (b) for the definition.) The average width is 4.3 ± 1.1 °C as seen in macroscopic transport measurements. Few regions have small ΔT_c , in the range [0 °C- 1°C] (small blue clusters in Fig. 4.1 (d)). Investigating these regions with other local probes could help understanding why this property occurs on certain areas of the sample. Hysteresis-free domains are promising for enhancing switching functionalities within optical and optoelectronic components. Previous research has demonstrated that a large hysteresis in VO₂ complicates its usage as an optical sensor [171].

3 Transition width maps

Fig. 4.1(e) displays **the transition width** δT_c map for sample A. The transition width gives information about how fast each pixel switches from insulating to metallic. It is calculated by fitting single pixel scaled intensity time traces to a hyperbolic tangent: $-\frac{1}{2}(\tanh(\frac{T-T_c}{\delta T_c})-1)$ as T_c is known from our time trace analysis. The average transition width of the pixels as measured in optics is 2.8 ± 1.1 °C with extremes from 0 °C to 8 °C. Some pixels show more than one step during a transition (see for example first pixel (305,300)). This phenomenon could be caused from the overlap between multiple metal or insulator domains influencing a single pixel or from structures smaller than the pixel size itself. As the pixel size is approximately 10 times smaller than the resolution, the complexity arises either from information from neighboring pixels affecting the signal at a given pixel. SNOM has observed inhomogeneities on scales smaller than those depicted in the optical maps [84].

A noteworthy observation is that the standard deviation of local T_c values across the sample, denoted as σT_c (1.2 °C), is smaller than the average transition width of pixels, δT_c (2.8 °C), as shown in the histograms of the maps (Fig. 4.2 (a) and (c)). An intriguing open question is whether the self-similar metal-insulator domain patterns discussed in [139] could account for this observed difference.

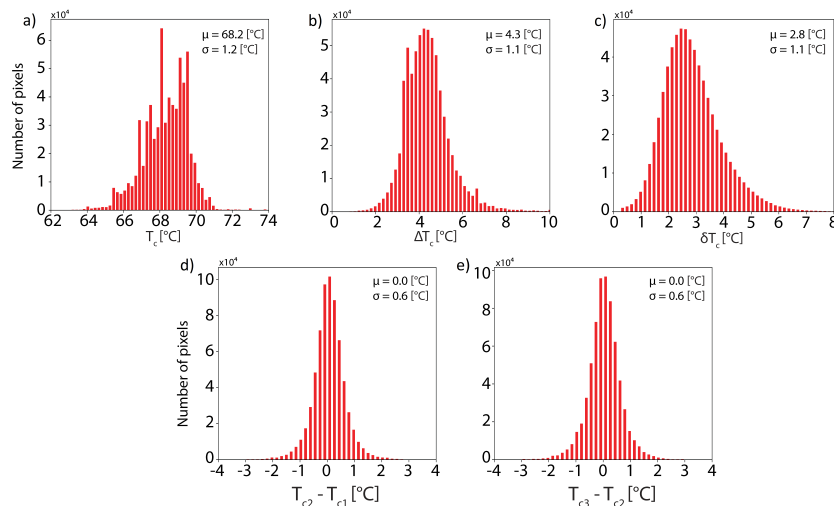


Figure 4.2 – Histograms of maps presented in Fig. 4.1 and 4.3. (a) T_c maps (upon warming); (b) ΔT_c map; (c) δT_c map and (d) and (e) two difference maps $T_{c2} - T_{c1}$ and $T_{c3} - T_{c2}$

4 T_c maps reproducibility

To study reproducibility, we set a temperature protocol consisting of three hysteresis loops at same temperature ramping rate. Then, we computed the difference between the T_c maps of the warming ramps of two consecutive loops (Figure 4.3). The warming ramps start at 38 °C up to 80 °C. The results are presented in the histograms of Figure 4.2(d) and 4.2(e). We observe that T_c remains unchanged for a vast pixels majority. In other words, T_c values are reoccurring at a particular location. Some pixels present an increment or decrement of the T_c , but its mean value prevails. The location and T_c of the nucleation sites triggers rapid changes in the electronic properties of the material leading to the formation of metallic patches reflected in the resistivity measurements.

A previous study in the macroscopic transport measurements of a VO₂ device reported discrete jumps in resistivity during the transition [172]. It may indicate that the transition occurs in avalanches rather than being a continuous process. Electrical measurements over 8 hysteresis loops show the most abrupt resistivity jumps occur at different temperatures from one cycle to the next one. The stochasticity is also observed in the optical T_c maps which suggests the patterns are strongly influenced by an underlying random field present in the thin film or substrate.

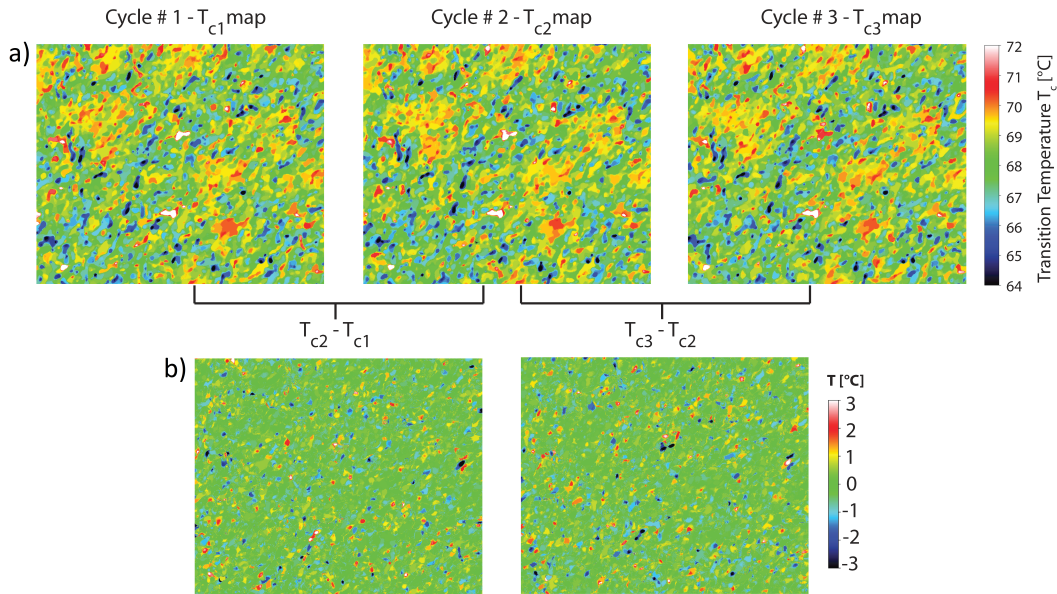


Figure 4.3 – (a) Three T_c maps while cycling through the IMT (warming) at $1^\circ\text{C}/\text{min}$. (b) Difference maps $T_{c2}-T_{c1}$ and $T_{c3}-T_{c2}$ between cycles. Global patterns are generally reproducible ($\sigma_{T_c}/T_c = 0.6^\circ\text{C}/68^\circ\text{C} = 1\%$). However some small regions present deviations up to $\pm 2^\circ\text{C}$. Maps size is $33.6 \mu\text{m} \times 27.6 \mu\text{m}$.

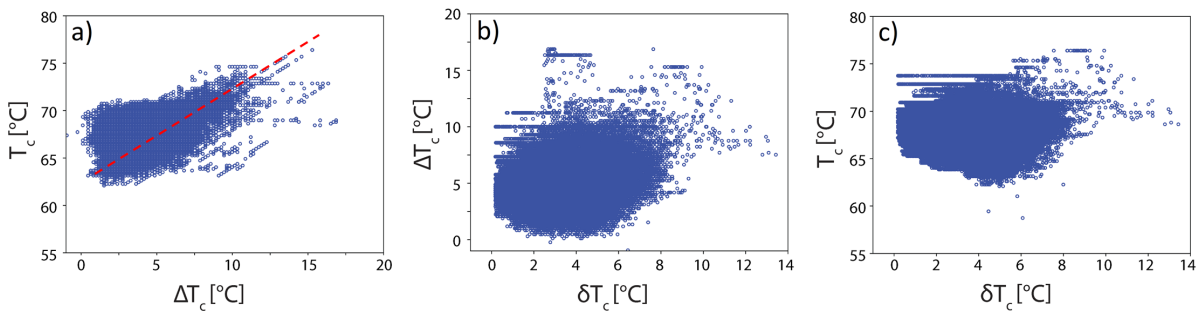


Figure 4.4 – Correlations between T_c (upon warming), ΔT_c and δT_c . Each of the 666,000 pixels (900×740) is represented. T_c vs. ΔT_c (panel (a)) shows a slight diagonal trend meaning that pixels with low T_c tend to have low ΔT_c (*i.e.* close to zero) and *vice versa* (see red dashed line.)

5 Correlations between maps

We present scatter plots relating the different features of the hysteresis loop T_c , ΔT_c , and δT_c to examine the correlations among them. Each point in the scatter plots presented in Fig. 4.4 is a pixel. The patterns that we observe in this correlation maps are mainly horizontal lines originating from multiple spatially close pixels switching at the same temperature during warming, and diagonal lines, arising from multiple adjacent pixels switching at the same temperature during cooling. While these patterns align with what is observed in avalanches, a more in-depth analysis is required to fully understand the underlying dynamics.

In the three correlation maps, no discernible trend is apparent in T_c vs. δT_c and ΔT_c vs. δT_c . However, T_c vs. ΔT_c reveals a slight positive correlation (see dashed red line in Fig. 4.4 (a).) This implies that pixels with low T_c tend to exhibit low ΔT_c values (i.e., close to zero), and conversely, pixels with high T_c tend to have higher ΔT_c . This positive correlation in Fig. 4.4(a) should not be confused with the few diagonal and horizontal lines in this panel due to finite temperature steps.

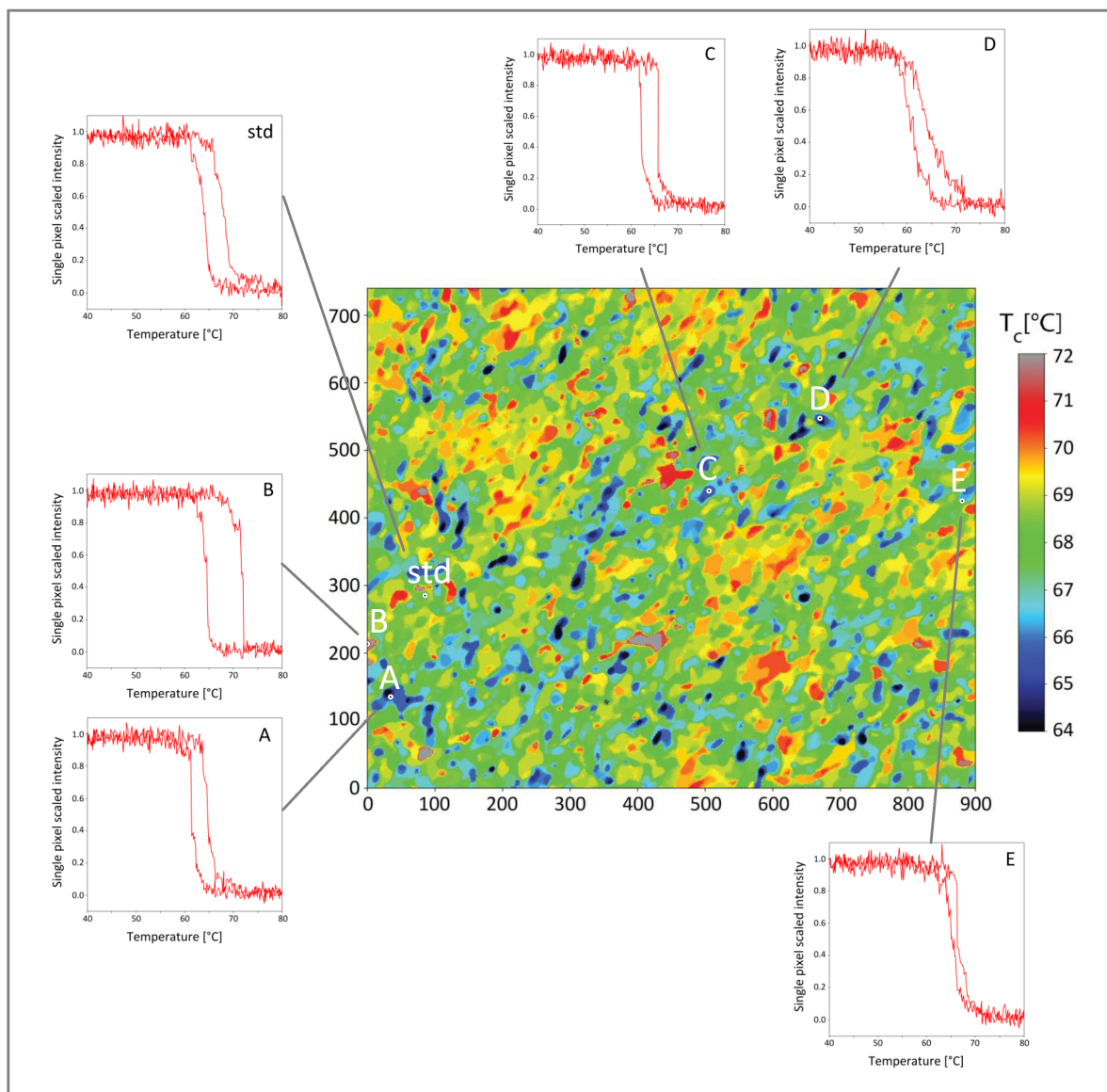
6 Deliberate pixel selection in search of specific thermal hysteresis characteristics

The pursuit of utilizing VO_2 in high-performance devices in practical applications has driven a continuous investigation into and customization of the physical properties of VO_2 through its IMT. For such applications i.e. neuromorphic devices, key parameters such as T_c , the abruptness of the transition, and the resistance difference between its metallic and insulating phases hold more importance. The maps described in the section above (Fig. 4.1 c, d and e) present a spatial differentiation of those key parameters so we are able to identify parts of the sample (each pixel in the map) with desired thermal hysteresis characteristics. Some pixels in the map present two steps during the IMT, which can be detected from their anomalously high error on the fit to the hyperbolic tangent function when computing δT_c .

Figure 4.5 shows the T_c map of the sample A with six pixels displaying different properties. The characteristics that we are presenting within these six pixels are not exclusive to the 37nm square pixel location; rather, they are applicable to numerous pixels around the xy coordinates reported. The pixel designated as “std” (representing standard) exhibits a transitioning profile with T_c , ΔT_c , and δT_c values close to the average values observed in the distribution of these three parameters (refer to Fig. 4.2 a, b, and c).

Pixels A and B show the most common type of local characteristics found in the maps: when T_c is high, ΔT_c is high; when T_c is low, ΔT_c is low. This positive correlation is evident at a global level in Fig. 4.4 (a). However, on a local level, individual pixels can have a large deviation from the global average behavior. Pixel A characteristics could be used in optical memory-type applications since it has a large ΔT_c , and Pixel B characteristics are useful for VO_2 sensors (bolometers) in which a small hysteresis width is preferable [173].

Pixel E displays an exceptionally low ΔT_c ($0.3\text{ }^\circ\text{C}$) with a relatively low T_c ($66.3\text{ }^\circ\text{C}$) closer



Label	(x,y) position	Specific characteristic	T_c [°C]	ΔT_c [°C]	δT_c [°C]
std (standard)	(85 , 285)	T_c , ΔT_c , δT_c close to mean value	68.0	4.1	2.6
A	(34 , 135)	Low T_c / Low ΔT_c	64.8	3.5	1.6
B	(0 , 213)	High T_c / High ΔT_c	71.7	7.2	1.5
C	(506 , 440)	Low δT_c	65.7	3.8	0.4
D	(670 , 547)	High δT_c	64.2	2.9	5.1
E	(880 , 425)	Very low ΔT_c	66.3	0.7	1.9

Figure 4.5 – T_c map ($33.6 \mu\text{m} \times 27.6 \mu\text{m}$) with six pixels chosen to illustrate specific characteristics in the hysteresis loops. The table shows the numerical values of T_c , ΔT_c and δT_c for each pixel. The numbers in bold highlight the unique characteristic of each pixel.

to the mean value of the map. This case where ΔT_c is within the lower values [0 °C -1 °C] presents an almost non-hysteretic behavior. Small hysteresis width in opto-electronic devices prevents optical detectors improves the temperature response of the switching between heating and cooling cycles [171] [174]. Likewise, in neuromorphic devices, small hysteresis allows lowering the voltage threshold needed for spiking [175].

Pixels C and D illustrate the case where the width δT_c of the transition is sharp (0.5 °C) or significantly wide (5 °C). Pixel C specifically exemplifies a sharply transitioning pixel, where the transition unfolds in an avalanche-like manner within temperature steps of 0.17 °C . A more detailed examination to identify the locations and mechanisms of these avalanches will be pursued in future work.

7 Analysis of parameters involved in the IMT

The maps discussed in the preceding sections were derived from samples prepared via the RF sputtering method (Sample A), offering numerous advantages inherent to physical deposition techniques. These benefits include the attainment of a uniform coating, precise control over film thickness, and the deposition of highly pure materials [176]. However, given the absence of commercially available thin-film VO₂ samples and our interest in exploring alternative characteristics, our research group at LPEM opted to embark on sample preparation using a sol-gel method.

The sol-gel method, a wet chemical approach to thin-film coating fabrication, offers distinct advantages over physical vapor deposition techniques. Notably, it stands out for its economic viability and straightforward implementation, contrasting with the complexity and facility-intensive nature of physical vapor deposition processes. Furthermore, the chemical manipulation inherent to the sol-gel method enables the synthesis of new functional compositions, rendering it more conducive to tailored material design compared to conventional methods like PVD.

We characterized electrically and optically two VO₂ samples of different thicknesses Sample B and Sample C, both synthesized on a c-cut substrate following the sol-gel synthesis method described in Chapter 2. From the XRD measurements, we found that sample B exhibits a well-defined crystallographic orientation (epitaxy), whereas sample C shows a non-epitaxial structure (Fig. 4.6(a)). The electrical characterization of the samples shows a resistance drop of three orders of magnitude for both the epitaxy and the non-epitaxy during the IMT. The epitaxial sample exhibits a lower resistance in its insulating state as well.

Differential resistivity-temperature curves were plotted to extract IMT features (Fig. 4.6(c) and (d)). The hysteresis loop parameters derived from these measurements indicate that the non-epitaxy sample has a broader transition width and a notably higher T_c (20 °C) upon heat-

Sample Code	Substrate	Preparation method	Thickness[nm]	Transition temperature T _c [°C]	Width of hysteresis ΔT_c [°C]	Sharpness δT_c [°C]	Resistance change
A	r-cut	RF magnetron sputtering	100	68.2	4.3±1.1	2.8±1.1	10 ⁴
B	c-cut	sol-gel	84	66	7.9±0.4	6.2±0.3	10 ³
C	c-cut	sol-gel	136	86	23.9±2.2	5.7± 0.9	10 ³

Table 4.1 – IMT characteristics of VO₂ thin films on Sapphire substrates.

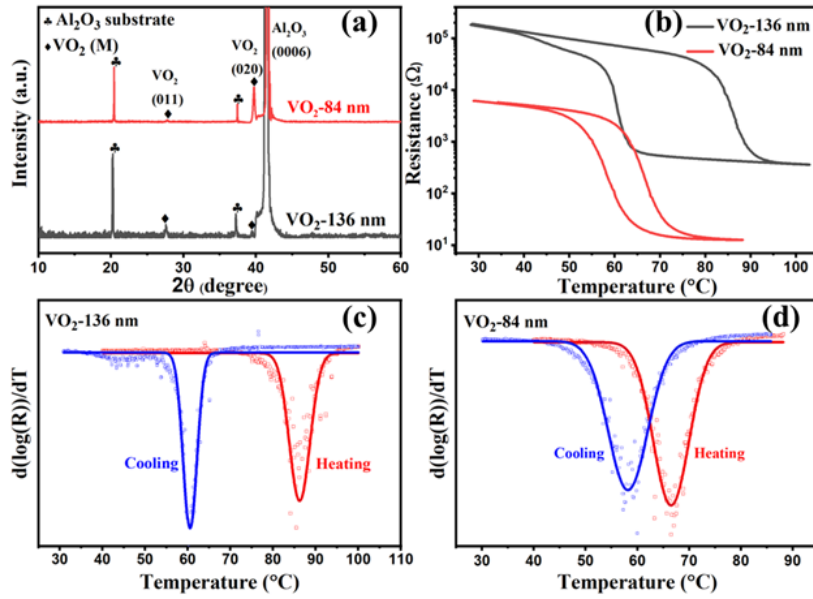


Figure 4.6 – (a) Room temperature XRD patterns of VO₂: Sample B epitaxy (preferentially oriented, red curve) and Sample C non epitaxy (gray curve). (b) Hysteresis loop of Sample B (gray curve) and Sample C (red curve). (c) and (d) Critical temperature values T_c^{up} , T_c^{down} , and ΔT_c , derived from the electrical characterization of Sample B and C respectively.

ing. The thinner sample displays transition temperatures of 58 °C during cooling and 66 °C during heating, whereas the thicker sample exhibits temperatures of 61 °C and 86 °C during the respective processes. This implies distinctive electrical and structural behaviors between the epitaxial and non-epitaxial VO₂ samples. A study on the epitaxial growth of VO₂ films on sapphire demonstrated that it significantly influences the hysteresis loop width and the transition temperature [177].

We generated T_c maps and histograms for a sample area measuring $15\mu\text{m} \times 15\mu\text{m}$ to analyze hysteresis loop characteristics and leverage spatial information obtained through optical characterization. In Figure 4.7(a), the epitaxial sample exhibits a more uniform map over a 10 °C range compared to the non-epitaxial sample shown in Figure 4.7(b). This trend is also evident in the histograms presented in Figure 4.8, where the non-epitaxial sample displays a broader distribution with an average ΔT_c of 23.9 ± 2 °C, while the epitaxial sample has a narrower distribution with an average ΔT_c of 7.9 ± 0.4 °C.

Furthermore, the sharpness of the transition, represented by δT_c , is more pronounced in the non-epitaxial sample. Although the average difference in δT_c between the non-epitaxial and epitaxial samples is less than 1 °C, certain pixels in the non-epitaxial sample undergo faster transitions (< 5 °C.)

Both the substrate and the growth process influence and affect the overall properties of VO₂ films, since they affect the growth orientation and surface morphology of the samples. Yang et al. in [44] realized a comparative study between VO₂ thin films grown on r-cut and c-cut. They found that r-cut samples presented a lower transition width and a sharper switching. This

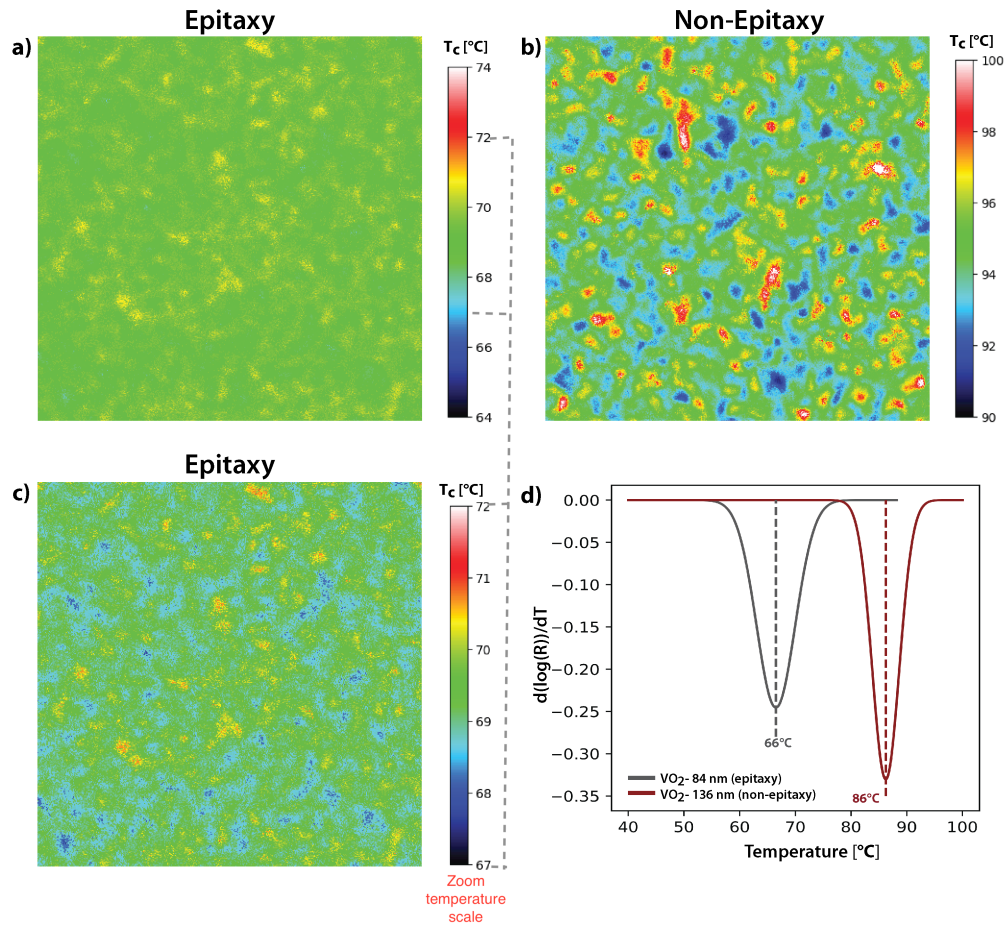


Figure 4.7 – T_c maps of VO_2 samples: (a) Sample B Preferentially oriented (Epitaxy), (b) Sample C Non preferentially oriented (Non epitaxy) at the same scale (temperature range of 10 °C), (c) Zoom over the range of temperatures for the epitaxy samples. It is observed that the epitaxy sample is more homogenous in T_c values over a range of 10 °C than the non epitaxy one. The analyzed area of the VO_2 samples is $15 \mu\text{m} \times 15 \mu\text{m}$.

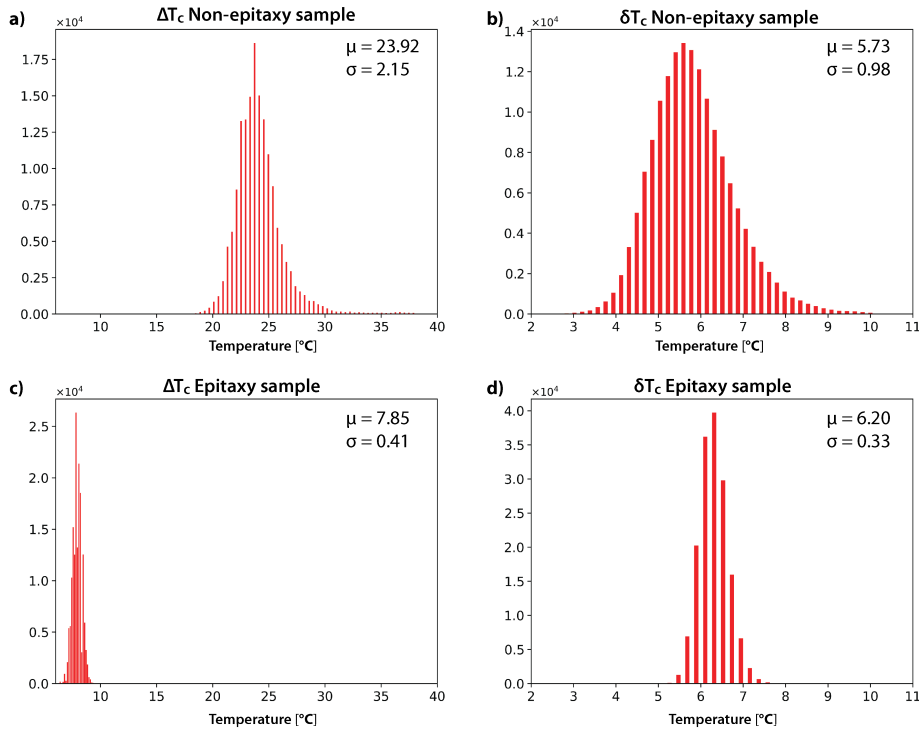


Figure 4.8 – Histograms of VO₂ samples: (a) Sample C ΔT_c of , (b) Sample C δT_c , (c) Sample B ΔT_c at same scale, to show the sharpness difference in the distribution of the samples B and C, (d) Sample B δT_c .

was attributed to c-cut samples having a broader range of nucleation barriers, resulting in a transition occurring over a wider temperature range and by a higher-in plane misorientation between the grains.

The hysteresis width in VO₂ films is closely associated with the nature of grain boundaries, as discussed by Zhang et al. [178]. Specifically, a smaller transversal grain size corresponds to a larger ΔT_c . Conversely, as the transverse grain size diminishes, the likelihood of heterogeneous nucleation decreases, leading to an increase in the hysteresis loop width. Additionally, the role of elastic stresses accompanying the phase transition becomes more pronounced with decreasing grain sizes [179].

In this work, variations in the shape and width of the hysteresis loop could be driven by changes in film thickness. The impact of strains generated during the phase transition becomes more prominent as the film thickness decreases. In the case of very thin films, the appearance of a hysteresis loop with two steps can be elucidated by considering that vanadium dioxide resides in two crystallographic orientations [180]. For instance, the c-axis may align with the substrate plane in some grains while being perpendicular in others. We can observe a bump in the cooling branch hysteresis graph of the non-epitaxy sample that could be explained by the formation of a metastable between the monoclinic (M1) and rutile (R) phases [181].

8 Main achievements

The main achievements of our study encompass three key aspects. Firstly, we successfully mapped the critical temperature (T_c), the width of the phase transition ΔT_c , and the sharpness of the transition (δT_c) of VO₂ samples. This was achieved by tracking the intensity of each pixel over time, thus providing both spatial and dynamic insights into the transition process. This mapping not only offers an understanding of the transition behavior but also sheds light on the intricate interplay of factors influencing the phase transition dynamics.

Secondly, our research shows the potential for tailoring sample characteristics to suit diverse applications, particularly for memory and fast switching functionalities, which are of importance in neuromorphic computing paradigms. By discerning the distinct requirements for these applications, we can strategically select VO₂ samples with specific properties optimized for desired functionalities. This flexibility in sample design opens up new opportunities for the development of neuromorphic computing systems with enhanced performance and efficiency.

Lastly, this method allows the characterization of VO₂ samples synthesized through different techniques. By obtaining statistical information for each segment of the sample, we gain valuable insights into the influence of various preparation methods on the material properties and transition characteristics. This systematic approach not only enriches our understanding of VO₂ behavior but also provides valuable guidance for optimizing sample fabrication processes to achieve desired performance metrics.

Chapter 5

Ramp Reversal Memory

Neuromorphic computing is presenting new paradigms for electronic devices tailored for artificial intelligence Artificial Intelligence (AI) applications. At the core of cognitive functions lies memory - the ability to encode, retain, and recall information. In biological neural networks, memory hinges on synaptic weights, representing the strength of connections between nodes. Similarly, AI algorithms draw inspiration from this biological blueprint.

Among the contenders aiming to replicate synaptic functionality, Phase Change Material PCM devices offer precise control over conductance levels through reversible phase changes. This versatility in phase modulation lays the groundwork for exploring resistance shifts, when looking for alternatives in memory research.

While previous studies have explored memory effects in strongly correlated materials such as manganites, it wasn't until 2017 [182] that Ramp Reversal Memory (RRM), a non-volatile memory effect, was reported in VO₂ and NdNiO₃. This effect, characterized by resistance increase at specific temperatures, manifests during the IMT induced by reversing the temperature ramp from heating to cooling. As explained in the introduction, this potentially allows creating a neuristor and synaptor in a single material.

Having a non-volatile memory in VO₂ means that the output resistance at a specific temperature is dependent on the past resistance level in the previous temperature ramp and this effect is retained until a high temperature far from T_c is applied. The RRM temperature protocol followed to achieve this memory effect is explained in more details in the subsequent sections.

Several conditions must align for the RRM, according to a heuristic model based on three properties commonly observed in temperature-driven first-order phase transitions of correlated oxide thin films found in [183]. Firstly, spatial phase separation must occur, delineating discernible insulating and metallic patches. Secondly, electronic phase transition correlates with a crystallographic reorientation from monoclinic insulating to tetragonal metallic structural arrangements. Finally, strain alterations influence the critical temperature, further modulating memory behavior. A microscopic origin has been put forward but needs to be validated.

To do so, our optical characterization provides invaluable spatial insights, unraveling the localization and aggregation of distinct phases. In the scope of RRM, this spatial resolution

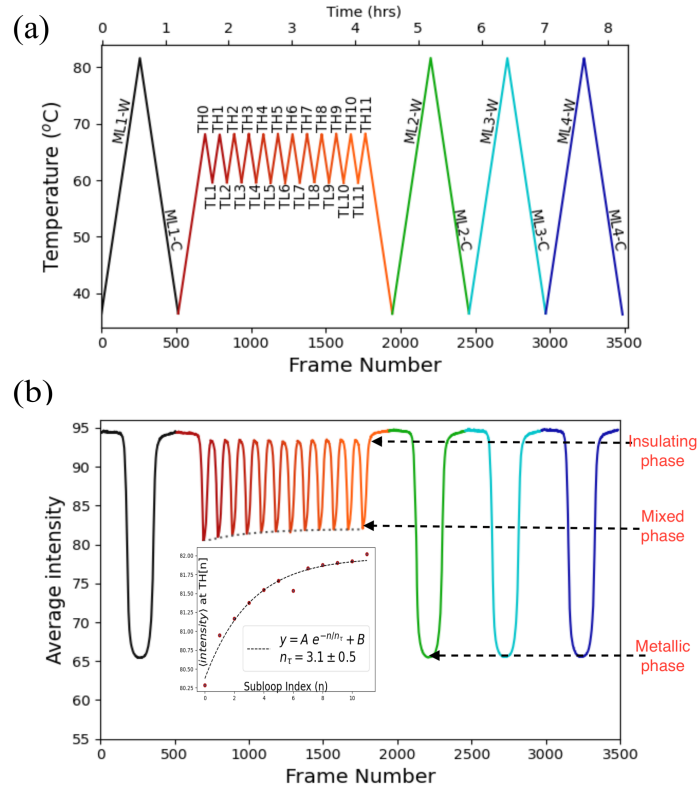


Figure 5.1 – (a) Ramp Reversal temperature protocol. Major loop labels are as follows: ML1-W stands for Major Loop 1 upon warming; ML1-C stands for Major Loop 1 upon cooling, and similarly for other major loops. In the subloops, temperature is varied repeatedly between a low temperature of $TL_n = 59.5^\circ\text{C}$ and a high temperature of $TH_n = 68^\circ\text{C}$, through a total of $n=11$ complete subloops. (b) Average intensity *vs.* frame number. Intensity is on a grayscale of 0 (black) to 255 (white), after accounting for illumination variation (detailed elsewhere). The light gray dashed line follows the average intensity at the end of each subloop. Inset: Fit of the average intensity at the end of each subloop (*i.e.* at TH_n), *vs.* subloop index n , to an exponential saturation. The time constant is $n_\tau = 3.1 \pm 0.5$ subloops.

yields a non-volatile memory framework capable of spatially resolving memory states. Moreover, this technique not only elucidates memory encoding mechanisms in VO_2 but also serves as a tool for identifying defects and knowing areas of increased critical temperature (T_c).

In the following sections, we present details on the RRM protocol followed for the measurements and image acquisition of this effect in VO_2 sample A, the accumulated memory maps, and changes in the critical temperature maps, as well as a point defect model in collaboration with Purdue university.

1 Following the Ramp Reversal Memory temperature protocol

We based the temperature protocol on the report by Vardi et al. where they observed a non-volatile memory effect on VO_2 and NdNiO_3 . This protocol is described in Fig. 5.1(a). Initially, we go through a warming-cooling cycle, where the sample starts from a completely

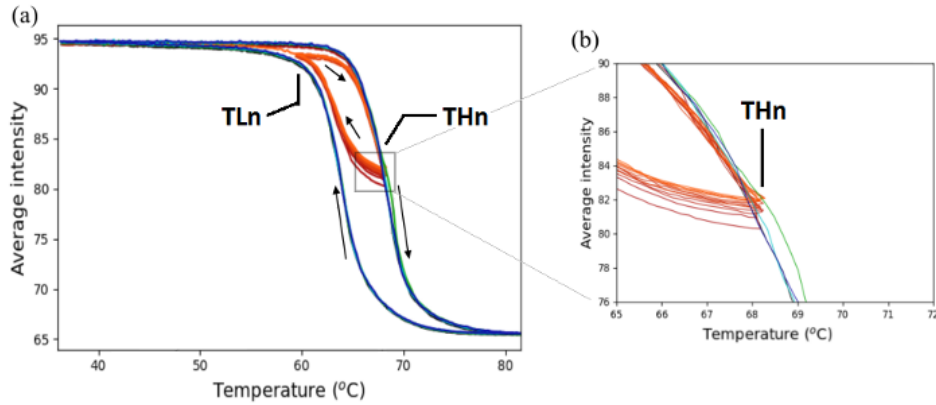


Figure 5.2 – (a) Hysteresis curves of average intensity *vs.* temperature throughout the Ramp Reversal protocol of Fig. 5.1. (b) Zoom showing the progressive increase after each subloop of the averaged intensity around the high temperature turning point $TH=68^{\circ}C$.

insulating to a fully metallic state, and then back again (ML1) in the temperature range of $38^{\circ}C - 80^{\circ}C$. This cycle occurs between frames 1 and 500. Subsequently, a sequence of temperature cycles, referred to as minor loops, is performed, wherein the warming ramp ascends to a specified peak temperature within the transition region, denoted as TH, and descends to TL during each minor loop iteration. This sequence occurs between frames 500 and 1900. At TH, the transition partially occurred and the VO_2 junction is a mixing of metallic and insulating phases. Following the end of the last minor loop, three subsequent major loops (ML2, ML3, and ML4) are performed (corresponding to frames 2000 to 3500 approximately.)

During the whole protocol we acquired micrographs of Sample A with the method described in Chapter 3 and we also recorded the resistance of the junction simultaneously. By examining the relationship between average intensity and temperature across all images in the protocol, we observe a RRM with similar features to the one shown in [182], which depicted resistance rather than reflectivity. The average intensity of the images is plotted in Fig. 5.1(b) as a function of the frame number and in Fig. 5.2 as a function of the temperature. During the first major cycle loop, the intensity drops from 95 in the insulating phase to 65 in the metallic phase. We note the increment in average intensity implying a concurrent increase in resistance across each subloop. Furthermore, this elevation in average intensity adheres to an exponential trend, as evidenced by the fitting showcased in Fig. 5.1 (b) inset. In the hysteresis graph, the average intensity at TH exhibits a evident rise as the bump of the red/orange/green curves. This can be seen in Fig. 5.2 (a) and zoomed-in portion (b).

During the sequence of minor loops, the intensity drops from 93 (at TLn) to a value situated between 80 and 82 (at THn). A plot of the evolution of the average intensity at each TH is shown in Fig. 5.1 (b) inset. The intensity is not varying randomly, it is following a monotonic increase, although the junction was heated up to the same value TH. This is also visible in Fig.

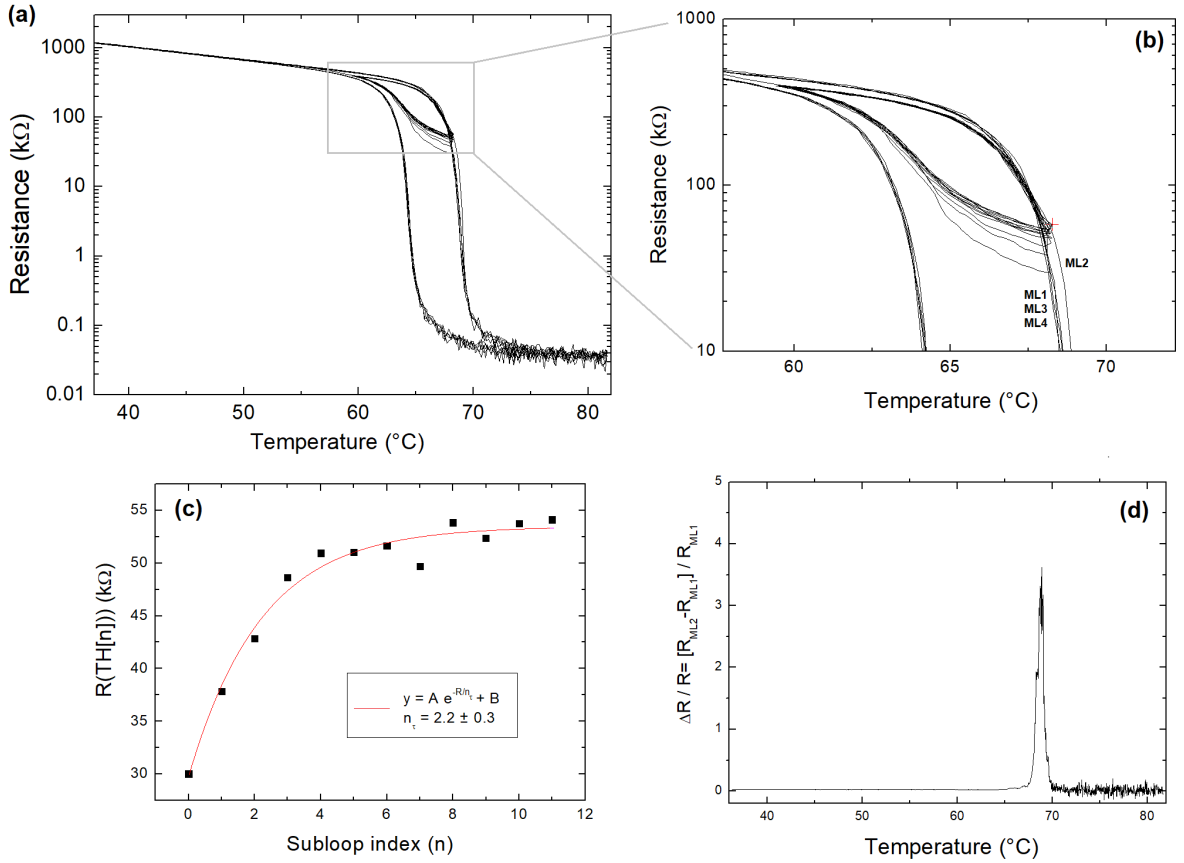


Figure 5.3 – (a) and (b) $R(T)$ measurement of the metal-insulator transition during the full ramp reversal sweep. ML1, ML3, ML4 curves overlap as seen previously.^[182] (c) At TH=68°C, resistance rises from 30kΩ at TH0 to 53kΩ at TH11 with a characteristic time of 2.2 subloops. (d) $\Delta R/R$ between ML1 and ML2 reaches 350% increase around 68.8°C.

5.2(b) with the shifts of the red, orange and green curves. This indicates that we have less metallic domains formed within the junction.

The increase of the intensity during the sequence of subloops can be fitted as an exponential function:

$$y = Ae^{-n/n_\tau} + B \quad (5.1)$$

As previously observed in [182], resistance increases at each TH turning point. This trend is shown in Fig. 5.3(b). From the fit, we find $n_\tau = 3.1 \pm 0.3$ subloops. Simultaneously, the same effect is observed in the resistance measurements, shown in Fig. 5.3(a) and Fig. 5.3(b). In that case, the measured characteristic time is $n_{\tau R} = 2.2 \pm 0.3$ subloops (see a fit in Fig. 5.3(c)), which is very similar to the optical measurement. Physically, this means that at every subloop, we have less metallic domain formed in the junction. Every time a subloop is performed, a fraction of the grains in the junction remains insulating, and the resistance increases although the temperature is the same. This is an evidence of the memory effect in VO₂.

Furthermore, let us now have a look at the second major loop (ML2), performed just after the

minor loop sequence. This loop is represented by the green curve in Figs. 5.1 and 5.2. We can see that near and above TH, the average intensity and the resistance are shifted from the original major loop curve (ML1, represented by the black curves). This second major loop is therefore different from the first one, as it was influenced by the subloop sequence and the structural modification of the VO₂ junction. **To recover the initial behavior, the junction has to be heated up further than TH in order to erase the memory effect.** This is confirmed by making other major loops (ML3 and ML4) that perfectly superimpose to the first one ML1. The amplitude of the memory effect is characterized by the difference in resistance (ΔR) between ML1 and ML2. We plotted in Fig. 5.3(d), the evolution of $\Delta R/R$ as a function of temperature. We have a maximum normalized difference equal to 3.5 at the transition temperature 68.8 °C. This value is much larger than the one reported in ref [182] where only 0.2 was measured.

Consequently, the memory observed in resistivity curves in this sample is found to be 17 times stronger and 6 times faster than reported previously. Discrepancies could arise from various factors such as sample preparation details, ramp speed, or variations in the turning point temperature.

We tested the effect of RRM at different temperature rates (0.2 °C/min, 0.4 °C/min, 0.6 °C/min, 0.8 °C/min, and 1 °C/min), and computed the time constant and amplitude to study changes in memory capacity, finding they are independent on the temperature rate. Also, doing a reverse ramp reversal, meaning going from a high temperature beyond the transition and cooling to a lower temperature does not have memory effect.

2 Finding T_c maps differences with RRM

Once we processed the entire set of images, we obtained T_c maps for the major loops to analyze the spatial changes in local T_c before and after applying the RRM protocol. In Fig. 5.4(a), the T_c maps of ML1 in the warming branch are depicted before the application of 11 subloops, while Fig. 5.4(b) illustrates ML2 in the warming branch immediately after the subloops. A noticeable increase in the ruggedness of the T_c map is observed after the subloops, indicative of the accumulated RRM, which is evident in the increase of yellow, orange and red regions in ML2-W, as also evidenced by the broader distribution found in the histogram of Fig. 5.4(c). Examining the distribution, the average T_c is slightly shifted from 68.12 °C to a higher temperature (68.36 °C), consistent with the increase in average intensity. The elevation of both local T_c and the standard deviation (σ , representing ruggedness) of ML2-W demonstrates these metrics are adequate in gauging the ramp reversal memory state. In panel (d), we first see the increase on average T_c and σ after the RRM training at the warming branch of ML2-W. Then upon heating the sample at 80 °C much higher than the local T_c, the average T_c and σ values for ML3 and ML4 warming branches values revert to pre-subloop, indicating a reset and erasure of the memory effect.

We also calculated the disparity between the T_c maps of the warming branches of the first major cycle before subloops and the last reset major cycle (ML4-W - ML1-W, Fig. 5.5(a)), and the latter with the major loop just after subloops (ML4-W - ML2-W, Fig. 5.5(c).) The

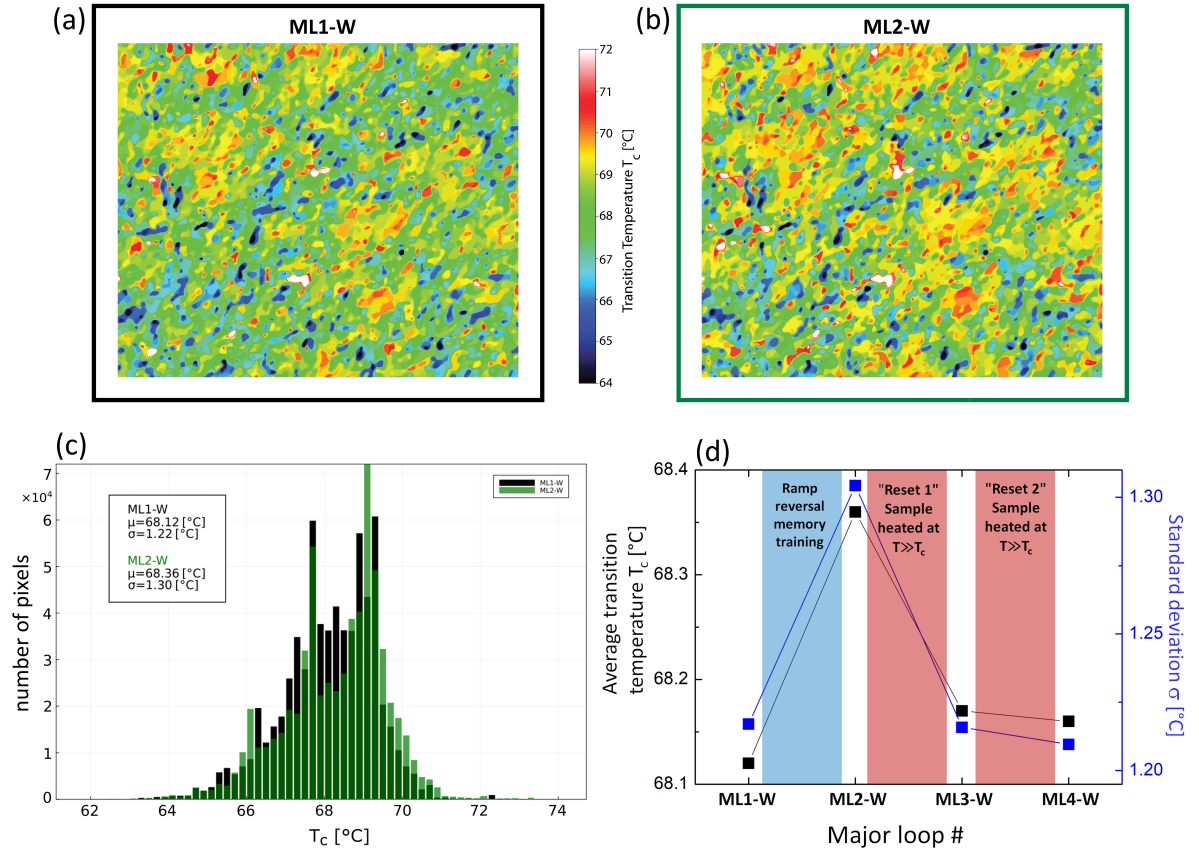


Figure 5.4 – (a) T_c map acquired during the warming branch of the first major loop (called ML1-W). The analyzed area of the VO_2 sample has a map size of $33.6 \mu\text{m} \times 28 \mu\text{m}$ ($900 \text{ pixels} \times 750 \text{ pixels}$). (b) T_c map acquired during the warming branch of the second major loop (ML2-W) after 11 subloops memory training. (c) Histograms of ML1-W and ML2-W maps. (d) Plot of the average transition temperature and standard deviation for all 4 major loops.

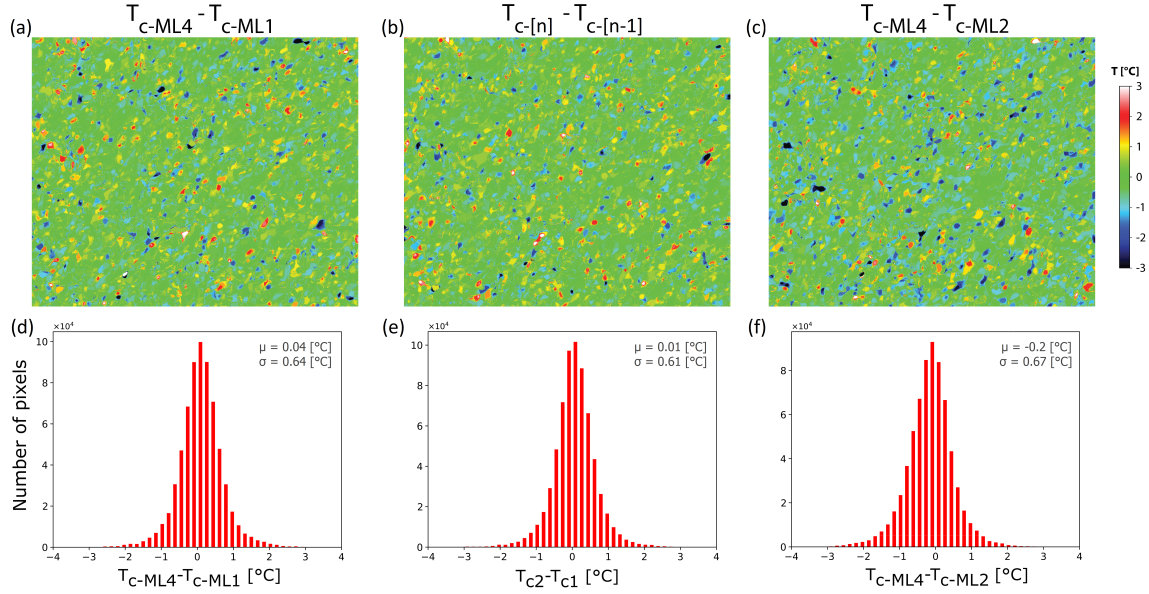


Figure 5.5 – (a) Difference in T_c maps between ML4-W and ML1-W. (b) Difference in T_c maps when cycling through two transition [n] and [n-1] as presented in Chapter 3; (c) Difference in T_c maps between ML4-W and ML2-W (*i.e.* with ramp reversal memory). Panels (d) (e) and (f) are corresponding histograms. Maps size is $33.6 \mu\text{m} \times 28 \mu\text{m}$ ($900 \text{ pixels} \times 750 \text{ pixels}$).

ML4-ML1 map and histogram (panels a and d) are centered around zero, with a σ of 0.6 °C. This closely resembles the map and histogram observed during a simple reproducibility test (panels b and e) outlined in Chapter 4 (Fig. 4.2.) When intrinsic memory is present (panels c and f), the average T_c , μ , is shifted by -0.2 °C. This suggests that the ramp reversal memory was entirely erased after subjecting the sample to high temperatures, within the fluctuations and stochasticity from one cycle to the next one characteristic of this material.

Merely examining the T_c maps makes it challenging to discern areas where there is a slight increase or decrease in T_c between cycles. To pinpoint spatial changes in T_c locally, we conducted thresholded differences between the T_c maps (Fig. 5.6 (b)). Regions exhibiting an increase in T_c are highlighted in red, while those showing a decrease are in blue. This approach provides visual insights into regions where memory accumulates in ML2-W (here, once again the increase of the insulating phase as an increase in T_c is clear), and where it is erased in ML4, complementing the information gleaned from histograms.

Figure 5.7 presents a more detailed insight into the memorization process through a four-color map, distinguishing regions where T_c is originally higher or lower than average and whether it increases or decreases during ramp reversal. The coexistence of all four possibilities underscores the complexity of this process. Panel (c) highlights numerous regions within insulating clusters at TH where high T_c values increase (orange), and within metallic clusters where low T_c values diminish (cyan). Conversely, examples of the opposite behavior (dark and light gray) are also observed. This indicates that memory is store throughout the sample, encompassing areas near metal-insulator boundaries at TH as well as deep within these clusters.

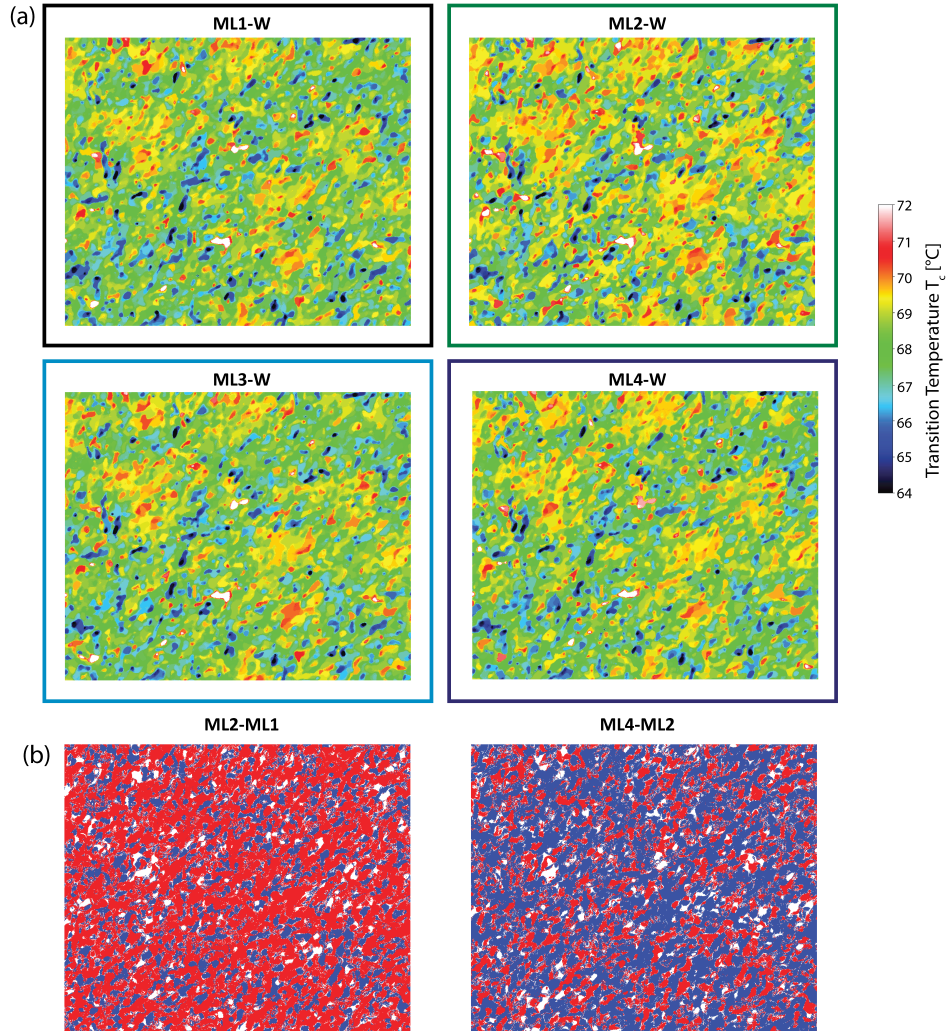


Figure 5.6 – (a) T_c maps from ML1-W and ML2-W (as shown in Fig. 5.4) side by side with T_c maps ML3-W and ML4W after ramping the sample to high temperatures. The frame color code (green or black) is the same as in Fig. 5.1 and Fig. 5.4. (b) Thresholded difference between the T_c maps of ML1-W and ML2-W (left panel) and between ML4-W and ML2-W (right panel). T_c has risen in red regions and has lowered in blue regions. White regions ($\pm 0.1^\circ\text{C}$ around 0°C) identify where T_c only changes within the temperature resolution ($\sim 0.17^\circ\text{C}$), and thus the temperature remains the same within error bars. Maps size is $33.6 \mu\text{m} \times 28 \mu\text{m}$ (900 pixels \times 750 pixels).

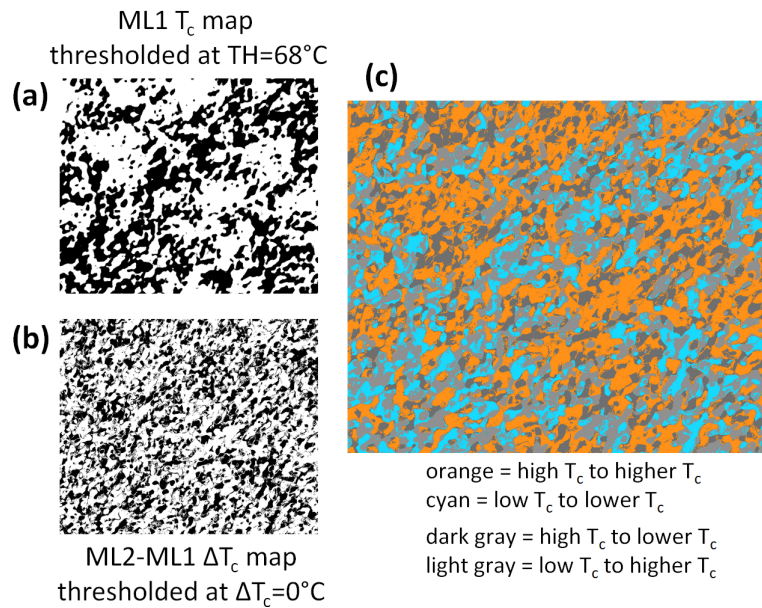


Figure 5.7 – Experimental ML1-W maps thresholded at the average $T_c = 68.13^\circ\text{C}$. White patches have high T_c ; black patches have low T_c . (b) Difference between ML2-W and ML1-W T_c maps, thresholded at $\Delta T_c=0^\circ\text{C}$. White patches in this panel, T_c became higher when passing from ML1 to ML2; Black patches, T_c became lower when passing from ML1 to ML2. (b) incorporating temperature resolution considerations. A two color difference map is used here for simplicity. (c) 4 color maps using (a) and (b). Orange patches have a high ML1 T_c and an even higher T_c in ML2. Cyan patches have a low ML1 T_c and an even lower ML2 T_c . In dark gray regions, a high ML1 T_c changed to a lower ML2 T_c . In light gray regions, a low ML1 T_c changed to a higher ML2 T_c . As the sample is cycled through the ramp reversal protocol, some extreme T_c 's become more extreme as seen by the presence of orange and cyan patches in (c). Maps size is $33.6 \mu\text{m} \times 28 \mu\text{m}$ (900 pixels \times 750 pixels).

3 Mapping memory accumulation

In a similar fashion to observing spatial hysteresis features, we discern the accumulation of memory within the sample during the minor loops. To obtain the memory maps, we employ thresholded images that only present the metallic and insulating phases, following the methodology outlined in Chapter 3. Figure 5.8 illustrates the initial state corresponding to the image at TH0, with a pixel count revealing a comparable quantity of pixels in both metallic and insulating states. After, each image is compared to TH0, retaining the same color for pixels exhibiting sustained metallic or insulating properties, while newly formed phases are highlighted in yellow (insulator) and blue (metallic). This allows us to observe the augmentation of insulating patches and their distribution. The memory probe, ML2, denotes the sample state with the highest memory accumulation. Following major loops reset to a balance of insulating and metallic patches. To validate these findings, ML3-W and ML4-W are compared to ML1-W, which takes place before the memory training, leading to consistent conclusions.

Successive panels illustrate the evolution of metal and insulator domains at the end of every other subloop TH_n, from n = 2 to n = 10, relative to TH0. Unchanged pixels are shaded dark or light grey depending on their metallic or insulating nature, while yellow and blue indicate the growth of insulating and metallic patches, respectively. On average, the sample gradually transitions to a more insulating state with subloop training, although specific regions exhibit a metallic shift.

ML2(TH)-TH0, labeled "Memory probe," represents the state with the most accumulated memory patches, coinciding with the highest average T_c . "Reset 1" and "Reset 2" maps, labeled in the top right panels, highlight the difference between ML3-W(TH) and ML4-W(TH) concerning TH0. A similar analysis using ML1(TH) as a reference gives the same results as expected.

Memory maps at different TH

After gathering all the insights on memory accumulation maps at TH = 68 °C, we conducted the RRM protocol at various turning points (Fig. 5.9). By varying TH in the ramp reversal protocol, we examined its effects on memory accumulation, intensity change amplitude, and time constant. Fitting the average intensity at each turning point revealed that the amplitude differences behaved as expected: at TH = 70 °C, near the metallic phase, there was a decrease in intensity; at TH = 67 °C, the amplitude was higher; and the highest amplitudes were observed at TH = 68 °C and TH = 69 °C. The time constant peaked at TH = 69 °C, though with considerable error bars. Future work could involve applying these temperature protocols for n > 12 to determine if the curve saturates or diverges, which would indicate proximity to criticality. Optimal conditions for application include a fast response and increased amplitude, ideally achieved at temperatures around 68 °C and 69 °C, as shown in graph 5.10.

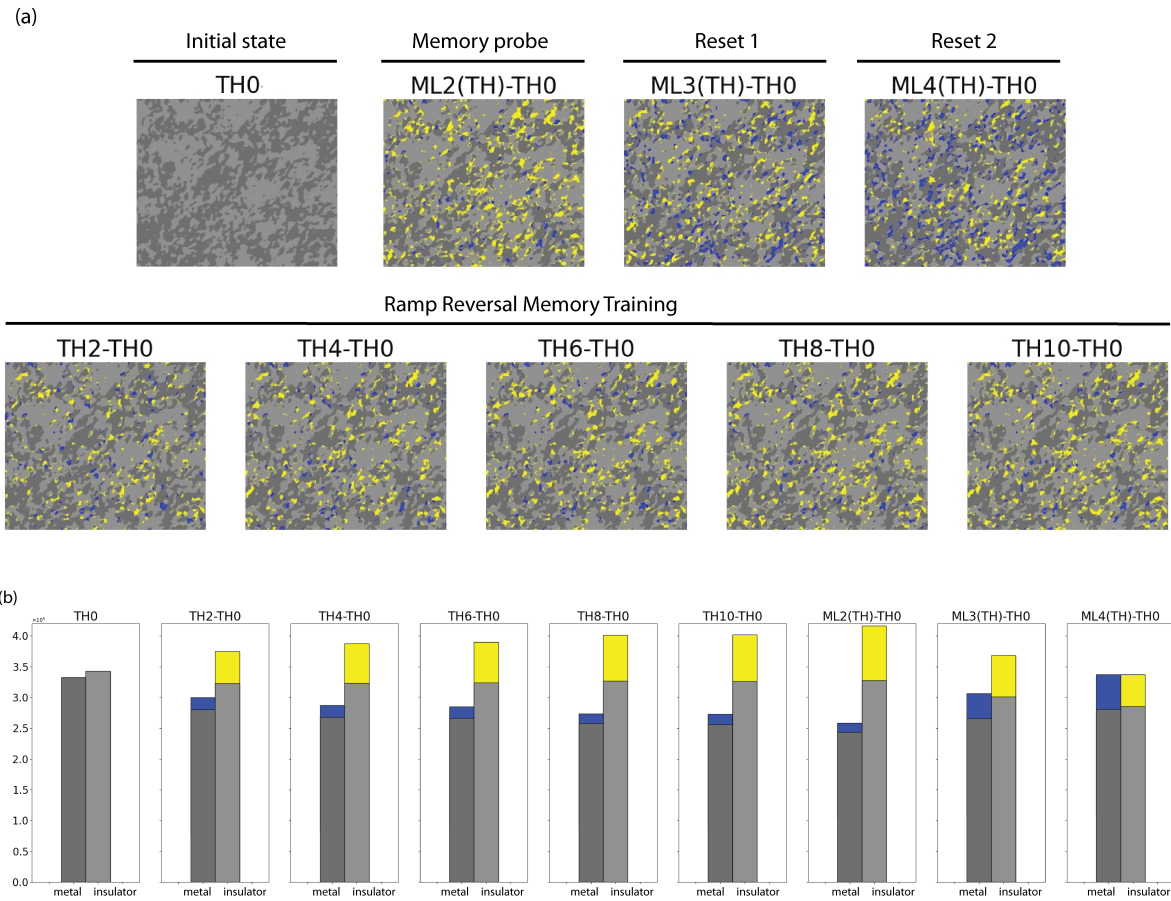


Figure 5.8 – Memory maps: (a) Experimental evolution of the spatial map of metal and insulator domains upon training with successive temperature subloops. Top left panel: Metal and insulator patches right before the first subloop begins, at TH0. Metallic patches are colored dark gray, and insulating patches are colored light gray. Image is $28\mu m$ high. (b) Bottom panels show the corresponding histograms during training and reset.

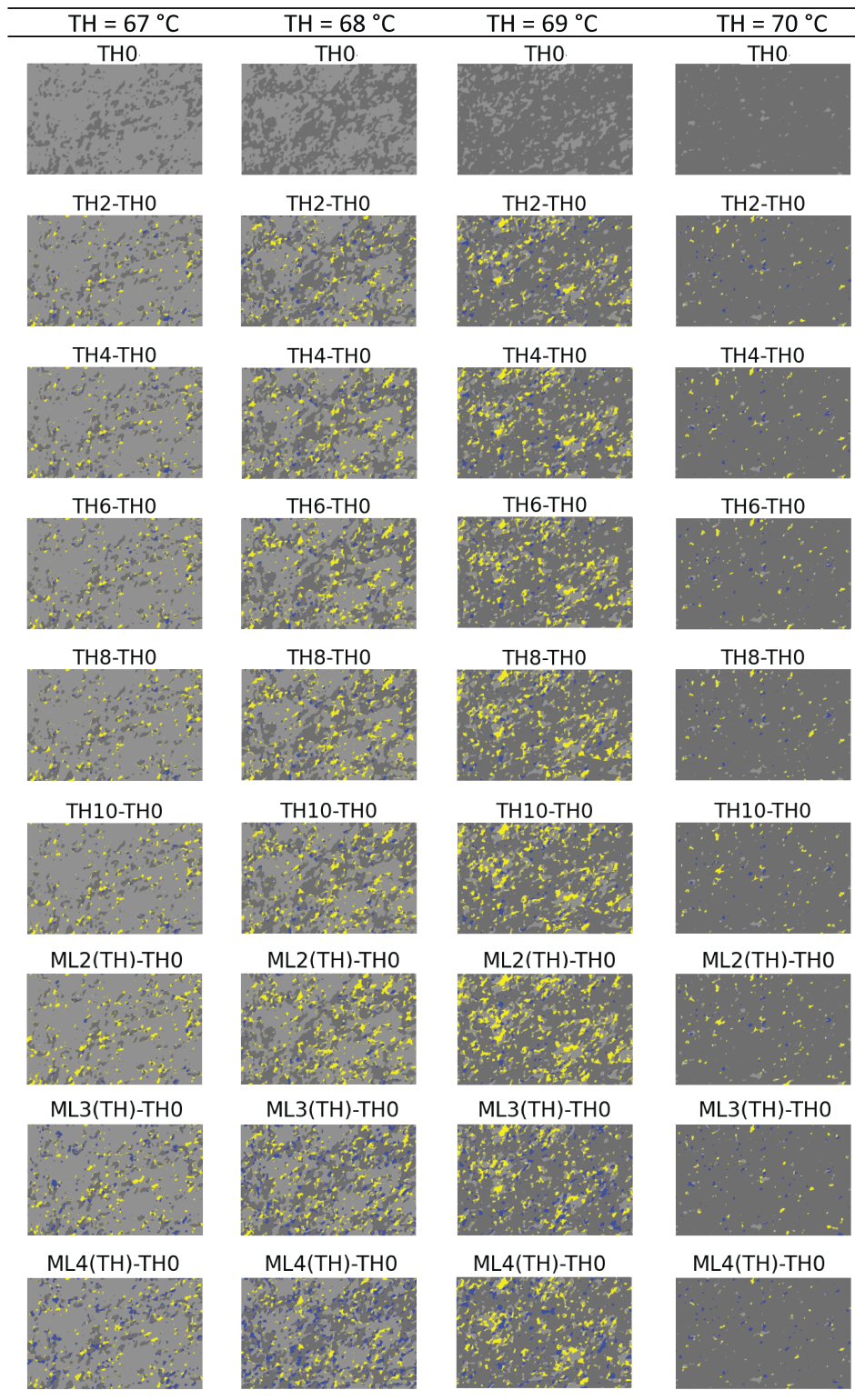


Figure 5.9 – Memory maps as shown in Fig.5.8 at different TH. VO_2 area is $33.6 \mu\text{m} \times 28 \mu\text{m}$ (900 pixels \times 750 pixels).

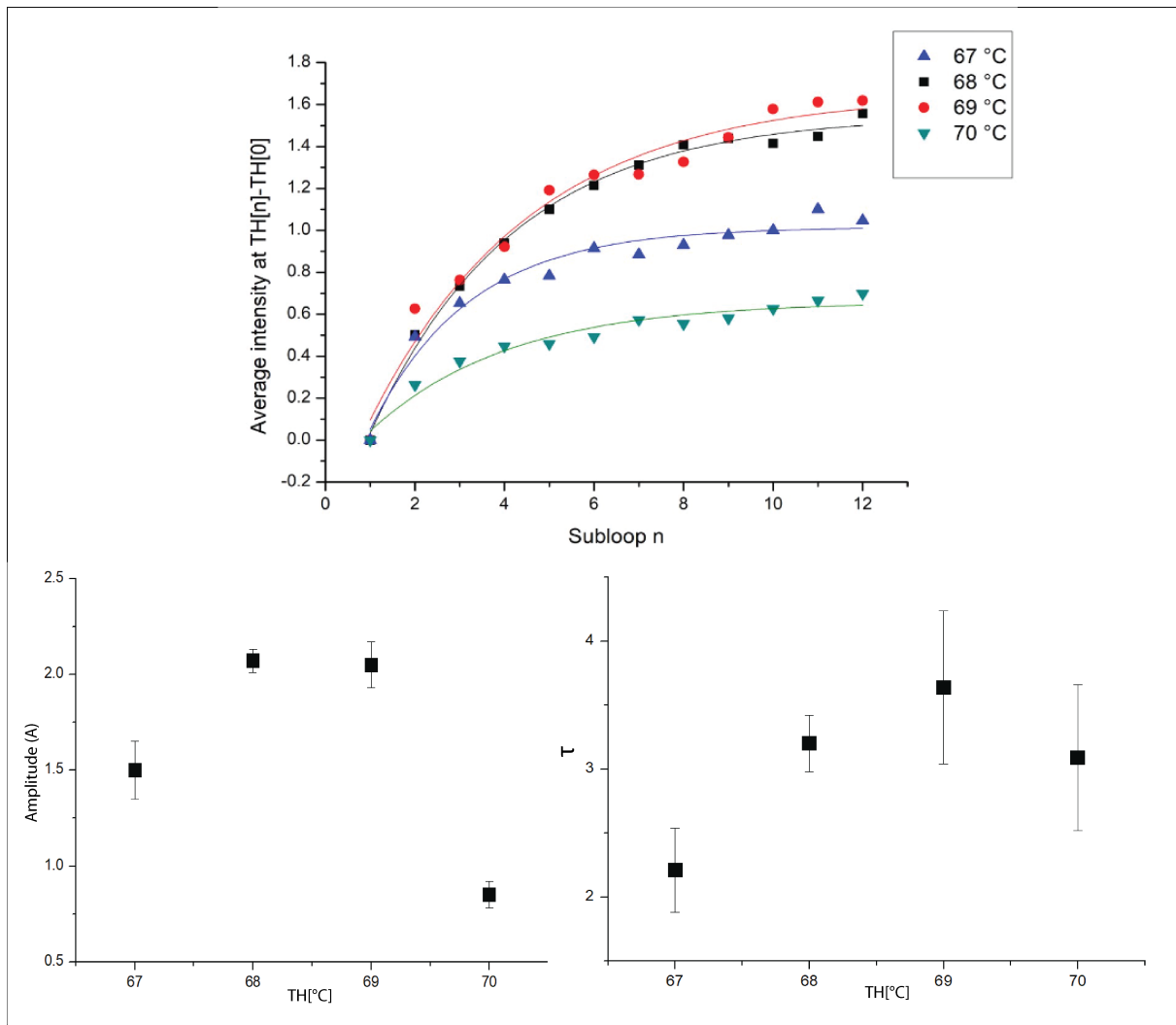


Figure 5.10 – Exponential fit for all TH. There is a peak in the time constant for $TH = 69^{\circ}C$ while the amplitude peaks around 68 - 69 °C, however the changes between these two temperatures are within error bars.

To explain this memory effect in VO₂, Vardi et al. proposed a scar model that suggests the formation of "scars" at metal-insulator boundaries at each TH. These scars are static, quasi-1D deformations in the material's lattice structure that have a higher local critical temperature (T_c) than the surrounding material, meaning they require a higher temperature to change phase. The scar model explains the memory effect observed in temperature-driven IMT in certain materials. As the material is heated, metallic domains appear within the insulating material and grow. When the temperature is reversed and the material is cooled, these metallic domains shrink, and insulating regions grow back. This transition occurs through phase coexistence, near criticality, where both metallic and insulating phases exist simultaneously in different regions of the material.

When the material is reheated after cooling, the scars at the phase boundaries prevent the original metallic regions from easily growing past them. Instead, new metallic domains nucleate and grow, forming new phase boundaries. As the temperature is cycled, more scars develop, reinforcing the memory effect. However, if the material is heated to a sufficiently high temperature, the metallic domains can overcome the scars, "healing" them and erasing the memory. Upon cooling from this high temperature, new scars form corresponding to the new maximum temperature reached.

However, comparing the model with our accumulated memory maps reveals significant distinctions:

(i) Insulating patches around metallic domains do not necessarily form closed loops, indicating the repeated advancement of metallic puddles to the same spots in successive subloops. (ii) Yellow patches, signifying insulating regions, extend beyond domain boundaries, forming large 2D shapes rather than localized 1D lines. (iii) Memory accumulation is not confined to metal-insulator boundaries but extends deep within insulating domains. (iv) Contrary to the scar model's prediction of solely increased local T_c , our memory maps depict regions with both higher (brighter yellow and red), and lower (deeper blue) T_c , as evident in ML2-W compared to ML3-W.

These observations suggest a more intricate mechanism underlying the ramp reversal memory effect in VO₂ than initially proposed by the scar model.

4 Explaining RRM with a minimal model of point defect motion

The spatially resolved optical microscopy maps in this study challenge the explanation of the scar model, which primarily addresses macroscopic resistivity curves. While the scar model offers a plausible macroscopic explanation, it falls short of explaining the accumulation of memory deep within metallic and insulating patches, as well as the occurrence of lowered T_c in certain regions.

In response to this challenges, Carlson's group propose a model based on the diffusion of point defects in the metal-insulator phase separation regime. The results of the theoretical model are published along the experimental results in this work. This model aims to account for the ramp reversal effects observed both macroscopically and microscopically. They employ the diffusion-segregation equation to describe defect motion in the presence of phase segregation

into metal and insulator domains, based on Equation 9 of reference [184], where x is the spatial coordinate, ρ and ρ_{eq} are the actual and thermal equilibrium concentrations at x , the later as a step function convolved with a gaussian kernel with $\xi = 5$, and D is the point defect diffusivity.

$$\frac{\partial \rho}{\partial t} = \frac{\partial}{\partial x} \left[D(x) \left(\frac{\partial \rho}{\partial x} - \frac{\rho}{\rho_{eq}} \frac{\partial \rho_{eq}}{\partial x} \right) \right] \quad (5.2)$$

This model is initialized using the T_c map obtained experimentally from the warming branch of the first major loop (ML1-W) of this work. The density of defects at the beginning of ML1-W is adjusted using the gradient descent method to ensure consistency with experimental conditions. As the model progresses through subsequent simulated warming - cooling cycles, it undergoes the same process as observed in our experiment, starting from identical initial conditions.

According to the assumptions made, defects accumulate in the metal during the ramp reversal process, while being depleted from the insulator whenever phase segregation of metal and insulator domains occurs. Physically this could arise from the fact that rutile unit cells expands compare to monoclinic and creates more strain. Adding point defects preferentially in this phase could help relieve this strain. Moreover, as metal clusters diminish while the temperature decreases, they carry defects along with them. This mechanism of purging defects from the rest of the sample resembles the floating zone technique used in semiconductor purification. Consequently, through successive iterations of the ramp reversal protocol, defects migrate from their original locations in the insulator patches at TH0 toward the regions of lowest T_c in the sample. Since defects typically reduce transition temperatures, this relocation of defects out of the insulating regions and into the metallic regions leads to an overall increase in transition temperature in the cleaner regions of the sample (the insulator) and a decrease in regions with higher defect concentration (the metal). This results in transition temperature maps exhibiting greater ruggedness, as depicted in the ML2-W panel of Fig. 5.4. Instead of undergoing abrupt changes, the equilibrium concentration of these mobile defects must vary smoothly at a metal-insulator boundary.

The equilibrium solution to the diffusion-segregation equation reveals the spatial dependence of defect distribution, crucial for understanding the observed phenomena. However, while theory predicts that regions of low T_c should decrease further during the ramp reversal protocol due to defect accumulation, experimental observations deviate from this prediction(Fig. 5.11). Several factors may contribute to this discrepancy, including non-linear mappings between T_c and defect density changes, annealing effects, and limitations in defect mobility.

It is worth noting that the proposed model offers new insights for future experiments, including those involving local probes such as STM and SNOM, as well as investigations into the effects of film/substrate strain, film thickness, and temperature ramp time on RRM. While the optical experiments provide indirect evidence of defect movements, further experiments are needed to validate and refine the proposed model. These future experiments will aid in refining existing models and further elucidating the underlying mechanisms of ramp reversal memory.

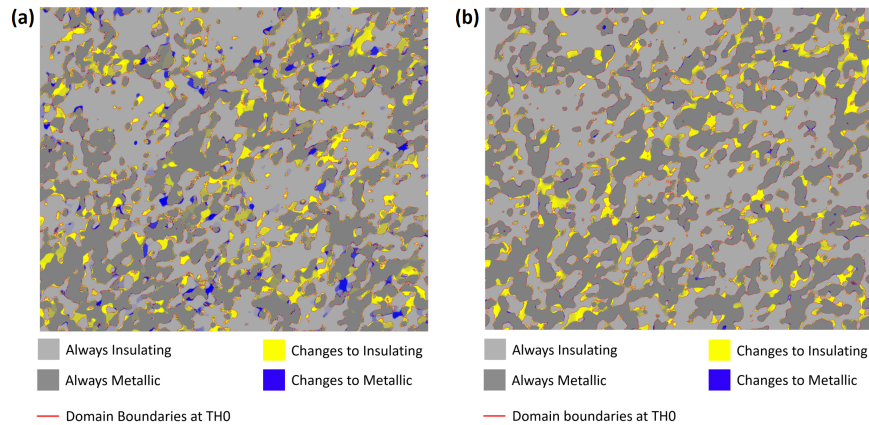


Figure 5.11 – Accumulated memory maps: (a) Experimental and (b) simulated averaged metal and insulator domains at the end of each subloop. The images are a direct average over 10 subloops of the TH_n-TH₀ images. Dark gray denotes regions that are metallic at TH; light gray denotes regions that are insulating at TH. Yellow regions are places where the insulator advanced as compared to TH₀. Blue regions are places where the metal advanced as compared to TH₀. Light yellow regions are typically regions that became insulating only at the end of the 10 subloops. Bright yellow regions however are regions that became insulating at the beginning of the subloops. Red contours mark the original metal-insulator boundaries at TH₀, before the subloops begin. Maps size is $33.6 \mu\text{m} \times 28 \mu\text{m}$.

5 Main achievements

In this chapter, we present the first optical imaging of ramp reversal memory in VO₂. These experiments offer a detailed insight into the spatial distribution of metal and insulator clusters and their evolution during thermal subloop training. Our findings reveal a progression of clusters from one subloop to the next, culminating in a more rugged transition temperature map after applying the RRM protocol. This suggests that memory accumulation extends beyond cluster boundaries at the transition temperature (TH), permeating deep into both metal and insulator patches across the sample.

Chapter 6

Using Deep Learning for pattern recognition in VO₂

The study of materials science has long relied on traditional experimental and theoretical approaches to understand the underlying physics and to identify patterns that govern material behavior. However, machine learning ML capabilities have changed this field, providing powerful tools for data-driven insights and predictive modeling. Now, we have more data coming from surface probes that have elucidated pattern formation in quantum materials across several length scales.

ML has been effectively used for pattern recognition, which involves the automatic discovery of regularities in data and subsequent action based on these patterns. For instance, ML can classify images into categories based on identified patterns, allowing us to extract important features and gain a better understanding of the underlying physics [185]. ML methods require large amounts of data to train neural networks to predict and generalize with high performance. The increasing data from surface probes can be exploited for this purpose [186].

There has been tremendous growth recently in the application of ML methods to condensed matter physics [187, 188, 189, 190]. ML is being applied to various problems, including disordered and glassy systems [191], quantum many-body problems [192, 193], quantum transport [194], and big data in materials science [195]. ML also benefits from physics, an area known as physics-inspired ML theory [188]. Applied to experimental data, ML has been used to detect the phase of matter a physical system is in and to aid in the experimental detection of the glass transition temperature [196]. Other common uses of ML for experimental data include extracting material parameters from experiments or using ML to replace lengthy and time-consuming fitting procedures [197, 198].

In the context of phase transitions, ML has been used to identify the phase of matter in theoretical configurations and to determine the transition temperature of those configurations,

typically assuming a specific Hamiltonian [189, 199]. However, the critical region, characterized by domains exhibiting power-law structures over multiple length scales, has received relatively little focus.

To address this gap, we developed a method that utilizes the rich spatial correlations available in near-critical configurations to **detect which Hamiltonian should be used to describe a physical system**, applying the method to experimentally derived data. Convolutional neural networks (CNNs), which are heavily used in image classification, are key in our model.

CNNs offer several advantages for this task. They are highly effective in recognizing patterns in images due to their ability to capture spatial hierarchies in data through convolutional layers. This makes them particularly well-suited for analyzing the intricate patterns formed by electronic domains in materials like VO₂. Additionally, CNNs can handle large amounts of data efficiently, making them ideal for processing the extensive datasets.

ML offers new theoretical frameworks for understanding why patterns form in strongly correlated materials, as most traditional theoretical tools are designed for understanding and describing homogeneous electronic states. Other method is cluster analysis techniques for interpreting these images, which have already uncovered universal behavior among disparate quantum materials [139, 200]. However, these methods are limited to systems near criticality and for sufficiently large fields of view. Powerful image recognition methods from ML hold the potential to complement and extend these analyses into new regimes.

This thesis chapter explores the application of ML techniques to uncover the fundamental physics and recognize patterns in materials, with a specific focus on VO₂. In particular, we are going to study images coming from Scanning Near-field Optical Microscopy **SNOM** and our optical characterization set-up. We present a deep learning (DL) classifier for pattern recognition using a CNN in spatial configurations from several different Hamiltonians. We test the DL classifier on experimental image data of VO₂ obtained via SNOM we compare the results with the well-established cluster network analysis, and then apply it to new optical microscope images of VO₂, showing that using only simulated data for training, we have developed a robust deep learning classification model capable of identifying the Hamiltonian driving pattern formation from experimental surface probe images.

1 Hamiltonian models that could describe pattern formation

We present three different kind of Hamiltonians that might explain the multiscale textures observed during the metal-insulator transition in VO₂. The domain configurations derived from these Hamiltonians will help train the deep learning model to identify the physics behind the pattern formation in this material. The simulations based on the following models were per-

formed by collaborators in Prof. Carlson's group at Purdue University. We focus on models near a second order phase transition, because the multiscale behavior inherent to criticality is capable of driving the multiscale pattern formation often seen in spatially resolved experiments on quantum materials.

Clean Ising model

First, we consider a simple interacting Hamiltonian. The Ising model is a mathematical model used in statistical mechanics that is commonly used to describe ferromagnetism in materials. It consists of discrete variables called "spins" that can be in one of two states: up or down. In the Ising model, each lattice site (a point on the grid) can be in one of two states, similar to how a material can have regions that are either metallic or insulating. The interaction between neighboring spins (or domains) determines the overall properties of the system. If a metallic domain is surrounded by other metallic domains, it tends to stay metallic, similar to how a spin-up prefers to align with neighboring spin-ups. In our case, the grid is composed by the pixels in one image.

We assume that the interaction energy between neighboring domains is lower when the domains are alike rather than different. Imagine a checkerboard where each square can be either black (spin down) or white (spin up). The state of each square depends on its neighbors. If a square is white, it prefers its neighbors to be white as well, similar to how metallic domains prefer to be near other metallic domains. This tendency for neighboring domains to be similar is modeled using a nearest-neighbor Ising Hamiltonian:

$$H = -J \sum_{\langle i,j \rangle} \sigma_i \sigma_j - \sum_i h \sigma_i \quad (6.1)$$

where $\sigma_i = \pm 1$ is a two-state local order parameter, representing metal (e.g., $\sigma = 1$) and insulator (e.g., $\sigma = -1$) domains. The first term in the equation accounts for the energy due to the interaction between neighboring domains. J is the coupling constant representing the strength of the interaction between neighboring domains. The second term accounts for the energy due to the interaction of each domain with an external magnetic field.

This model is mapped to the temperature-driven IMT in VO₂, assuming that a temperature change in experiments corresponds to a combination of temperature and field changes in the model.

The simulations have configurations near the critical point, as this is where the Hamiltonian can create structures across multiple length scales. Using Monte Carlo simulations, they generate typical multiscale patterns of insulator and metal domains that arise from the clean Ising Hamiltonian. Complex domain configurations appear near the critical points of this model.

Simulation Methods:

Monte Carlo Updates: The simulation uses Monte Carlo methods to update the state of the system. Specifically, it uses a combination of two types of updates:

- Parallel Checkerboard Metropolis Update: This method divides the lattice (a grid representing the system) into a checkerboard pattern and updates the spins (magnetic moments of particles) in parallel, alternating between the two colors of the checkerboard.
- Wolff Algorithm: This is another type of Monte Carlo update that is efficient for simulating the Ising model, especially near critical points. It works by flipping clusters of spins instead of individual spins, which helps reduce autocorrelation times.

Thermalization:

The system is first thermalized, meaning it is allowed to reach thermal equilibrium. This is done by performing 100,000 steps of the parallel checkerboard Metropolis updates interleaved with 10,000 Wolff updates.

Saving Spin Configurations:

After thermalization, spin configurations (the arrangement of spins in the lattice) are saved periodically. Specifically, configurations are saved after performing 10 parallel checkerboard Metropolis updates followed by 10 Wolff updates.

System Size and Boundary Conditions:

The simulated system is a 3D lattice of size $100 \times 100 \times 100$

Boundary Conditions:

- Open Boundary Conditions (OBC) in the z-direction: Spins at the boundaries in the z-direction are not influenced by spins outside the system.
- Periodic Boundary Conditions (PBC) in the x and y directions: The lattice is treated as if it wraps around on itself in the x and y directions, creating a continuous loop.

Saving 2D Spin Configurations:

After thermalization, 2D slices of the 3D lattice are saved for analysis. These include:

- Two open surfaces: The outermost layers of the lattice in the z-direction.

- Three parallel 2D slices from the interior: These slices are taken from within the lattice and are spaced equally to minimize correlations between them.

Additionally, 2D configurations are saved from the orthogonal directions:

- Four configurations perpendicular to the x-direction: Equally spaced slices in the y-z plane.
- Four configurations perpendicular to the y-direction: Equally spaced slices in the x-z plane.

Figures 6.1(a) - (d) show some configurations near the critical temperature T_c^{2D} on a 100×100 lattice, with periodic boundary conditions. Figures 6.1(e)-(h) show some representative configurations near T_c^{3D} on a $100 \times 100 \times 100$ lattice.

Random Field Ising model

The Random Field Ising Model (RFIM) is a variation of the Clean Ising model. In the standard Ising model, each spin can be in one of two states (up or down), and spins interact with their nearest neighbors. The RFIM introduces a random external field, adding disorder to the system. This random field can cause each spin to experience a different local environment, leading to more complex behavior. Besides interaction energy between domains, material disorder also influences the shapes of metal and insulator domains. Since disorder can make certain regions more favorable to being an insulator and others more favorable to being metal, we use a random-field Ising model (RFIM) to simulate these effects:

$$H = -J \sum_{\langle i,j \rangle} \sigma_i \sigma_j - \sum_i (h_i + h) \sigma_i \quad (6.2)$$

The first term is the clean Ising model (Eq. 6.1.) In the second term, the uniform field h and the local random fields h_i interact directly with the local order parameter. The random fields h_i are chosen from a Gaussian distribution with a width R , where the probability of h_i is $P(h_i) = \exp(-h_i^2/(2R^2))\sqrt{2\pi R^2}$. In VO₂, the IMT is temperature-driven. In the model, this transition appears as a combination of temperature and uniform field h . When both temperature and disorder are non-zero, the random field dominates the behavior near the phase transition. This means that in the renormalization-group sense, the temperature becomes irrelevant, while the random field remains relevant over a broad range. This means that the random field's effects become more pronounced and critical as the system is viewed at larger scales. The random field strongly influences the system's macroscopic behavior near the transition. To understand the patterns of metal and insulator domains, the model is studied at zero temperature by varying the uniform field h . At zero temperature, the model undergoes a phase transition at a random field strength of $R_c \approx 2.27J$ in an infinite three-dimensional system (RF-3D). In two dimensions (RF-2D), the critical disorder strength approaches zero in the infinite size limit, although for finite systems, R_c is non-zero. For our field of view (FOV), $R_c \approx J$ for RF-2D.

Near the critical point of the random field model, as the uniform field is varied, intricate patterns develop over multiple length scales near the coercive field strength, where the metal/insulator domain fraction changes rapidly with respect to the uniform field h . Figures 6.1(i)-(l) show representative configurations of RF-2D on a 100×100 lattice. Figures 6.1(m)-(p) show configurations on the surface of a $100 \times 100 \times 100$ lattice near the 3D critical disorder strength R_c^{3D} .

Percolation model

In some cases, domains may not interact with each other as described in the above Hamiltonians. Instead, each domain could act independently. In the corresponding uncorrelated percolation model, a site is labeled as "metallic" with a probability p ; otherwise, it is labeled as "insulating." When $p \neq 0.5$, this process is like flipping a biased coin, where p is the probability of getting heads.

This model also exhibits a second-order phase transition based on the value of p , showing structure across multiple length scales near its critical point. The critical percolation threshold, p_c , is identified by the presence of a percolating cluster that spans the entire system, touching both sides.

In a two-dimensional system on an infinite square lattice, this threshold occurs at $p_c^{2D} \approx 0.59$. In a three-dimensional system on an infinite cubic lattice, it occurs at $p_c^{3D} \approx 0.31$. Figure 6.1(s) shows a percolation configuration of size 100×100 at $p_c^{2D} = 0.59$. Figure 6.1(q) shows a percolation configuration of size $100 \times 100 \times 100$ at $p_c^{3D} = 0.31$.

To improve the deep learning (DL) model's ability to tell apart configurations near a critical point from those that aren't, we also create additional training images using a method called uncorrelated percolation, but away from critical points (Fig. 6.1(q) and Fig. 6.1(t).) To avoid the complex, fractal-like patterns that appear near critical points, we generate these images within specific ranges of $p = 0.02 - 0.2; 0.48 - 0.52; 0.8 - 0.98$.

- The first range (0.02-0.2) produces images that are mostly black.
- The second range (0.48-0.52) produces images that are "white noise" (such as in Fig. 6.1(r)).
- The third (0.8-0.98) range produces images that are mostly all white (like those in Fig. 6.1(t).)

By using these different ranges, we ensure that the model learns to identify and distinguish between various types of configurations, not just those near the critical point.

Other than P, the models each have a second order phase transition, at which the spin configurations display power law behavior, with structure on all length scales up to the correlation length, which diverges at the critical point.

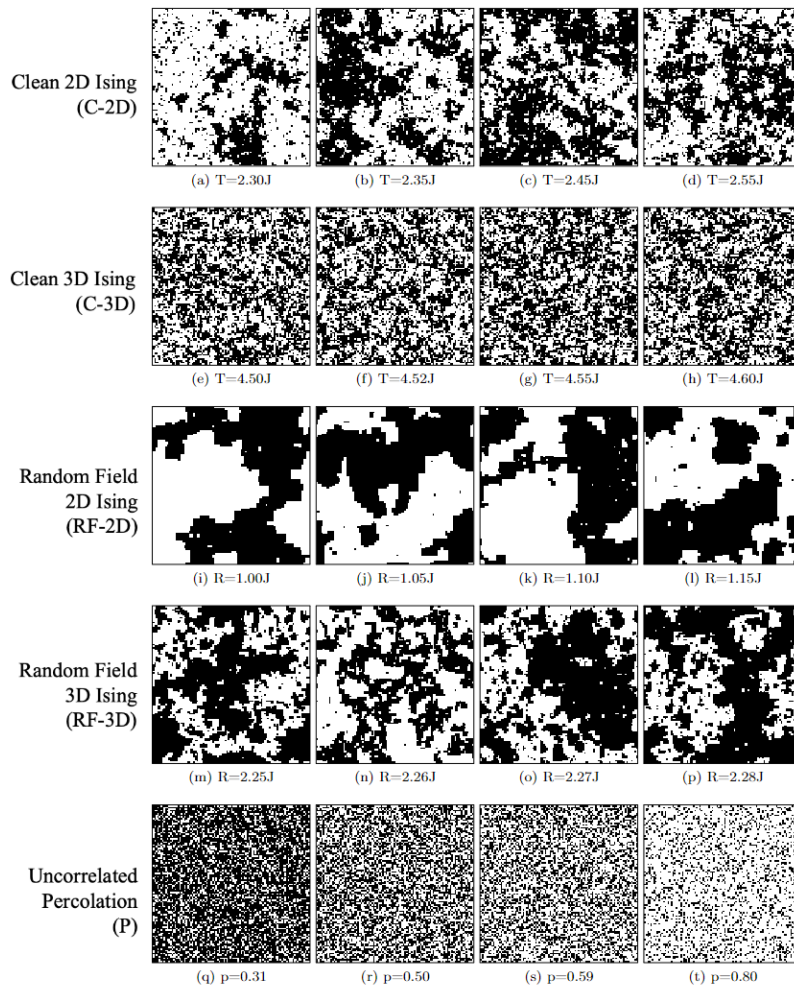


Figure 6.1 – Typical critical configurations generated from simulations of clean and random field Ising models and percolation models. Each simulation image is 100×100 pixels.

2 Synthetic images dataset

The DL model needs to learn the features of the pattern forms by each one of the models described in the previous section. For this aim, enough example images have to be fed for the training stage of the model. In total, a set of 64,000 synthetic images was generated to train the CNN. This included 8,000 images for each model near its transition, except for the percolation model, which produced 16,000 images due to variations away from the 2D and 3D critical percolation strengths.

To increase the diversity of training sets, data augmentation is often employed. This prevents overfitting and enhances model generalization and performance. Common transformations for data augmentation include geometric transformations and noise injections.

In our system, the entire phase space associated with typical configurations generated by the models exhibits certain symmetries. These symmetries can be exploited to generate more configurations and augment the training data. For instance, the clean Ising model satisfies the Z_2 symmetry $\sigma_i \rightarrow -\sigma_i$. Similarly, the RFIM is symmetric under the simultaneous operations $\sigma_i \rightarrow -\sigma_i$ with $h_i \rightarrow -h_i$, and the percolation model is symmetric under the operations $\sigma_i \rightarrow -\sigma_i$ with $p \rightarrow 1 - p$. Additionally, for the square domain configurations we use as training data, the statistical weight of typical configurations in phase space is symmetric under all operations of the dihedral group of the square, D_4 . This symmetry allows us to increase the training set by a factor of 16 for the square-shaped images of domain patterns.

Instead of traditional data augmentation, an alternative method is utilized: symmetry reduction. This method involves reducing the symmetry of each configuration as much as possible before feeding them into the neural network. Symmetry reduction is as effective as data augmentation but significantly reduces the time needed to train the neural network. For symmetry reduction to be effective, all data must undergo this process before being fed into the CNN for both training and validation stages.

The symmetry operations applied to these spin configurations, while preserving the statistical weight of typical configurations in phase space, include:

Ising Z_2 symmetry $\sigma_i \rightarrow -\sigma_i$: If a domain configuration has a majority of spins down, we flip all spins to make it a majority spin-up configuration.

Rotations: The configuration is rotated by 0, $\pi/2$, π , or $3\pi/2$ such that of the four quadrants, quadrant I has the most spins up.

Transpose (reflection about the xy diagonal): If quadrant IV has more spins up than quadrant II, we transpose the configuration to ensure that quadrant II has more spins up than quadrant IV.

This method is described in Fig. 6.2. By applying these symmetry reduction techniques, we effectively prepare the data for the neural network, ensuring both efficiency and consistency in training.

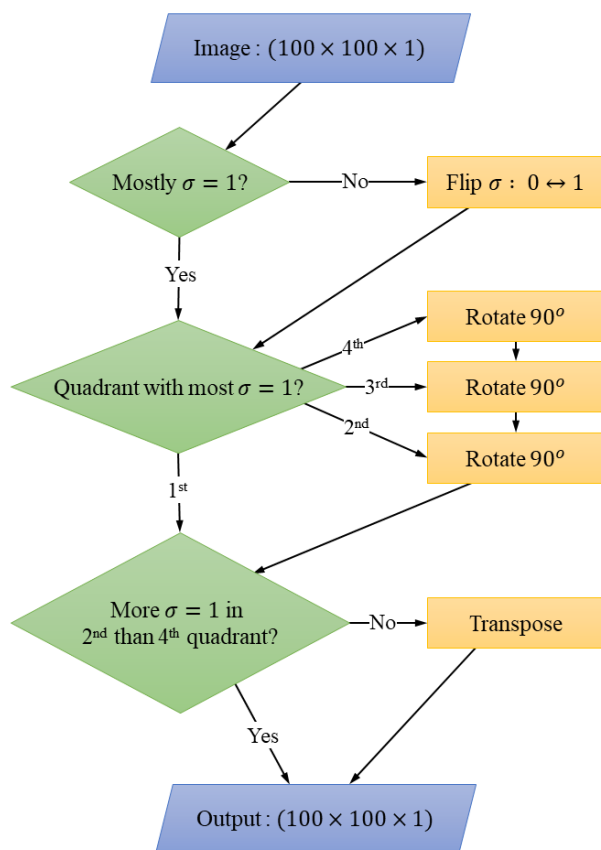


Figure 6.2 – Symmetry reduction method, as described in the text.

3 Model architecture

A CNN was employed to classify binary images into one of the seven Hamiltonians (Fig. 6.3). The code uses TensorFlow as the framework to implement the classifier in Python within a Jupyter notebook. The input is a 100x100 one-channel image, which is fed into the first convolutional layer (Conv2D) with 32 filters and a kernel size of (5, 5). This is followed by a Max Pooling layer of size (2, 2) to reduce the spatial dimensions of the feature maps and prevent overfitting. Another Conv2D layer with 64 filters and another Max Pooling layer follow. The output is then flattened into a 1D layer with 1024 units. After the fully connected layer, a Dropout layer with a rate of 0.5 is added. The final output layer uses a softmax activation function that allows a multiclass classification in one of the seven hamiltonians (C-2D, C-3D, RF-2D, RF-3D, P-2D, P-3D, and P*). The classes are mutually exclusive and with equally importance. The model employs the Adam optimizer and a cross-entropy loss function for parameter adjustment in the CNN.

For the training stage, 80% of the synthetic data for each category was used for training, while the remaining 20% was reserved for model validation. In deep learning, various methods are used to assess the performance and learning of classifiers from the training data. Two key metrics are accuracy, which measures the proportion of correct predictions, and training loss, often referred to as error, which quantifies the difference between predicted and actual outcomes.

We use accuracy as a metric that tells how well the classifier is predicting across all models, by computing the percentage of correct predictions with respect to the total number of predictions. For instance, if an image of the training set is correctly classified as C-2D and it matches the true label then it is accurate. The model has an accuracy of 99.64 % when tested on the training set, and 99.67 % when tested with similar images that has not seen before.

The training error is calculated summing over all images of the training set after each batch. In a similar way, the validation error is calculated after an epoch. An epoch is finished when the training iterates over all images in the training set. We selected training the model for 4 epochs to prevent overfitting. Figure 6.4 shows that the classification errors are less than 0.5 % at this point. Setting the "number of epochs" tells how many times the learning algorithm will process the whole training set and adjust the parameters accordingly.

3.1 Outliers detection method

The softmax output is a probability distribution over the input classes, producing a vector of predicted probabilities for the different models. The probabilities sum to 1, with the highest probability assigned as the label for a given classified image, making the output directly interpretable. The softmax function is defined in Eq. 6.3, where n is the number of models and v_j are the values for the output layer.

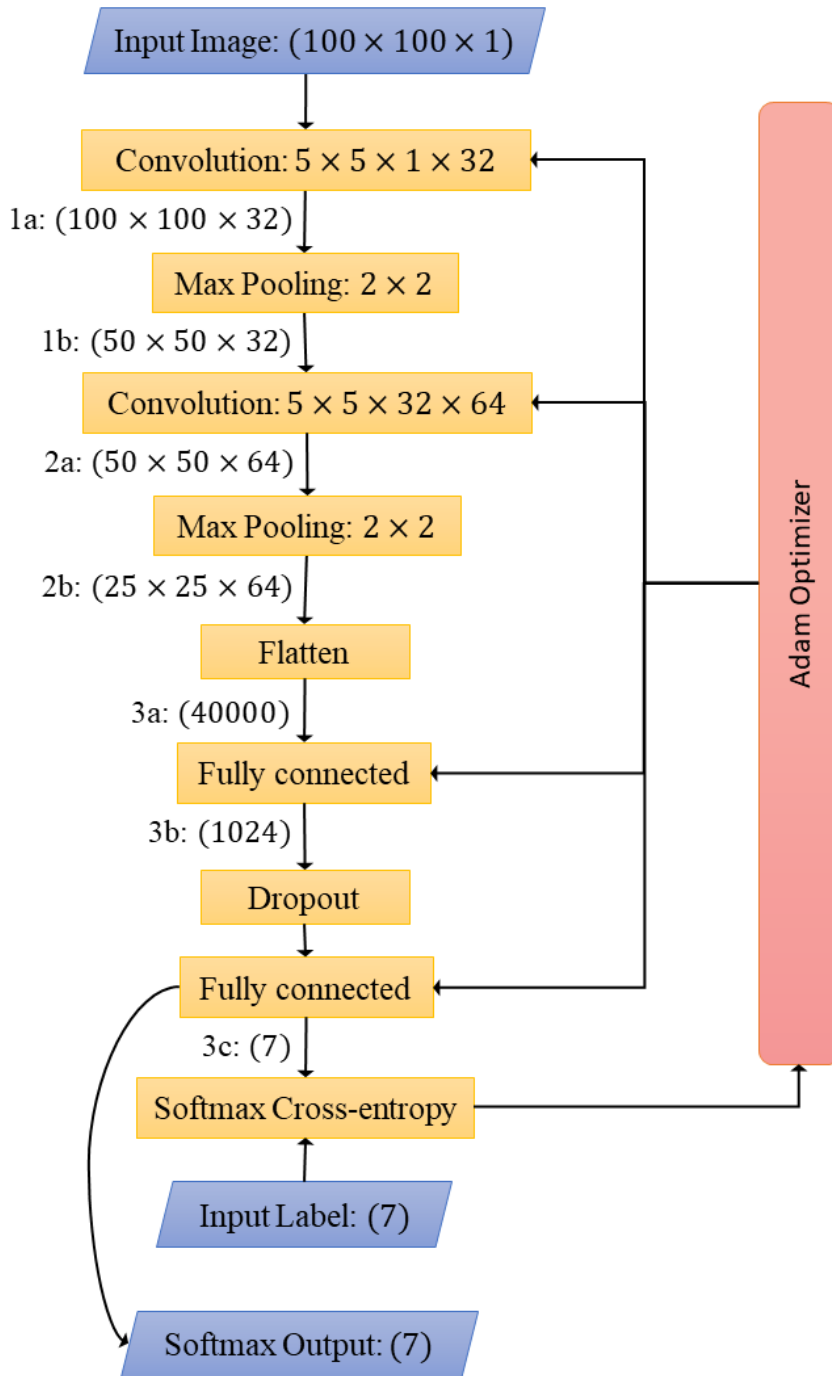


Figure 6.3 – Convolutional Neural Network. The multi-dimensional output 2b is flattened into a one-dimensional array (3a) before it is fed into the fully connected layer. We use the Adam (Adaptive moment estimation) optimization algorithm to train the network. The output label is determined using softmax activation on the output layer.

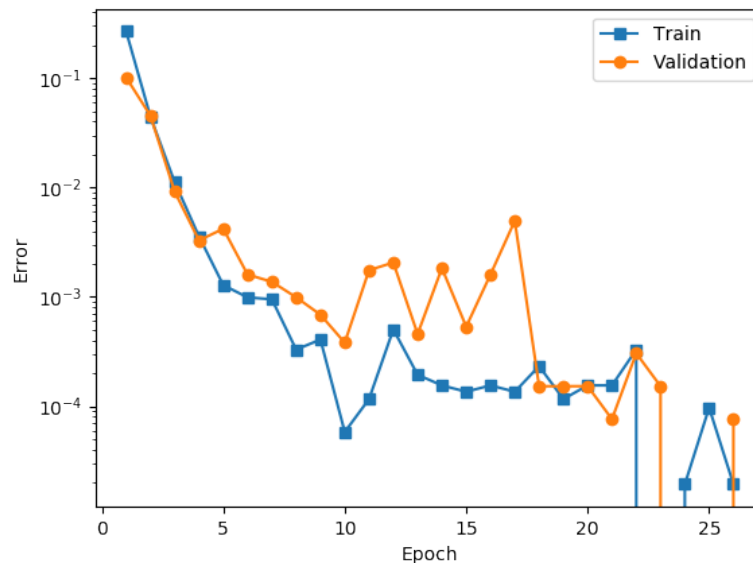


Figure 6.4 – Error in the training and validation set vs. the number of epochs. Epochs correspond to the number of times the training set went through a training process. To prevent overfitting we chose epoch=4 for testing with experimental images. Training/Validation accuracy = 99.64%/99.67%.

$$Y_i^{softmax} = \frac{\exp(v_i)}{\sum_{j=1}^n \exp(v_j)} \quad (6.3)$$

However, there could be cases where none of the models correctly describe the Hamiltonian governing the pattern formation, yet the image is still classified as one of the seven models. This issue is especially relevant when classifying images from experimental acquisitions. To detect outliers, several methods can be employed. One approach is setting a threshold for the probabilities, but since images are taken at different temperatures and the CNN is trained on synthetic data close to criticality, they may contain varying amounts of information. Another strategy involves adversarial networks, which modify the training set and learn to detect suspicious classifications, but this is limited by the amount of presented cases.

In our work, we propose examining the distribution of data points in the hyperspace generated from the training examples, specifically by analyzing the last fully connected layer. Each data point in the graph can be thought as a particle. For two particles to be included in the same group (cluster), they have to be within a specified distance range. We observed that the classes form well-separated clusters (Fig. 6.5). The centroids (center of mass) of each cluster which are data points representing the center of the cluster are calculated by computing the arithmetic mean of data points assigned to the cluster. Since we have seven models, those centroids are seven-dimensional vectors.

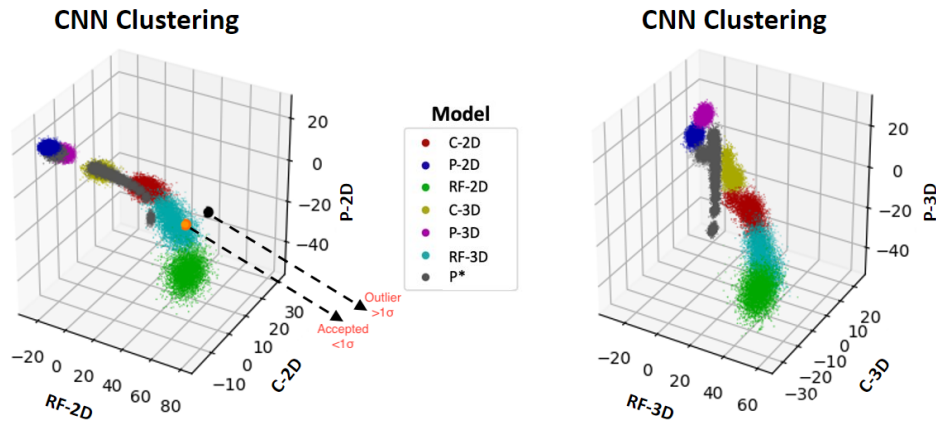


Figure 6.5 – Distribution of values of the output nodes for each class in the last fully connected layer, for all of the training sets. These clusters inhabit a 7-dimensional ‘model’ space. The two representations in the figure are projections of the same 7-dimensional information onto two different 3-dimensional subspaces.

However to be able to visualize the clusters, we plotted them in 3D. Figure 6.5 shows the representation of each cluster in different colors, plotting the values for each data point for the 2D hamiltonians coordinates in one side, and the 3D hamiltonians in the other. An example of classification is as follows: A data point representing a classification is depicted as an orange dot. This orange dot is close to the cluster in cyan corresponding to the RF-3D and the distance from the centroid of this cluster is within 1σ , so we have confidence on this classification. On the other hand, the black dot would be also classified as RF-3D since it is closer to that cluster in comparison with the other models, however, it is located further than 1σ , hence we are not confident on this result since it could be better explained by a model the CNN wasn’t trained on. Thus, we can consider the black dot as an outlier.

4 Vetting the Deep Learning model with experimental data

We first tested the performance of the trained CNN on an experimentally derived dataset, where the Hamiltonian that best describes the pattern formation is already known. The experimental data consists of images taken with SNOM on a thin film of VO₂. Four images at different temperatures were considered for the test, including one near criticality, where phase coexistence between metallic and insulating puddles occurs. The field of view for SNOM images is $4\mu\text{m}$.

Previous studies used cluster network analysis to understand the physics underlying the pattern formation [170]. These studies showed that the patterns are fractal in nature, exhibiting spatial correlation from the pixel size (20 nm) up to the field of view. The quantitative geometric characteristics and avalanche statistics matched those of RF-2D.

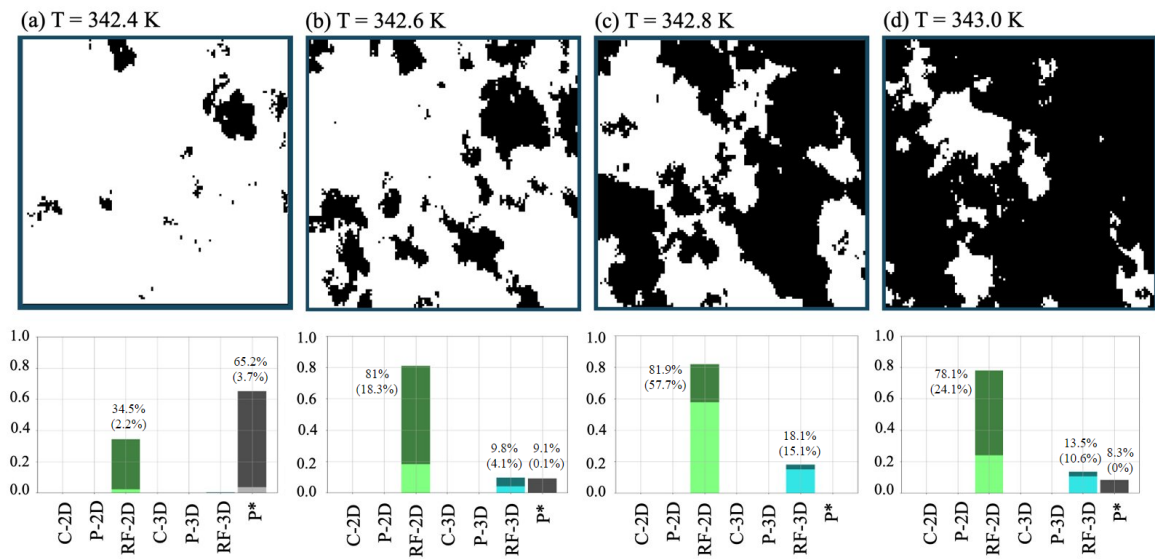


Figure 6.6 – Classification results of our deep learning model applied to SNOM images on a thin film of VO_2 . The top row shows the thresholded data showing insulating (white) and metallic (black) patches. The total percentage of classifications for a particular model are reported in the bar charts of panels (a)-(d). Classification percentages that fall within 1σ of a cluster in the training set are indicated in parentheses. Classifications that fall more than 1σ away from the edge of the corresponding cluster in the training set are colored darker in the bar chart. SNOM images are $4\ \mu\text{m} \times 4\ \mu\text{m}$ (256×256 pixels).

SNOM measurements provide intensity as a continuous variable at each pixel, resulting in single-channel images. Since the CNN input must be a binary image, we thresholded the images, assigning SNOM values of $a < 2.5$ as insulating and $a > 2.5$ as metallic. These values are consistent with previous work showing that the geometric characteristics of the pattern formation are insensitive to threshold changes within about 15% of this value. SNOM images are 256x256 pixels, so to utilize the entire field of view, we computed a sliding window of size 100x100, taking strides of one pixel for a total of 157x157 classifications per image.

Figure 6.6 shows the SNOM images classified by the CNN, along with the percentage of classification indicated by bars below them. At the first temperature, furthest from criticality, there is little pattern formation, resulting in low classification confidence. The highest classification confidence is achieved at $T = 342$ K, with 57.7% of the image classified as RF-2D within one standard deviation and 81.9% when counting all classified values. These results are consistent with previous studies.

We also examined the distribution of data points in hyperspace (Fig. 6.7), visualizing data classified within 1σ in orange and other classified values in black. The orange points are consistently close to the **RF-2D model**, becoming more pronounced as the system approaches criticality.

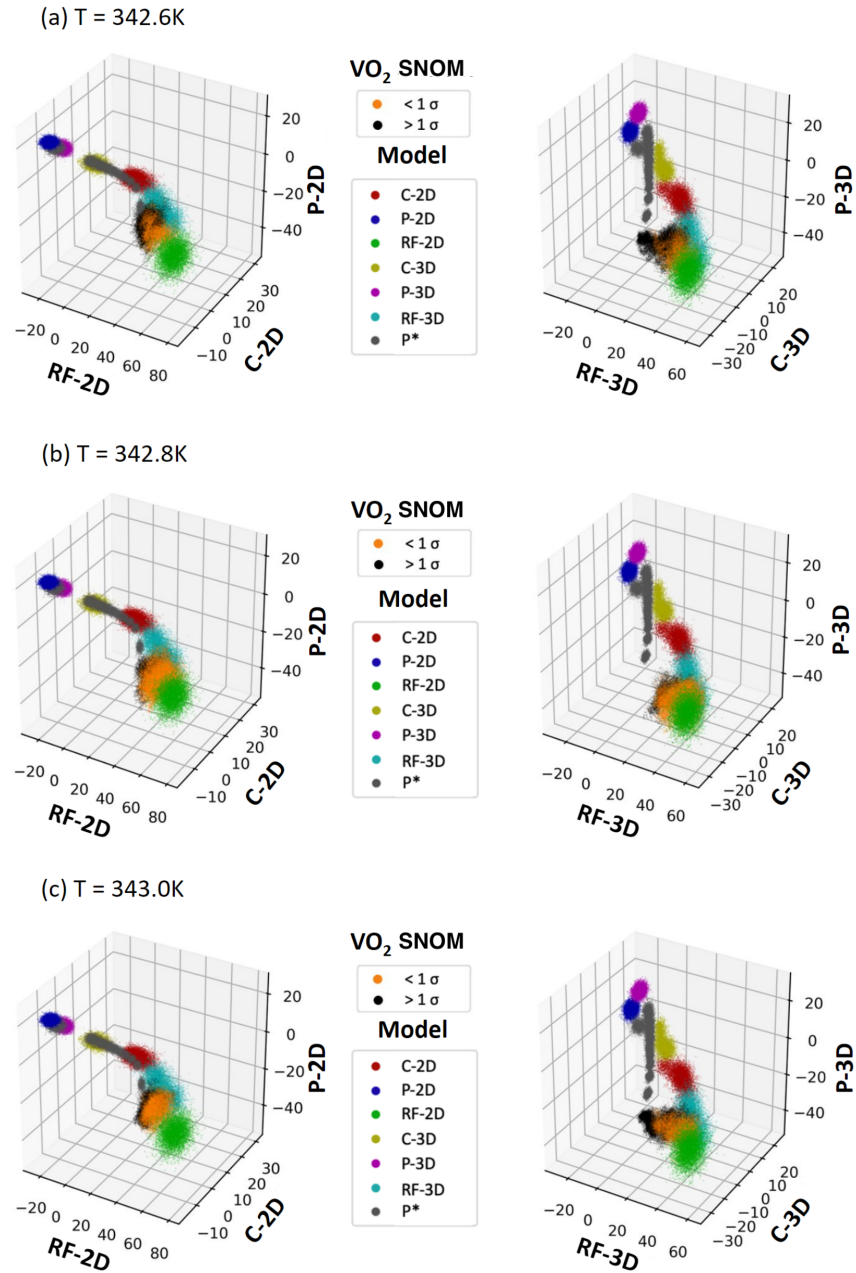


Figure 6.7 – Distribution of values of the output nodes for each class in the last fully connected layer, for the VO₂ SNOM data, superimposed on the distribution for the training sets shown in Fig. 6.5. Results for the VO₂ data that are within one 7-dimensional standard deviation of a training set are indicated by orange dots. Results for the VO₂ data that are farther away are indicated by black dots.

5 Classifying VO₂ images acquired with optical set-up

After verifying the classification of images acquired from a VO₂ thin film with SNOM, we proceeded to test the CNN using images obtained with our experimental optical setup described in Chapter 3. For this purpose, we applied a 3-point convolution to reduce high-frequency noise and thresholded the images using the midpoint of each single pixel time trace. This process resulted in images displaying only metallic and insulating phases. The image size was 760x760 pixels, with a field of view of $28\mu\text{m} \times 28\mu\text{m}$, leading to 661^2 classifications per image.

Figure 6.8 shows the classification results for four images at different temperatures, varying in proximity to criticality. The results mirrored those from SNOM images, but the classification percentage increased to 89.42% within 1σ and 99.98% overall at $T = 341.35$ K, identifying the RF-2D model. The distribution of weights shows the orange cloud of high-confidence points closely aligning with the RF-2D model (Fig. 6.9).

Identifying the Hamiltonian as RF-2D indicates that material disorder and interactions between spatially proximate metallic and insulating sites drive the pattern formation. For this reason, the Preisach model that describes hysteresis in systems as made up of many independent hysteretic elements is not suitable. Random-field critical points exhibit extreme critical slowing down: barriers to equilibration grow as a power law as the system nears criticality, causing the characteristic relaxation time to grow exponentially [201]. This leads to highly nonequilibrium behavior, including hysteresis, glassiness, coarsening, and aging. Moreover, the model has an anomalously large region of critical behavior: a system 85% away from the critical point can still display two decades of scaling [202]. Thus, it is relatively easy within this model to enter a regime that exhibits pattern formation across multiple length scales, including fractal textures.

In Chapter 4, we observed that the distribution of the T_c map is non-symmetric, but the histogram of the difference is symmetric, this could mean that the switching mechanism of some part of the samples is not governed by the RFIM, but by other mechanisms. These differences might be caused by the presence of defects such as grain boundaries.

In the optical setup, we can acquire more images at various temperatures, allowing us to classify the entire range of images during a warming ramp, as shown in Fig. 6.10. The classification percentage increases smoothly as the system approaches criticality, suggesting this could be a valuable new tool for diagnosing proximity to criticality.

Classified images coming from experiments that are close to the metallic and insulating phase do not exhibit pattern formation, so there is less information available to distinguish the underlying model and they are classified as P*. We expect that as the images are taken at temperatures closer to T_c , the detection of the model will peak at that particular temperature. Proximity to criticality is typically discerned through correlation lengths, which are expected to diverge as a power law near the critical temperature, following $\xi \propto 1/|T - T_c|^\nu$.

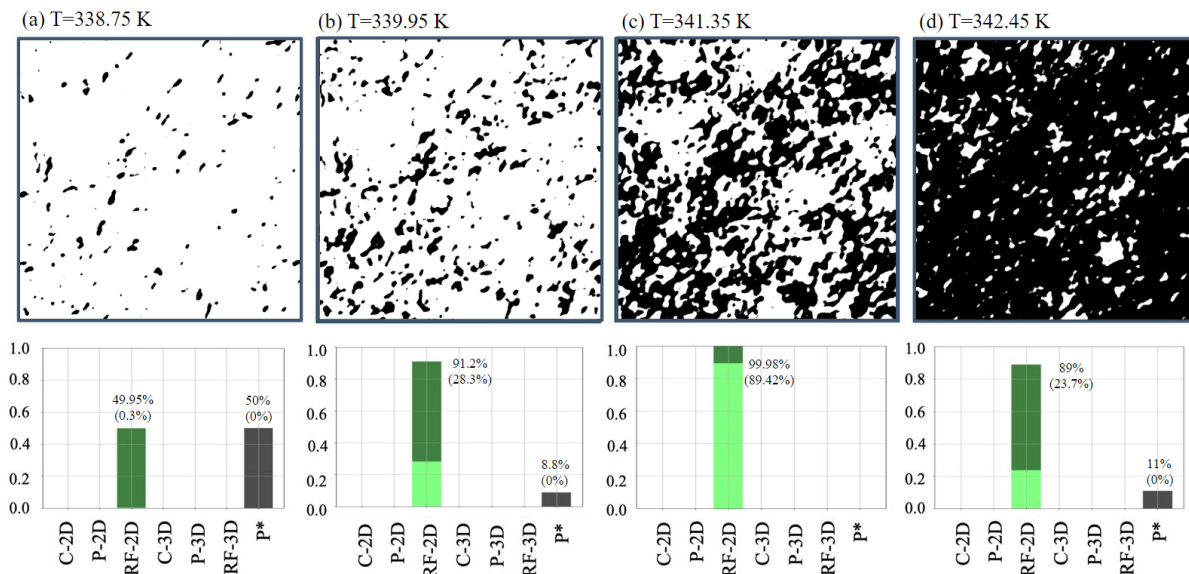


Figure 6.8 – Classification results of our deep learning model applied to new $28 \mu\text{m} \times 28 \mu\text{m}$ optical microscopy images of a VO₂ thin film showing metallic (black) and insulating (white) patches. The total percentage of classifications for a particular model are reported in the bar charts of panels (a)-(e). Classification percentages that fall within 1σ of a cluster in the training set are indicated in parentheses. Classifications that fall more than 1σ away from the edge of the corresponding cluster in the training set are colored darker in the bar chart.

However, the maximum correlation length our CNN can detect is limited by the field of view of the experimental data. The CNN does not return a length scale but shows that the proximity of experimentally derived data's cluster of output values in the last fully connected layer approaches and then retreats from the training set cluster as a function of temperature. This is evidenced by the nonmonotonic behavior of the height of the bright green bars with temperature in Fig. 6.10. This supports our hypothesis that the average distance of the cluster from that of the training set can measure proximity to criticality.

For both experimental datasets, whether from SNOM or optical microscopy, the CNN determined that the pattern of metal and insulator patches was governed by the RF-2D physics. For the SNOM data, this matches the previous identification of the study using the same images in [170]. For the microscope data, it was known prior to the CNN application that a 2D Hamiltonian should drive the pattern formation because the film thickness (100 nm) is comparable to the instrument's lateral resolution. Thus, the spatial correlations measured are firmly in the two-dimensional limit. The CNN's identification of a two-dimensional model, rather than a three-dimensional one, further validates our method.

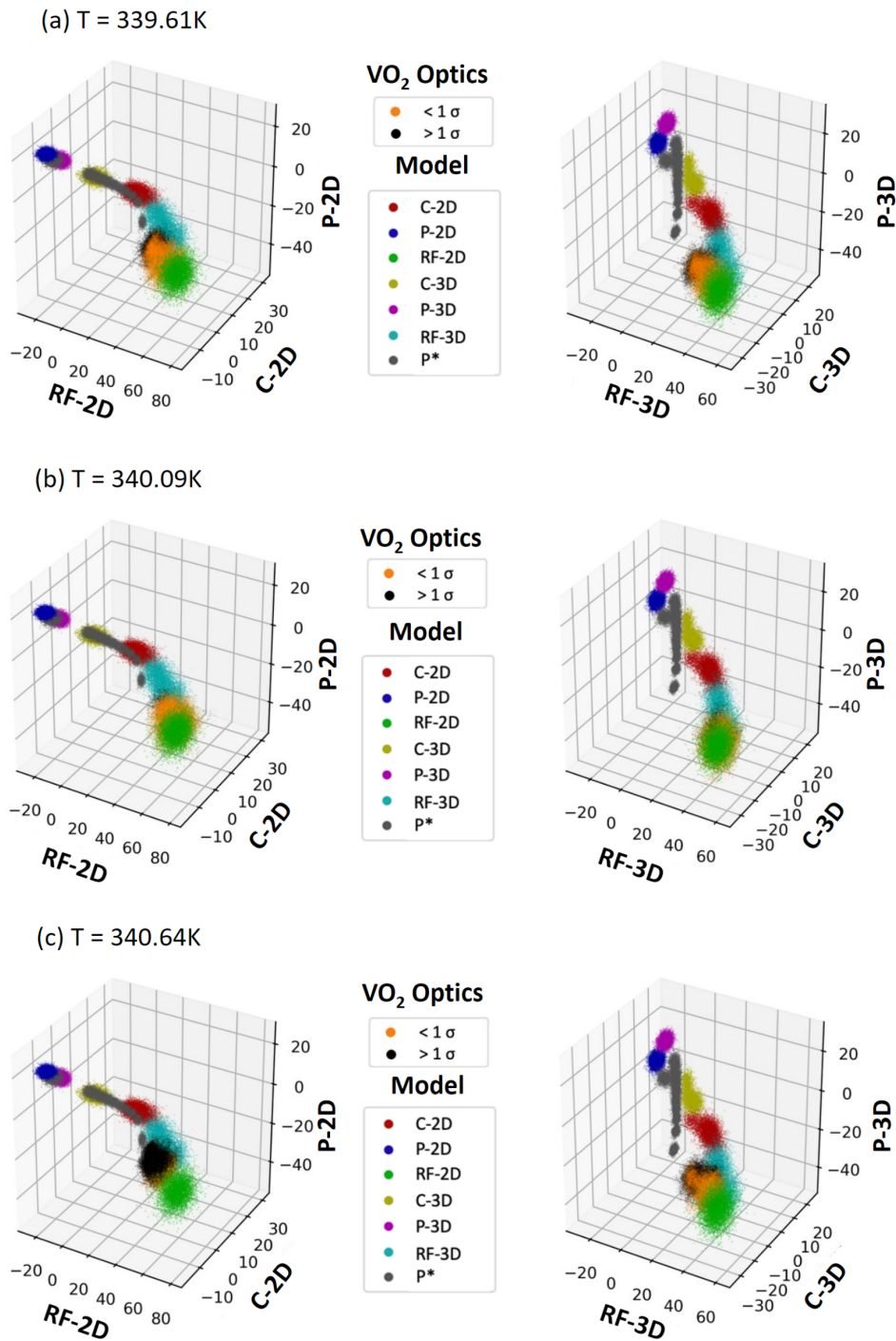


Figure 6.9 – Distribution of relative weights of each class in the last fully connected layer, for the VO₂ optical data (square sample presented in Fig. 6.8), superimposed on the distribution for the training sets shown in Fig. 6.5. Results for the VO₂ data that are within one 7-dimensional standard deviation of a training set are indicated by orange dots. Results for the VO₂ data that are farther away are indicated by black dots.

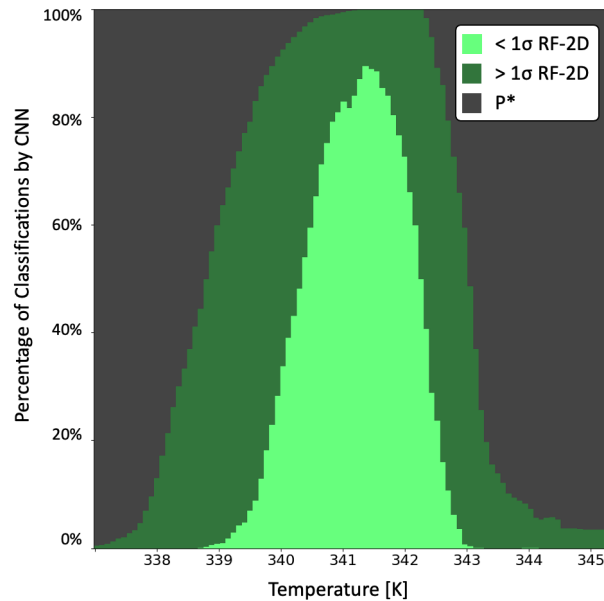


Figure 6.10 – All CNN predictions from optical data during a temperature ramp up of data presented in Fig. 6.8. Darker colors denote classifications that are more than 1 standard deviation from the identified training set.

6 Main achievements

Using binary images, taken at fine temperature steps, we proposed a machine learning-based criterion for diagnosing proximity to criticality, validated by successfully classifying Hamiltonians in SNOM and optical microscopy images of VO_2 thin films, confirming that pattern formation is driven by the two-dimensional random field Ising model (RF-2D) near a critical point.

We have demonstrated that the CNN achieves over 99% accuracy in classifying synthetic data and approximately 83-89% accuracy with experimental data, highlighting the model's performance.

We introduced a symmetry reduction method that significantly reduces training time without compromising accuracy and a distribution-based method for quantifying confidence in multilabel classifier predictions, eliminating the need for adversarial training sets.

Conclusion and future work

Artificial intelligence is transforming the way we relate to the world and is applied in a broad range of fields. However, implementing it with the current architectures is energetically expensive and is reaching what is known as von Neumann's bottleneck. Neuromorphic computing, which takes inspiration from nature, i.e., the biological neural networks that are highly interconnected, parallel, and energetically efficient, is an alternative to conventional architectures aimed at solving this bottleneck and accelerating AI algorithms. Despite this, the architectures alone do not address the issues associated with the current CMOS-based electronic devices used to implement them. There is a need for materials that can closely emulate these biologically and electrically relevant features.

A variety of materials, including transition oxides, have been explored for their potential in mimicking neuron-like behavior. Among these, vanadium dioxide (VO_2) is especially noteworthy since it exhibits an insulating-to-metal transition (IMT) near room temperature, making it potentially practical for real-world applications. This switch could be finely tuned and manipulated, enabling the material to "remember" its state. This is reminiscent of the synaptic functions observed in biological systems, where synapses can strengthen or weaken over time, effectively "remembering" information. Moreover, VO_2 can act as a neuristor, by accumulating phases - metallic sites on an insulating matrix over time - and then reaching a threshold that causes a resistance drop of several orders of magnitude, it 'spikes', similar to the action potential observed in biological neurons.

In this thesis, we investigate the IMT in VO_2 and assess its potential applications in neuromorphic computing by studying memory in the material. VO_2 changes the refractive index from the insulating to metal phases, so we have enough optical contrast in the visible range to apply optical microscopy to study the dynamics of the IMT. This exhibits a distinct phase separation near criticality that reveals a fractal pattern. This phenomenon, observable from the nanometer to micrometer scale, displays the fractal nature of pattern formation. The optical characterization method for VO_2 allowed us to incorporate spatial information which, in turn, improved our understanding of material behavior during its phase transition and facilitated the tailoring of devices. In this comprehensive study, we explored various aspects of the IMT in VO_2 , covering characterization, fabrication methods, and advanced imaging techniques.

The main achievements of our research are highlighted in the following key aspects:

Chapter 3: Mapping Transition Dynamics and Tailoring Sample Characteristics

First, we successfully mapped the critical temperature (T_c), the width of the phase transition (ΔT_c), and the sharpness of the transition (δT_c) in VO_2 samples. This was achieved through a novel approach of tracking pixel intensity over time, providing both spatial and dynamic insights into the transition process. This mapping not only enhances our understanding of the transition behavior but also elucidates the complex interplay of factors influencing phase transition dynamics.

Several new experimental steps were necessary to align, focus, and calibrate the raw grayscale images recorded. These achievements enabled us to accurately track the spatial distribution of metal and insulator clusters, resulting in detailed binary black and white images, time traces, and maps. We observed micron-sized patterns that were largely reproducible through multiple temperature sweeps. The ΔT_c hysteresis width map exhibited an average hysteresis width of 4.3 °C consistent with macroscopic resistivity hysteresis but with significant local variation, ranging from approximately 0 °C in certain small regions to about 8 °C in others.

These findings open new opportunities to access local properties of VO_2 , such as electrically contacting specific parts of the sample to select unique parameter combinations for electrical and optoelectronic devices. The positive correlation between the T_c value and hysteresis width could enable new approaches for tailoring the material's response to external triggers. Additionally, these observations provide new perspectives for studying open questions in the theory of hysteresis. Future work could focus on exploring these local properties further and investigating how different external conditions affect the transition dynamics at a microscopic level.

Second, our research demonstrates the potential for tailoring sample characteristics to meet diverse application requirements, particularly in memory and fast switching functionalities essential for neuromorphic computing paradigms. By identifying the distinct needs for these applications, we can strategically select and design VO_2 samples with specific properties optimized for desired functionalities. This adaptability in sample design opens up new avenues for developing advanced neuromorphic computing systems with improved performance and efficiency.

Lastly, this method facilitates the characterization of VO_2 samples synthesized through different techniques. By obtaining statistical information for each segment of the sample, we gain valuable insights into the impact of various preparation methods on the material properties and transition characteristics. This systematic approach not only enriches our understanding of VO_2 behavior but also provides critical guidance for optimizing sample fabrication processes to

achieve desired performance metrics.

Chapter 4: Optical Imaging of Ramp Reversal Memory in VO₂

In this chapter, we present the pioneering optical imaging of ramp reversal memory (RRM) in VO₂. These experiments provide detailed insights into the spatial distribution of metal and insulator clusters and their evolution during thermal subloop training. Our findings reveal a progression of clusters from one subloop to the next, culminating in a more rugged transition temperature map after applying the RRM protocol. This suggests that memory accumulation extends beyond cluster boundaries at the transition temperature (T_H), permeating deeply into both metal and insulator patches across the sample.

These insights into the RRM mechanism could pave the way for novel memory devices with enhanced robustness and stability. Our findings reveal that clusters evolve by front propagation from one subloop to the next. In successive and accumulated memory maps, we observed that the transition temperature map becomes more rugged after all subloops, indicating that memory accumulates not only at the cluster boundaries at T_H but also deep inside the metal and insulator patches throughout the sample.

Furthermore, our experiments show that the subloop-trained memory disappears as expected when the sample is heated to $T = 82^\circ\text{C}$, just above the closing of the major hysteresis loop. This finding supports the connection between ramp reversal memory and defect mobility. Further work is needed to identify the species of defects contributing to this effect.

The observation of spatially resolved nonvolatile memory encoding in VO₂ paves the way for developing multi-level memory synaptors for neuromorphic computing applications. Additionally, the proposed connection between RRM and defect mobility opens the possibility of enhancing the memory effect through defect engineering methods, such as using dopants, ion irradiation, or tuning material synthesis conditions.

Chapter 5: Machine Learning-Based Criterion for Diagnosing Proximity to Criticality

We proposed a machine learning-based criterion for diagnosing proximity to criticality, validated by successfully classifying Hamiltonians in scanning near-field infrared microscopy (SNOM) and optical microscopy images of VO₂ thin films. Our results confirm that pattern formation in VO₂ is driven by the two-dimensional random field Ising model near a critical point.

We demonstrated that the convolutional neural network (CNN) achieves over 99% accuracy in classifying synthetic data and approximately 83-89% accuracy with experimental data, underscoring the model's robustness. Additionally, we introduced a symmetry reduction method that significantly reduces training time without compromising accuracy, and a distribution-based

method for quantifying confidence in multilabel classifier predictions, eliminating the need for adversarial training sets. These advancements in machine learning methodologies could significantly enhance the analysis of complex phase transitions in correlated materials.

Future Work and Perspectives

The detailed understanding of phase transition dynamics in VO₂ and the ability to tailor material properties for specific applications hold great promise for the development of next-generation memory devices and neuromorphic computing systems. The optical imaging techniques and machine learning approaches introduced in this study provide powerful tools for further exploration of phase transitions in strongly correlated materials. Future research could focus on optimizing the optical characterization set-up for different kinds of triggers like laser or electric pulses, exploring the full potential of RRM in practical devices, and expanding the machine learning framework to other correlated material systems. The study also set out to deepen comprehension of VO₂ IMT and explore how this material could emulate biological neural networks, specifically as neuristors and memristors, thereby contributing to the development of innovative computing paradigms that mirror the functionality of the human brain.

Other opportunities include using an alternative temperature protocol called Ringdown to study how disorder affects the insulator-metal transition (IMT). By analyzing images from the Ringdown protocol and RRM with the developed deep learning classifier, we can determine if there is a shift in the detection of criticality. Additionally, ramping the temperature at rate slower than 1°C/ min, allows us to study avalanches during the IMT and track cluster formation over time. Grayscale images, combined with simultaneous resistance measurements, have also proven valuable in developing a resistor network model that can predict resistance values at a given temperature based solely on the grayscale image of the VO₂ area.

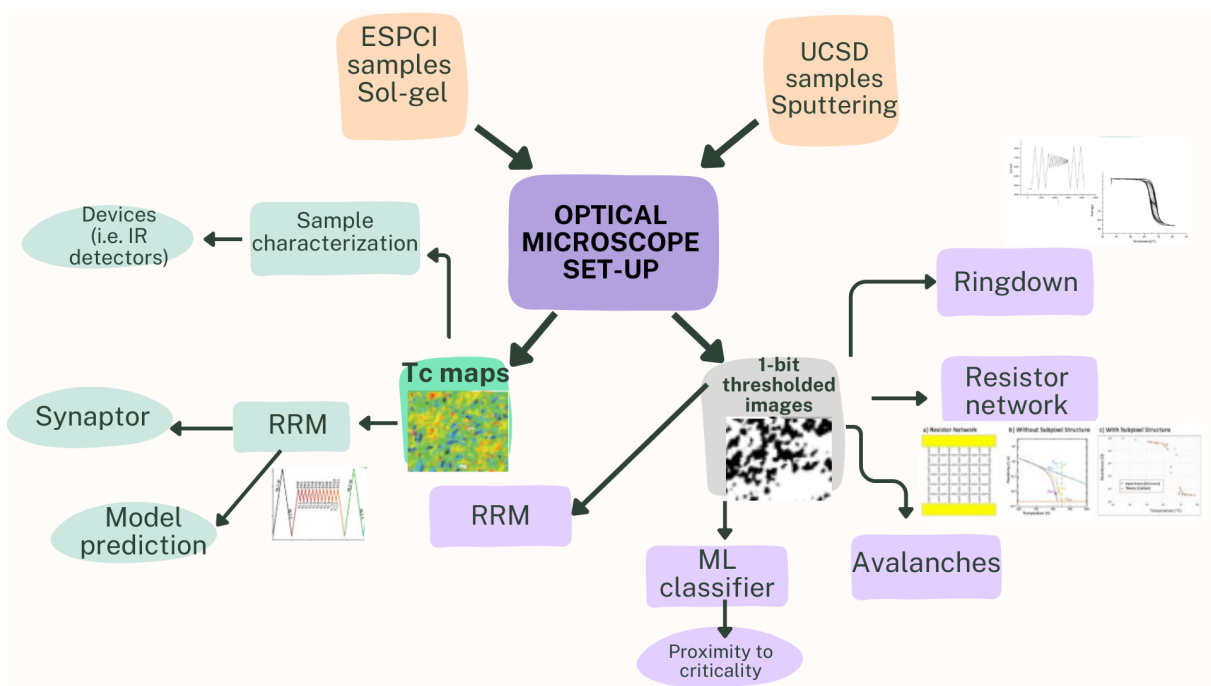


Figure 7.11 – An overview of the applications derived from the optical characterization setup reveals that T_c maps have been used to identify hysteresis features in VO_2 samples synthesized using different methods, such as sol-gel and RF sputtering. The sol-gel samples were provided by Z. Fang from ESPCI, while Professor Schuller from UCSD supplied the RF sputtering samples. These maps not only enhance our understanding of the RRM mechanism but also serve as a valuable tool in other areas. For instance, thresholded images that distinctly depict the insulating and metallic phases are utilized in the deep learning classifier, the tracking of avalanches, and RRM.

List of publications

Peer-reviewed articles

1. Spatially Distributed Ramp Reversal Memory in VO₂.

S. Basak, Y. Sun, M. A. Banguero, P. Salev, I. K. Schuller, L. Aigouy, E. W. Carlson, A. Zimmers. Adv. Electron. Mater. 2023, 9, 2300085 DOI: 10.1002/aelm.202300085

2. Deep learning Hamiltonians from disordered image data in quantum materials.

S. Basak, M. Alzate Banguero, L. Burzawa, F. Simmons, P. Salev, L. Aigouy, M. M. Qazilbash, I. K. Schuller, D. N. Basov, A. Zimmers, and E. W. Carlson Phys. Rev. B 107, 205121 DOI: 10.1103/PhysRevB.107.205121

Articles in preparation

3. Correlative mapping of local hysteresis properties in VO₂

Melissa Alzate Banguero, Sayan Basak, Nicolas Raymond, Forrest Simmons, Pavel Salev, Ivan K Schuller, Lionel Aigouy, Erica W Carlson, Alexandre Zimmers arXiv preprint arXiv:2301.04220 DOI: 10.48550/arXiv.2301.04220

4. Tuning the Resistance of a VO₂ Junction with a Focused Laser Beam and Atomic Force Microscopy

Zhuoqun Fang, Melissa Alzate-Banguero, Amit R. Rajapurohita, Forrest Simmons, Erica W. Carlson, Zhuoying Chen, Lionel Aigouy¹, Alexandre Zimmers Submitted to Adv. Electron. Mater 2024

International conferences

Deep Learning Hamiltonians from Disordered Image Data in Quantum Materials

Melissa Alzate Banguero, Sayan Basak, Lukasz Burzawa, Forrest Simmons, Pavel Salev, Lionel Aigouy, Muhammad Qazilbash, Ivan Schuller, Dmitri Basov, Alexandre Zimmers, Erica Carlson. APS March Meeting Abstracts, Bibcode:2023.2023APS..MARD29013A

Filming the metal-insulator transition - from T_c maps to machine learning pattern recognition

Melissa Alzate Banguero, Sayan Basak, Nicolas Raymond, Forrest Simmons, Pavel Salev, Ivan Schuller, Lionel Aigouy, Alexandre Zimmers, Erica Carlson. APS March Meeting Abstracts, 2022. F63. 013.

Bibliography

- [1] P Russel Norvig and S Artificial Intelligence. « A modern approach ». *Prentice Hall Upper Saddle River, NJ, USA: Rani, M., Nayak, R., & Vyas, OP (2015). An ontology-based adaptive personalized e-learning system, assisted by software agents on cloud storage. Knowledge-Based Systems* 90 (2002), pp. 33–48 (cit. on p. 1).
- [2] Christopher Collins, Denis Dennehy, Kieran Conboy, and Patrick Mikalef. « Artificial intelligence in information systems research: A systematic literature review and research agenda ». *International Journal of Information Management* 60 (2021), p. 102383 (cit. on p. 1).
- [3] Luciano Floridi. « AI as agency without intelligence: On CHATGPT, large language models, and other generative models ». *SSRN* (2023) (cit. on p. 1).
- [4] Norbert Wiener. *Cybernetics: or Control and Communication in the Animal and the Machine*. 2nd ed. Cambridge, MA: MIT Press, 1948 (cit. on p. 1).
- [5] John Jumper, Richard Evans, Alexander Pritzel, Tim Green, Michael Figurnov, Olaf Ronneberger, et al. « Highly accurate protein structure prediction with AlphaFold ». *Nature* 596.7873 (2021), pp. 583–589 (cit. on p. 1).
- [6] Neil C. Thompson, Kristjan H. Greenewald, Keeheon Lee, and Gabriel F. Manso. « The Computational Limits of Deep Learning ». *CoRR* abs/2007.05558 (2020). arXiv: [2007.05558](https://arxiv.org/abs/2007.05558) (cit. on p. 1).
- [7] IEA. *Electricity 2024 – analysis*. 2024 (cit. on p. 1).
- [8] Schneider Electric. *The AI Disruption: Challenges and Guidance for Data Center Design*. 2023 (cit. on p. 1).
- [9] Anders Sandberg and Nick Bostrom. « Whole brain emulation: A roadmap » (2008) (cit. on p. 2).
- [10] Ladislav Kováč. « The 20 W sleep-walkers ». *EMBO reports* 11.1 (2010), pp. 2–2. eprint: <https://www.embopress.org/doi/pdf/10.1038/embor.2009.266> (cit. on p. 2).
- [11] Yiran Chen, Hai (Helen) Li, Chunpeng Wu, Chang Song, Sicheng Li, Chuhan Min, et al. « Neuromorphic computing’s yesterday, today, and tomorrow – an evolutionary view ». *Integration* 61 (2018), pp. 49–61 (cit. on p. 2).
- [12] Catherine D. Schuman, Shruti R. Kulkarni, Maryam Parsa, J. Parker Mitchell, Prasanna Date, and Bill Kay. « Opportunities for neuromorphic computing algorithms and applications ». *Nature Computational Science* 2.1 (2022), pp. 10–19 (cit. on p. 2).
- [13] Zhenzhu Meng, Yating Hu, and Christophe Ancey. « Using a Data Driven Approach to Predict Waves Generated by Gravity Driven Mass Flows ». *Water* 12.2 (2020) (cit. on p. 4).
- [14] Danijela Marković, Alice Mizrahi, Damien Querlioz, and Julie Grollier. « Physics for neuromorphic computing ». *Nature Reviews Physics* 2.9 (2020), pp. 499–510 (cit. on pp. 5, 9).
- [15] Dmitri B. Strukov and Konstantin K. Likharev. « A reconfigurable architecture for hybrid CMOS/Nanodevice circuits ». *Proceedings of the 2006 ACM/SIGDA 14th International Symposium on Field Programmable Gate Arrays*. FPGA '06. Monterey, California, USA: Association for Computing Machinery, 2006, 131–140 (cit. on p. 5).
- [16] J. Feldmann, N. Youngblood, C. D. Wright, H. Bhaskaran, and W. H. P. Pernice. « All-optical spiking neurosynaptic networks with self-learning capabilities ». *Nature* 569.7755 (2019), pp. 208–214 (cit. on p. 5).
- [17] Steve Furber. « Large-scale neuromorphic computing systems ». *Journal of Neural Engineering* 13.5 (2016), p. 051001 (cit. on p. 5).

- [18] Pablo Stoliar, Julien Tranchant, Benoit Corraze, Etienne Janod, Marie-Paule Besland, Federico Tesler, et al. « A Leaky-Integrate-and-Fire Neuron Analog Realized with a Mott Insulator ». *Advanced Functional Materials* 27.11 (2017), p. 1604740. eprint: <https://onlinelibrary.wiley.com/doi/pdf/10.1002/adfm.201604740> (cit. on p. 7).
- [19] Ivan K. Schuller, Rick Stevens, Robinson Pino, and Michael Pechan. « Neuromorphic Computing – From Materials Research to Systems Architecture Roundtable » () (cit. on p. 7).
- [20] Javier del Valle, Juan Gabriel Ramírez, Marcelo J. Rozenberg, and Ivan K. Schuller. « Challenges in materials and devices for resistive-switching-based neuromorphic computing ». *Journal of Applied Physics* 124.21 (2018), p. 211101. eprint: https://pubs.aip.org/aip/jap/article-pdf/doi/10.1063/1.5047800/19911666/211101_1_1_5047800.pdf (cit. on pp. 7, 8, 10, 12, 14).
- [21] Jiayi Li, Haider Abbas, Diing Shenp Ang, Asif Ali, and Xin Ju. « Emerging memristive artificial neuron and synapse devices for the neuromorphic electronics era ». *Nanoscale Horiz.* 8 (11 2023), pp. 1456–1484 (cit. on pp. 7, 9).
- [22] Wenbin Chen, Lekai Song, Shengbo Wang, Zhiyuan Zhang, Guanyu Wang, Guohua Hu, et al. « Essential Characteristics of Memristors for Neuromorphic Computing ». *Advanced Electronic Materials* 9.2 (2023), p. 2200833. eprint: <https://onlinelibrary.wiley.com/doi/pdf/10.1002/aelm.202200833> (cit. on p. 7).
- [23] Qilin Hua, Huaqiang Wu, Bin Gao, Qingtian Zhang, Wei Wu, Yujia Li, et al. « Low-Voltage Oscillatory Neurons for Memristor-Based Neuromorphic Systems ». *Global Challenges* 3.11 (2019), p. 1900015. eprint: <https://onlinelibrary.wiley.com/doi/pdf/10.1002/gch2.201900015> (cit. on p. 7).
- [24] Gyorgy Csaba and Wolfgang Porod. « Coupled oscillators for computing: A review and perspective ». *Applied Physics Reviews* 7.1 (2020), p. 011302. eprint: https://pubs.aip.org/aip/apr/article-pdf/doi/10.1063/1.5120412/14575376/011302_1_online.pdf (cit. on p. 8).
- [25] Qiming Shao, Zhongrui Wang, and J. Joshua Yang. « Efficient AI with MRAM ». *Nature Electronics* 5.2 (2022), pp. 67–68 (cit. on p. 8).
- [26] N. Locatelli, V. Cros, and J. Grollier. « Spin-torque building blocks ». *Nature Materials* 13.1 (2014), pp. 11–20 (cit. on p. 8).
- [27] Adrien F. Vincent, Jérôme Larroque, Nicolas Locatelli, Nesrine Ben Romdhane, Olivier Bichler, Christian Gamrat, et al. « Spin-Transfer Torque Magnetic Memory as a Stochastic Memristive Synapse for Neuromorphic Systems ». *IEEE Transactions on Biomedical Circuits and Systems* 9.2 (2015), pp. 166–174 (cit. on p. 8).
- [28] Piotr Rzeszut, Jakub Chęciński, Ireneusz Brzozowski, Sławomir Ziętek, Witold Skowroński, and Tomasz Stobiecki. « Multi-state MRAM cells for hardware neuromorphic computing ». *Scientific Reports* 12.1 (2022), p. 7178 (cit. on p. 8).
- [29] J. Grollier, D. Querlioz, K. Y. Camsari, K. Everschor-Sitte, S. Fukami, and M. D. Stiles. « Neuromorphic spintronics ». *Nature Electronics* 3.7 (2020), pp. 360–370 (cit. on p. 8).
- [30] and, et al. « Thermal effect of Ge₂Sb₂Te₅ in phase change memory device ». *Chinese Physics B* 23.8 (2014), p. 087804 (cit. on p. 9).
- [31] Xiangwen Wang, Xianghong Lin, and Xiaochao Dang. « Supervised learning in spiking neural networks: A review of algorithms and evaluations ». *Neural Networks* 125 (2020), pp. 258–280 (cit. on p. 9).
- [32] Wenrui Zhang and Peng Li. « Temporal Spike Sequence Learning via Backpropagation for Deep Spiking Neural Networks ». *Advances in Neural Information Processing Systems*. Ed. by H. Larochelle, M. Ranzato, R. Hadsell, M.F. Balcan, and H. Lin. Vol. 33. Curran Associates, Inc., 2020, pp. 12022–12033 (cit. on p. 9).
- [33] Erbin Qiu, Yuan-Hang Zhang, Massimiliano Di Ventra, and Ivan K. Schuller. « Reconfigurable Cascaded Thermal Neuristors for Neuromorphic Computing ». *Advanced Materials* 36.6 (2024), p. 2306818. eprint: <https://onlinelibrary.wiley.com/doi/pdf/10.1002/adma.202306818> (cit. on pp. 10, 12, 16).
- [34] Qingxi Duan, Zhaokun Jing, Xiaolong Zou, Yanghao Wang, Ke Yang, Teng Zhang, et al. « Spiking neurons with spatiotemporal dynamics and gain modulation for monolithically integrated memristive neural networks ». *Nature Communications* 11.1 (2020), p. 3399 (cit. on p. 11).
- [35] Miguel Romera, Philippe Talatchian, Sumito Tsunegi, Flavio Abreu Araujo, Vincent Cros, Paolo Bortolotti, et al. « Vowel recognition with four coupled spin-torque nano-oscillators ». *Nature* 563.7730 (2018), pp. 230–234 (cit. on pp. 11, 13).
- [36] T. Böhnert, Y. Rezaeiyan, M. S. Claro, L. Benetti, A. S. Jenkins, H. Farkhani, et al. « Weighted spin torque nano-oscillator system for neuromorphic computing ». *Communications Engineering* 2.1 (2023), p. 65 (cit. on p. 11).

- [37] Bo Xu, Yuhao Huang, Yuetong Fang, Zhongrui Wang, Shaoliang Yu, and Renjing Xu. « Recent Progress of Neuromorphic Computing Based on Silicon Photonics: Electronic–Photonic Co-Design, Device, and Architecture ». *Photonics* 9.10 (2022) (cit. on p. 11).
- [38] Karol Fröhlich, Ivan Kundrata, Michal Blaho, Marian Precner, Milan Ľapajna, Martin Klimo, et al. « Hafnium oxide and tantalum oxide based resistive switching structures for realization of minimum and maximum functions ». *Journal of Applied Physics* 124.15 (2018), p. 152109. eprint: https://pubs.aip.org/aip/jap/article-pdf/doi/10.1063/1.5025802/15216674/152109\1\1_online.pdf (cit. on p. 12).
- [39] Mi Ra Park, Yawar Abbas, Haider Abbas, Quanli Hu, Tae Sung Lee, Young Jin Choi, et al. « Resistive switching characteristics in hafnium oxide, tantalum oxide and bilayer devices ». *Microelectronic Engineering* 159 (2016), pp. 190–197 (cit. on p. 14).
- [40] L. Goux, P. Czarnecki, Y. Y. Chen, L. Pantisano, X. P. Wang, R. Degraeve, et al. « Evidences of oxygen-mediated resistive-switching mechanism in TiN HfO₂ Pt cells ». *Applied Physics Letters* 97.24 (2010), p. 243509. eprint: https://pubs.aip.org/aip/apl/article-pdf/doi/10.1063/1.3527086/14443561/243509\1\1_online.pdf (cit. on p. 14).
- [41] B. J. Choi, D. S. Jeong, S. K. Kim, C. Rohde, S. Choi, J. H. Oh, et al. « Resistive switching mechanism of TiO₂ thin films grown by atomic-layer deposition ». *Journal of Applied Physics* 98.3 (2005), p. 033715. eprint: https://pubs.aip.org/aip/jap/article-pdf/doi/10.1063/1.2001146/13271932/033715\1\1_online.pdf (cit. on p. 14).
- [42] Hongjun Wang, Yuanyuan Zhu, and Dejun Fu. « Coexistence of bipolar and unipolar resistive switching characteristics of thin TiO₂ film grown on Cu foil substrate for flexible nonvolatile memory device ». *Journal of Alloys and Compounds* 695 (2017), pp. 2669–2671 (cit. on p. 14).
- [43] Deok-Hwang Kwon, Kyung Min Kim, Jae Hyuck Jang, Jong Myeong Jeon, Min Hwan Lee, Gun Hwan Kim, et al. « Atomic structure of conducting nanofilaments in TiO₂ resistive switching memory ». *Nature Nanotechnology* 5.2 (2010), pp. 148–153 (cit. on p. 14).
- [44] Tsung-Han Yang, Ravi Aggarwal, Alok Gupta, Honghui Zhou, Roger J. Narayan, and J. Narayan. « Semiconductor-metal transition characteristics of VO₂ thin films grown on c- and r-sapphire substrates ». *Journal of Applied Physics* 107.5 (2010), p. 053514. eprint: https://pubs.aip.org/aip/jap/article-pdf/doi/10.1063/1.3327241/15052236/053514\1\1_online.pdf (cit. on pp. 14, 66).
- [45] Min Kyu Yang, Hyunsu Ju, Gun Hwan Kim, Jeon-Kook Lee, and Han-Cheol Ryu. « Direct evidence on Ta-Metal Phases Igniting Resistive Switching in TaOx Thin Film ». *Scientific Reports* 5.1 (2015), p. 14053 (cit. on p. 14).
- [46] Agnes Gubicza, Miklós Csontos, András Halbritter, and György Mihály. « Non-exponential resistive switching in Ag₂S memristors: a key to nanometer-scale non-volatile memory devices ». *Nanoscale* 7 (10 2015), pp. 4394–4399 (cit. on p. 14).
- [47] Hisashi Shima, Fumiyoshi Takano, Hiro Akinaga, Yukio Tamai, Isao H. Inoue, and Hide Takagi. « Resistance switching in the metal deficient-type oxides: NiO and CoO ». *Applied Physics Letters* 91.1 (2007), p. 012901. eprint: https://pubs.aip.org/aip/apl/article-pdf/doi/10.1063/1.2753101/13668594/012901\1\1_online.pdf (cit. on p. 14).
- [48] S. Seo, M. J. Lee, D. H. Seo, E. J. Jeoung, D.-S. Suh, Y. S. Joung, et al. « Reproducible resistance switching in polycrystalline NiO films ». *Applied Physics Letters* 85.23 (2004), pp. 5655–5657. eprint: https://pubs.aip.org/aip/apl/article-pdf/85/23/5655/18602711/5655\1\1_online.pdf (cit. on p. 14).
- [49] Jun Yao, Zhengzong Sun, Lin Zhong, Douglas Natelson, and James M. Tour. « Resistive Switches and Memories from Silicon Oxide ». *Nano Letters* 10.10 (2010), pp. 4105–4110 (cit. on p. 14).
- [50] Fang Nie, Jie Wang, Hong Fang, Shuang Ma, Feiyang Wu, Wenbo Zhao, et al. « Ultrathin SrTiO₃-based oxide memristor with both drift and diffusive dynamics as versatile synaptic emulators for neuromorphic computing ». *Materials Futures* 2.3 (2023), p. 035302 (cit. on p. 14).
- [51] Ben Walters, Mohan V. Jacob, Amirali Amirsoleimani, and Mostafa Rahimi Azghadi. « A Review of Graphene-Based Memristive Neuromorphic Devices and Circuits ». *Advanced Intelligent Systems* 5.10 (2023), p. 2300136. eprint: <https://onlinelibrary.wiley.com/doi/pdf/10.1002/aisy.202300136> (cit. on p. 14).
- [52] W. C. Chien, Y. C. Chen, E. K. Lai, Y. D. Yao, P. Lin, S. F. Horng, et al. « Unipolar Switching Behaviors of RTO WO_x RRAM ». *IEEE Electron Device Letters* 31.2 (2010), pp. 126–128 (cit. on p. 14).

- [53] Javier del Valle, Pavel Salev, Yoav Kalcheim, and Ivan K. Schuller. « A caloritronics-based Mott neuristor ». *Scientific Reports* 10.1 (2020), p. 4292 (cit. on pp. 12, 15).
- [54] Madeleine Abernot, Nadine Azemard, and Aida Todri-Sanial. « Oscillatory neural network learning for pattern recognition: an on-chip learning perspective and implementation ». *Frontiers in Neuroscience* 17 (2023) (cit. on p. 14).
- [55] Elisabetta Corti, Bernd Gotsmann, Kirsten Moselund, Adrian M. Ionescu, John Robertson, and Siegfried Karg. « Scaled resistively-coupled VO₂ oscillators for neuromorphic computing ». *Solid-State Electronics* 168 (2020), p. 107729 (cit. on p. 14).
- [56] Wei Yi, Kenneth K. Tsang, Stephen K. Lam, Xiwei Bai, Jack A. Crowell, and Elias A. Flores. « Biological plausibility and stochasticity in scalable VO₂ active memristor neurons ». *Nature Communications* 9.1 (2018), p. 4661 (cit. on pp. 14, 15).
- [57] Upanya Khandelwal, Rama Satya Sandilya, Rajeev Kumar Rai, Deepak Sharma, Smruti Rekha Mahapatra, Debasish Mondal, et al. « Large electro-opto-mechanical coupling in VO₂ neuristors ». *Applied Physics Reviews* 11.2 (2024), p. 021410. eprint: https://pubs.aip.org/aip/apr/article-pdf/doi/10.1063/5.0169859/19886910/021410_1_5.0169859.pdf (cit. on p. 14).
- [58] Juan Núñez, José M. Quintana, María J. Avedillo, Manuel Jiménez, Aida Todri-Sanial, Elisabetta Corti, et al. « Insights Into the Dynamics of Coupled VO₂ Oscillators for ONNs ». *IEEE Transactions on Circuits and Systems II: Express Briefs* 68.10 (2021), pp. 3356–3360 (cit. on p. 14).
- [59] Sangheon Oh, Yuhan Shi, Javier del Valle, Pavel Salev, Yichen Lu, Zhisheng Huang, et al. « Energy-efficient Mott activation neuron for full-hardware implementation of neural networks ». *Nature Nanotechnology* 16.6 (2021), pp. 680–687 (cit. on p. 15).
- [60] Rui Yuan, Pek Jun Tiw, Lei Cai, Zhiyu Yang, Chang Liu, Teng Zhang, et al. « A neuromorphic physiological signal processing system based on VO₂ memristor for next-generation human-machine interface ». *Nature Communications* 14.1 (2023), p. 3695 (cit. on p. 15).
- [61] Jiajie Ying, Fuhong Min, and Guangyi Wang. « Neuromorphic behaviors of VO₂ memristor-based neurons ». *Chaos, Solitons Fractals* 175 (2023), p. 114058 (cit. on p. 15).
- [62] Chuan Yu Han, Zheng Rong Han, Sheng Li Fang, Shi Quan Fan, Jun Qing Yin, Wei Hua Liu, et al. « Characterization and Modelling of Flexible VO₂ Mott Memristor for the Artificial Spiking Warm Receptor ». *Advanced Materials Interfaces* 9.19 (2022), p. 2200394. eprint: <https://onlinelibrary.wiley.com/doi/pdf/10.1002/admi.202200394> (cit. on p. 15).
- [63] Nareg Ghazikhanian, Javier del Valle, Pavel Salev, Ralph El Hage, Yoav Kalcheim, Coline Adda, et al. « Resistive switching localization by selective focused ion beam irradiation ». *Applied Physics Letters* 123.12 (2023), p. 123505. eprint: https://pubs.aip.org/aip/apl/article-pdf/doi/10.1063/5.0151823/18131881/123505_1_5.0151823.pdf (cit. on pp. 15, 16).
- [64] Shaobo Cheng, Min-Han Lee, Xing Li, Lorenzo Fratino, Federico Tesler, Myung-Geun Han, et al. « Operando characterization of conductive filaments during resistive switching in Mott VOVO₂ ». *Proceedings of the National Academy of Sciences* 118.9 (2021), e2013676118. eprint: <https://www.pnas.org/doi/pdf/10.1073/pnas.2013676118> (cit. on p. 16).
- [65] Elihu Anouchi, Tony Yamin, and Amos Sharoni. « Three-Terminal VO₂-Based Device with Internal Read-Write Switching ». *Phys. Rev. Appl.* 19 (3 2023), p. 034057 (cit. on p. 16).
- [66] Andrei Velichko, Vadim Putrolaynen, and Maksim Belyaev. « Higher-order and long-range synchronization effects for classification and computing in oscillator-based spiking neural networks ». *Neural Computing and Applications* 33.8 (2021), pp. 3113–3131 (cit. on p. 16).
- [67] Luisa Whittaker, Christopher J. Patridge, and Sarbajit Banerjee. « Microscopic and Nanoscale Perspective of the MetalInsulator Phase Transitions of VO₂: Some New Twists to an Old Tale ». *The Journal of Physical Chemistry Letters* 2.7 (2011), pp. 745–758 (cit. on pp. 21, 22).
- [68] Peng Hu, Ping Hu, Tuan Duc Vu, Ming Li, Shancheng Wang, Yujie Ke, et al. « Vanadium Oxide: Phase Diagrams, Structures, Synthesis, and Applications ». *Chemical Reviews* 123 (8 2023), pp. 4353–4415 (cit. on p. 20).
- [69] Tetiana Slusar, Jin Cheol Cho, Bong Jun Kim, Sun Jin Yun, and Hyun Tak Kim. « Epitaxial growth of higher transition-temperature VO₂ films on AlN/Si ». *APL Materials* 4 (2 2016) (cit. on p. 20).
- [70] Dmitry Ruzmetov, Kevin T Zawilski, Sanjaya D Senanayake, Venkatesh Narayanamurti, and Shriram Ramanathan. « Infrared reflectance and photoemission spectroscopy studies across the phase transition boundary in thin film vanadium dioxide ». *Journal of Physics: Condensed Matter* 20.46 (2008), p. 465204 (cit. on p. 20).

- [71] Carlos Batista, Ricardo M. Ribeiro, and Vasco Teixeira. « Synthesis and characterization of VO₂-based thermochromic thin films for energy-efficient windows ». *Nanoscale Research Letters* 6.1 (2011), p. 301 (cit. on p. 20).
- [72] Delphine Malarde, Michael J. Powell, Raul Quesada-Cabrera, Rachel L. Wilson, Claire J. Carmalt, Gopinathan Sankar, et al. « Optimized Atmospheric-Pressure Chemical Vapor Deposition Thermochromic VO₂ Thin Films for Intelligent Window Applications ». *ACS Omega* 2.3 (2017), pp. 1040–1046 (cit. on pp. 20, 28).
- [73] Maksim A. Belyaev, Vadim V. Putrolaynen, Andrey A. Velichko, Genrikh B. Stefanovich, and Alexander L. Pergament. « Field-effect modulation of resistance in VO₂ thin film at lower temperature ». *Japanese Journal of Applied Physics* 53.11 (2014), p. 111102 (cit. on p. 20).
- [74] Francine C. Case. « Improved VO₂ thin films for infrared switching ». *Appl. Opt.* 30.28 (1991), pp. 4119–4123 (cit. on p. 20).
- [75] Roseanna G. Lawandi, Dylan Morden, Imad Agha, Shivashankar Vangala, and Andrew M. Sarangan. « VO₂ wire grid polarizers for MWIR applications ». *J. Opt. Soc. Am. B* 41.3 (2024), pp. 744–749 (cit. on p. 20).
- [76] Mohammad Samizadeh Nikoo, Reza Soleimanzadeh, Anna Krammer, Guilherme Migliato Marega, Yunkyung Park, Junwoo Son, et al. « Electrical control of glass-like dynamics in vanadium dioxide for data storage and processing ». *Nature Electronics* 5.9 (2022), pp. 596–603 (cit. on p. 20).
- [77] Jiahua Qi, Dongping Zhang, Qicong He, Lanxuan Zeng, Yi Liu, Zhuangbing Wang, et al. « Independent regulation of electrical properties of VO₂ for low threshold voltage electro-optic switch applications ». *Sensors and Actuators A: Physical* 335 (2022), p. 113394 (cit. on p. 20).
- [78] D. Kucharczyk and T. Niklewski. « Accurate X-ray determination of the lattice parameters and the thermal expansion coefficients of VO₂ near the transition temperature ». *Journal of Applied Crystallography* 12.4 (1979), pp. 370–373. eprint: <https://onlinelibrary.wiley.com/doi/pdf/10.1107/S0021889879012711> (cit. on p. 22).
- [79] Chang Lu, Qingjian Lu, Min Gao, and Yuan Lin. « Dynamic manipulation of thz waves enabled by phase-transition VO₂ thin film ». *Nanomaterials* 11 (1 2021), pp. 1–27 (cit. on p. 22).
- [80] C. N. Berglund and H. J. Guggenheim. « Electronic Properties of VO₂ near the Semiconductor-Metal Transition ». *Phys. Rev.* 185 (3 1969), pp. 1022–1033 (cit. on p. 22).
- [81] Mohammad Moein Seyfour and Russell Binions. « Sol-gel approaches to thermochromic vanadium dioxide coating for smart glazing application ». *Solar Energy Materials and Solar Cells* 159 (2017), pp. 52–65 (cit. on pp. 22, 28).
- [82] F J Morin. « NUMBER PHYSICAL REVIEW LETTERS Jvr ». 3 (), p. 1959 (cit. on p. 22).
- [83] Renata M. Wentzcovitch, Werner W. Schulz, and Philip B. Allen. « VO₂: Peierls or Mott-Hubbard? A view from band theory ». *Phys. Rev. Lett.* 72 (21 1994), pp. 3389–3392 (cit. on p. 22).
- [84] M. M. Qazilbash, M. Brehm, Byung-Gyu Chae, P.-C. Ho, G. O. Andreev, Bong-Jun Kim, et al. « Mott Transition in VO₂ Revealed by Infrared Spectroscopy and Nano-Imaging ». *Science* 318.5857 (2007), pp. 1750–1753. eprint: <https://www.science.org/doi/pdf/10.1126/science.1150124> (cit. on pp. 23, 29–31, 33, 39, 42, 60).
- [85] Lei Wang, Irina Novikova, John M. Klopff, Scott Madaras, Gwyn P. Williams, Eric Madaras, et al. « Distinct Length Scales in the VO₂ Metal–Insulator Transition Revealed by Bi-chromatic Optical Probing ». *Advanced Optical Materials* 2.1 (2014), pp. 30–33. eprint: <https://onlinelibrary.wiley.com/doi/pdf/10.1002/adom.201300333> (cit. on p. 23).
- [86] V. A. Klimov, I. O. Timofeeva, S. D. Khanin, E. B. Shadrin, A. V. Ilinskii, and F. Silva-Andrade. « Hysteresis loop construction for the metal-semiconductor phase transition in vanadium dioxide films ». *Technical Physics* 47.9 (2002), pp. 1134–1139 (cit. on p. 23).
- [87] Christophe Petit, Jean-Marc Frigerio, and Michel Goldmann. « Hysteresis of the metal-insulator transition of ; evidence of the influence of microscopic texturation ». *Journal of Physics: Condensed Matter* 11.16 (1999), p. 3259 (cit. on p. 23).
- [88] Masami Nishikawa, Tomohiko Nakajima, Toshiya Kumagai, Takeshi Okutani, and Tetsuo Tsuchiya. « Adjustment of thermal hysteresis in epitaxial VO₂ films by doping metal ions ». *Journal of the Ceramic Society of Japan* 119.1391 (2011), pp. 577–580 (cit. on p. 23).
- [89] Yannick Bleu, Florent Bourquard, Vincent Barnier, Anne-Sophie Loir, Florence Garrelie, and Christophe Donnet. « Towards Room Temperature Phase Transition of W-Doped VO₂ Thin Films Deposited by Pulsed Laser Deposition: Thermochromic, Surface, and Structural Analysis ». *Materials* 16.1 (2023) (cit. on pp. 23, 25).

- [90] Bongjin Simon Mun, Joonseok Yoon, Sung-Kwan Mo, Kai Chen, Nobumichi Tamura, Catherine Dejoie, et al. « Role of joule heating effect and bulk-surface phases in voltage-driven metal-insulator transition in VO₂ crystal ». *Applied Physics Letters* 103.6 (2013), p. 061902. eprint: https://pubs.aip.org/aip/apl/article-pdf/doi/10.1063/1.4817727/14290851/061902_1_online.pdf (cit. on p. 23).
- [91] Iuliana P Radu, B Govoreanu, S Mertens, X Shi, M Cantoro, M Schaekers, et al. « Switching mechanism in two-terminal vanadium dioxide devices ». *Nanotechnology* 26.16 (2015), p. 165202 (cit. on p. 23).
- [92] S. B. Lee, K. Kim, J. S. Oh, B. Kahng, and J. S. Lee. « Origin of variation in switching voltages in threshold-switching phenomena of VO₂ thin films ». *Applied Physics Letters* 102.6 (2013), p. 063501. eprint: https://pubs.aip.org/aip/apl/article-pdf/doi/10.1063/1.4790842/14280884/063501_1_online.pdf (cit. on p. 23).
- [93] A. Zimmers, L. Aigouy, M. Mortier, A. Sharoni, Siming Wang, K. G. West, et al. « Role of Thermal Heating on the Voltage Induced Insulator-Metal Transition in VO₂ ». *Phys. Rev. Lett.* 110 (5 2013), p. 056601 (cit. on p. 23).
- [94] Gokul Gopalakrishnan, Dmitry Ruzmetov, and Shriram Ramanathan. « On the triggering mechanism for the metal-insulator transition in thin film VO₂ devices: electric field versus thermal effects ». *Journal of Materials Science* 44.19 (2009), pp. 5345–5353 (cit. on p. 23).
- [95] G Stefanovich, A Pergament, and D Stefanovich. « Electrical switching and Mott transition in VO₂ ». *Journal of Physics: Condensed Matter* 12.41 (2000), p. 8837 (cit. on p. 23).
- [96] Kunio Okimura and Joe Sakai. « Time-dependent Characteristics of Electric Field-induced Metal-Insulator Transition of Planer VO₂/c-Al₂O₃ Structure ». *Japanese Journal of Applied Physics* 46.9L (2007), p. L813 (cit. on p. 23).
- [97] Suhas Kumar, Matthew D. Pickett, John Paul Strachan, Gary Gibson, Yoshio Nishi, and R. Stanley Williams. « Local Temperature Redistribution and Structural Transition During Joule-Heating-Driven Conductance Switching in VO₂ ». *Advanced Materials* 25.42 (2013), pp. 6128–6132. eprint: <https://onlinelibrary.wiley.com/doi/pdf/10.1002/adma.201302046> (cit. on p. 23).
- [98] Dasheng Li, Abhishek A. Sharma, Darshil K. Gala, Nikhil Shukla, Hanjong Paik, Suman Datta, et al. « Joule Heating-Induced Metal-Insulator Transition in Epitaxial VO₂/TiO₂ Devices ». *ACS Applied Materials & Interfaces* 8.20 (2016), pp. 12908–12914 (cit. on p. 23).
- [99] Naga Phani B Aetukuri. *THE CONTROL OF METAL-INSULATOR TRANSITION*. 2013 (cit. on p. 23).
- [100] Yoav Kalcheim, Alberto Camjayi, Javier del Valle, Pavel Salev, Marcelo Rozenberg, and Ivan K. Schuller. « Non-thermal resistive switching in Mott insulator nanowires ». *Nature Communications* 11.1 (2020), p. 2985 (cit. on p. 23).
- [101] Zhenhua Zhang, Hua Guo, Wenqiang Ding, Bin Zhang, Yue Lu, Xiaoxing Ke, et al. « Nanoscale Engineering in VO₂ Nanowires via Direct Electron Writing Process ». *Nano Letters* 17.2 (2017), pp. 851–855 (cit. on pp. 23, 24).
- [102] S. H. Dietze, M. J. Marsh, Siming Wang, J.-G. Ramírez, Z.-H. Cai, J. R. Mohanty, et al. « X-ray-induced persistent photoconductivity in vanadium dioxide ». *Phys. Rev. B* 90 (16 2014), p. 165109 (cit. on pp. 23, 24).
- [103] Hai-Tian Zhang, Lu Guo, Greg Stone, Lei Zhang, Yuan-Xia Zheng, Eugene Freeman, et al. « Imprinting of Local Metallic States into VO₂ with Ultraviolet Light ». *Advanced Functional Materials* 26.36 (2016), pp. 6612–6618. eprint: <https://onlinelibrary.wiley.com/doi/pdf/10.1002/adfm.201601890> (cit. on p. 23).
- [104] Ge Li, Donggang Xie, Hai Zhong, Ziyi Zhang, Xingke Fu, Qingli Zhou, et al. « Photo-induced non-volatile VO₂ phase transition for neuromorphic ultraviolet sensors ». *Nature Communications* 13.1 (2022), p. 1729 (cit. on pp. 23, 24).
- [105] Scott Madaras. « Insulator To Metal Transition Dynamics Of Vanadium Dioxide Thin Insulator To Metal Transition Dynamics Of Vanadium Dioxide Thin Films Films » (2020) (cit. on p. 23).
- [106] Daniel Wegkamp and Julia Stähler. « Ultrafast dynamics during the photoinduced phase transition in VO₂ ». *Progress in Surface Science* 90.4 (2015), pp. 464–502 (cit. on pp. 25, 33).
- [107] Ningyi Yuan, Jinhua Li, Ge Li, and Xiaoshuang Chen. « The large modification of phase transition characteristics of VO₂ films on SiO₂/Si substrates ». *Thin Solid Films* 515.4 (2006), pp. 1275–1279 (cit. on p. 25).

- [108] Shi Chen, Zhaowu Wang, Hui Ren, Yuliang Chen, Wensheng Yan, Chengming Wang, et al. « Gate-controlled VO₂ phase transition for high-performance smart windows ». *Science Advances* 5.3 (2019), eaav6815. eprint: <https://www.science.org/doi/pdf/10.1126/sciadv.aav6815> (cit. on p. 25).
- [109] Mohammad Taha, Sumeet Walia, Taimur Ahmed, Daniel Headland, Withawat Withayachumnankul, Sharath Sriram, et al. « Insulator–metal transition in substrate-independent VO₂ thin film for phase-change devices ». *Scientific Reports* 7.1 (2017), p. 17899 (cit. on p. 25).
- [110] J. Duchene, M. Terrailon, P. Pailly, and G. Adam. « Filamentary Conduction in VO₂ Coplanar Thin-Film Devices ». *Applied Physics Letters* 19.4 (1971), pp. 115–117. eprint: <https://pubs.aip.org/aip/apl/article-pdf/19/4/115/18425057/115\1\online.pdf> (cit. on p. 25).
- [111] B K Ridley and T B Watkins. « The Possibility of Negative Resistance Effects in Semiconductors ». *Proceedings of the Physical Society* 78.2 (1961), p. 293 (cit. on p. 25).
- [112] R.L. Remke, R.M. Walsler, and R.W. Bené. « The effect of interfaces on electronic switching in VO₂ thin films ». *Thin Solid Films* 97.2 (1982), pp. 129–143 (cit. on pp. 25, 26).
- [113] Elisabetta CORTI. « Networks of Coupled VO₂ Oscillators for Neuromorphic Computing » (2021) (cit. on p. 26).
- [114] Marc Currie, Virginia D. Wheeler, Brian Downey, Neeraj Nepal, Syed B. Qadri, James A. Wollmershauser, et al. « Asymmetric hysteresis in vanadium dioxide thin films ». *Opt. Mater. Express* 9.9 (2019), pp. 3717–3728 (cit. on pp. 26, 27).
- [115] Chunzi Zhang, Cyril Koughia, Ozan Güneş, Jun Luo, Nazmul Hossain, Yuanshi Li, et al. « Synthesis, structure and optical properties of high-quality VO₂ thin films grown on silicon, quartz and sapphire substrates by high temperature magnetron sputtering: Properties through the transition temperature ». *Journal of Alloys and Compounds* 848 (2020), p. 156323 (cit. on p. 27).
- [116] D. H. Kim and H. S. Kwok. « Pulsed laser deposition of VO₂ thin films ». *Applied Physics Letters* 65.25 (1994), pp. 3188–3190. eprint: <https://pubs.aip.org/aip/apl/article-pdf/65/25/3188/18508634/3188\1\online.pdf> (cit. on p. 29).
- [117] Tobias Peterseim, Martin Dressel, Marc Dietrich, and Angelika Polity. « Optical properties of VO₂ films at the phase transition: Influence of substrate and electronic correlations ». *Journal of Applied Physics* 120.7 (2016), p. 075102. eprint: <https://pubs.aip.org/aip/jap/article-pdf/doi/10.1063/1.4961406/14885348/075102\1\online.pdf> (cit. on p. 33).
- [118] Fritz Keilmann and Rainer Hillenbrand. « Near-Field Microscopy by Elastic Light Scattering from a Tip ». *Philosophical Transactions: Mathematical, Physical and Engineering Sciences* 362.1817 (2004), pp. 787–805 (cit. on pp. 29, 33).
- [119] Mengkun Liu, Martin Wagner, Jingdi Zhang, Alexander McLeod, Salinporn Kittiwatanakul, Zhe Fei, et al. « Symmetry breaking and geometric confinement in VO₂: Results from a three-dimensional infrared nano-imaging ». *Applied Physics Letters* 104.12 (2014), p. 121905. eprint: <https://pubs.aip.org/aip/apl/article-pdf/doi/10.1063/1.4869558/14292852/121905\1\online.pdf> (cit. on p. 33).
- [120] T. Togashi, K. Yamamoto, R. Eguchi, Y. Takata, A. Chainani, T. Kiss, et al. « Time-resolved Photoemission Spectroscopy of the Photo-Induced Phase Transition in VO₂ ». *15th International Conference on Ultrafast Phenomena*. Optica Publishing Group, 2006, FB5 (cit. on p. 33).
- [121] T. L. Cocker, L. V. Titova, S. Fourmaux, G. Holloway, H.-C. Bandulet, D. Brassard, et al. « Time-resolved THz spectroscopy of the ultrafast photoinduced insulator-metal phase transition of VO₂ ». *Research in Optical Sciences*. Optica Publishing Group, 2012, IT4D.3 (cit. on p. 33).
- [122] A. Leitenstorfer, C. Kübler, R. Lopez, A. Halabica, R. F. Haglund, and R. Huber. « Ultrafast insulator-metal transition in VO₂: interplay between coherent lattice motion and electronic correlations ». *physica status solidi c* 6.1 (2009), pp. 149–151. eprint: <https://onlinelibrary.wiley.com/doi/pdf/10.1002/pssc.200879860> (cit. on p. 33).
- [123] Y. J. Chang, J. S. Yang, Y. S. Kim, D. H. Kim, T. W. Noh, D.-W. Kim, et al. « Surface versus bulk characterizations of electronic inhomogeneity in a VO₂ thin film ». *Phys. Rev. B* 76 (7 2007), p. 075118 (cit. on p. 33).
- [124] M. M. Qazilbash, A. Tripathi, A. A. Schafgans, Bong-Jun Kim, Hyun-Tak Kim, Zhonghou Cai, et al. « Nanoscale imaging of the electronic and structural transitions in vanadium dioxide ». *Phys. Rev. B* 83 (16 2011), p. 165108 (cit. on pp. 32, 33).

- [125] Suhas Kumar, John Paul Strachan, Matthew D. Pickett, Alexander Bratkovsky, Yoshio Nishi, and R. Stanley Williams. « Sequential Electronic and Structural Transitions in VO₂ Observed Using X-ray Absorption Spectromicroscopy ». *Advanced Materials* 26.44 (2014), pp. 7505–7509. eprint: <https://onlinelibrary.wiley.com/doi/pdf/10.1002/adma.201402404> (cit. on pp. 32, 33).
- [126] D. D. Sarma, Dinesh Topwal, U. Manju, S. R. Krishnakumar, M. Bertolo, S. La Rosa, et al. « Direct Observation of Large Electronic Domains with Memory Effect in Doped Manganites ». *Phys. Rev. Lett.* 93 (9 2004), p. 097202 (cit. on p. 33).
- [127] T. Miyamachi, A. Sekiyama, S. Imada, H. Fujiwara, T. Saita, H. Higashimichi, et al. « Bulk sensitive core-level photoemission spectroscopy of VO₂ ». *Journal of Magnetism and Magnetic Materials* 310.2, Part 1 (2007), e252–e254 (cit. on p. 33).
- [128] T. Becker, C. Streng, Y. Luo, V. Moshnyaga, B. Damaschke, N. Shannon, et al. « Intrinsic Inhomogeneities in Manganite Thin Films Investigated with Scanning Tunneling Spectroscopy ». *Phys. Rev. Lett.* 89 (23 2002), p. 237203 (cit. on p. 33).
- [129] Tobias Peterseim, Martin Dressel, Marc Dietrich, and Angelika Polity. « Optical properties of VO₂ films at the phase transition: Influence of substrate and electronic correlations ». *Journal of Applied Physics* 120.7 (2016), p. 075102. eprint: https://pubs.aip.org/aip/jap/article-pdf/doi/10.1063/1.4961406/14885348/075102_1_online.pdf (cit. on p. 33).
- [130] Ahrum Sohn, Teruo Kanki, Kotaro Sakai, Hidekazu Tanaka, and Dong-Wook Kim. « Fractal Nature of Metallic and Insulating Domain Configurations in a VO₂ Thin Film Revealed by Kelvin Probe Force Microscopy ». *Scientific Reports* 5.1 (2015), p. 10417 (cit. on pp. 30, 31, 33, 42).
- [131] A. Cavalleri, Cs. Tóth, C. W. Siders, J. A. Squier, F. Ráksi, P. Forget, et al. « Femtosecond Structural Dynamics in VO₂ during an Ultrafast Solid-Solid Phase Transition ». *Phys. Rev. Lett.* 87 (23 2001), p. 237401 (cit. on p. 33).
- [132] Allan S. Johnson, Daniel Perez-Salinas, Khalid M. Siddiqui, Sungwon Kim, Sungwook Choi, Klara Volckaert, et al. « Ultrafast X-ray imaging of the light-induced phase transition in VO₂ ». *Nature Physics* 19.2 (2023), pp. 215–220 (cit. on p. 33).
- [133] Chenhang Xu, Cheng Jin, Zijing Chen, Qi Lu, Yun Cheng, Bo Zhang, et al. « Transient dynamics of the phase transition in VO₂ revealed by mega-electron-volt ultrafast electron diffraction ». *Nature Communications* 14.1 (2023), p. 1265 (cit. on p. 33).
- [134] H. S. Choi, J. S. Ahn, J. H. Jung, T. W. Noh, and D. H. Kim. « Mid-infrared properties of a VO₂ film near the metal-insulator transition ». *Phys. Rev. B* 54 (7 1996), pp. 4621–4628 (cit. on pp. 29, 31).
- [135] K. W. Post, A. S. McLeod, M. Hepting, M. Bluschke, Yifan Wang, G. Cristiani, et al. « Coexisting first- and second-order electronic phase transitions in a correlated oxide ». *Nature Physics* 14.10 (2018), pp. 1056–1061 (cit. on p. 29).
- [136] A. Frenzel, M. M. Qazilbash, M. Brehm, Byung-Gyu Chae, Bong-Jun Kim, Hyun-Tak Kim, et al. « Inhomogeneous electronic state near the insulator-to-metal transition in the correlated oxide VO₂ ». *Phys. Rev. B* 80 (11 2009), p. 115115 (cit. on p. 29).
- [137] A. J. Huber, F. Keilmann, J. Wittborn, J. Aizpurua, and R. Hillenbrand. « Terahertz Near-Field Nanoscopy of Mobile Carriers in Single Semiconductor Nanodevices ». *Nano Letters* 8.11 (2008), pp. 3766–3770 (cit. on p. 29).
- [138] J.-G. Ramírez, A. Sharoni, Y. Dubi, M. E. Gómez, and Ivan K. Schuller. « First-order reversal curve measurements of the metal-insulator transition in VO₂: Signatures of persistent metallic domains ». *Phys. Rev. B* 79 (23 2009), p. 235110 (cit. on p. 31).
- [139] Shuo Liu, B. Phillabaum, E. W. Carlson, K. A. Dahmen, N. S. Vidhyadhiraja, M. M. Qazilbash, et al. « Random Field Driven Spatial Complexity at the Mott Transition in VO₂ ». *Phys. Rev. Lett.* 116 (3 2016), p. 036401 (cit. on pp. 31, 60, 87).
- [140] B. Phillabaum, E. W. Carlson, and K. A. Dahmen. « Spatial complexity due to bulk electronic nematicity in a superconducting underdoped cuprate ». *Nature Communications* 3.1 (2012), p. 915 (cit. on p. 31).
- [141] Ahrum Sohn, Haeri Kim, Dong-Wook Kim, Changhyun Ko, Shriram Ramanathan, Jonghyurk Park, et al. « Evolution of local work function in epitaxial VO₂ thin films spanning the metal-insulator transition ». *Applied Physics Letters* 101.19 (2012), p. 191605. eprint: https://pubs.aip.org/aip/apl/article-pdf/doi/10.1063/1.4766292/14260488/191605_1_online.pdf (cit. on p. 31).

- [142] Shruthi H. Shetty, Sumiksha Shetty, Chandra Singh, and Ashwath Rao. « Supervised Machine Learning: Algorithms and Applications ». *Fundamentals and Methods of Machine and Deep Learning*. John Wiley Sons, Ltd, 2022. Chap. 1, pp. 1–16. eprint: <https://onlinelibrary.wiley.com/doi/pdf/10.1002/9781119821908.ch1> (cit. on p. 34).
- [143] Iqbal H. Sarker. « Deep Learning: A Comprehensive Overview on Techniques, Taxonomy, Applications and Research Directions ». *SN Computer Science* 2.6 (2021), p. 420 (cit. on p. 35).
- [144] Anubhav Jain, Shyue Ping Ong, Geoffroy Hautier, Wei Chen, William Davidson Richards, Stephen Dacek, et al. « Commentary: The Materials Project: A materials genome approach to accelerating materials innovation ». *APL Materials* 1.1 (2013), p. 011002. eprint: https://pubs.aip.org/aip/apm/article-pdf/doi/10.1063/1.4812323/13163869/011002\1\1_online.pdf (cit. on p. 36).
- [145] Yann LeCun, Yoshua Bengio, and Geoffrey Hinton. « Deep learning ». *Nature* 521.7553 (2015), pp. 436–444 (cit. on p. 36).
- [146] Steve Lawrence, C Lee Giles, Ah Chung Tsoi, and Andrew D Back. « Face recognition: A convolutional neural-network approach ». *IEEE transactions on neural networks* 8.1 (1997), pp. 98–113 (cit. on p. 36).
- [147] Srinivas C Turaga, Joseph F Murray, Viren Jain, Fabian Roth, Moritz Helmstaedter, Kevin Briggman, et al. « Convolutional networks can learn to generate affinity graphs for image segmentation ». *Neural computation* 22.2 (2010), pp. 511–538 (cit. on p. 36).
- [148] Xiaoting Zhong, Brian Gallagher, Shusen Liu, Bhavya Kailkhura, Anna Hiszpanski, and T. Yong-Jin Han. « Explainable machine learning in materials science ». *npj Computational Materials* 8.1 (2022), p. 204 (cit. on p. 37).
- [149] Chris Olah, Alexander Mordvintsev, and Ludwig Schubert. « Feature Visualization ». *Distill* (2017) (cit. on p. 36).
- [150] M. Fäth, S. Freisem, A. A. Menovsky, Y. Tomioka, J. Aarts, and J. A. Mydosh. « Spatially Inhomogeneous Metal-Insulator Transition in Doped Manganites ». *Science* 285.5433 (1999), pp. 1540–1542. eprint: <https://www.science.org/doi/pdf/10.1126/science.285.5433.1540> (cit. on p. 39).
- [151] A. S. McLeod, E. van Heumen, J. G. Ramirez, S. Wang, T. Saerbeck, S. Guenon, et al. « Nanotextured phase coexistence in the correlated insulator V₂O₃ ». *Nature Physics* 13.1 (2017), pp. 80–86 (cit. on p. 39).
- [152] Tian Miao, Lina Deng, Wenting Yang, Jinyang Ni, Changlin Zheng, Joanne Etheridge, et al. « Direct experimental evidence of physical origin of electronic phase separation in manganites ». *Proceedings of the National Academy of Sciences* 117.13 (2020), pp. 7090–7094. eprint: <https://www.pnas.org/doi/pdf/10.1073/pnas.1920502117> (cit. on pp. 39, 40).
- [153] Jiarui Li, Jonathan Pellicciari, Claudio Mazzoli, Sara Catalano, Forrest Simmons, Jerzy T. Sadowski, et al. « Scale-invariant magnetic textures in the strongly correlated oxide NdNiO₃ ». *Nature Communications* 10.1 (2019), p. 4568 (cit. on pp. 39, 40).
- [154] Y. Kohsaka, C. Taylor, K. Fujita, A. Schmidt, C. Lupien, T. Hanaguri, et al. « An Intrinsic Bond-Centered Electronic Glass with Unidirectional Domains in Underdoped Cuprates ». *Science* 315.5817 (2007), pp. 1380–1385. eprint: <https://www.science.org/doi/pdf/10.1126/science.1138584> (cit. on pp. 39, 40).
- [155] Md Hosne Mobarak, Mariam Akter Mimona, Md. Aminul Islam, Nayem Hossain, Fatema Tuz Zohura, Ibnul Imtiaz, et al. « Scope of machine learning in materials research—A review ». *Applied Surface Science Advances* 18 (2023), p. 100523 (cit. on p. 39).
- [156] Sergei V. Kalinin, Evgheni Strelcov, Alex Belianinov, Suhas Somnath, Rama K. Vasudevan, Eric J. Lingerfelt, et al. « Big, Deep, and Smart Data in Scanning Probe Microscopy ». *ACS Nano* 10.10 (2016), pp. 9068–9086 (cit. on p. 40).
- [157] W. Ma, E. J. Kautz, A. Baskaran, A. Chowdhury, V. Joshi, B. Yener, et al. « Image-driven discriminative and generative machine learning algorithms for establishing microstructure–processing relationships ». *Journal of Applied Physics* 128.13 (2020), p. 134901. eprint: https://pubs.aip.org/aip/jap/article-pdf/doi/10.1063/5.0013720/15254529/134901\1\1_online.pdf (cit. on p. 40).
- [158] Maxim Ziatdinov, Dohyung Kim, Sabine Neumayer, Liam Collins, Mahshid Ahmadi, Rama K. Vasudevan, et al. « Super-resolution and signal separation in contact Kelvin probe force microscopy of electrochemically active ferroelectric materials ». *Journal of Applied Physics* 128.5 (2020), p. 055101. eprint: https://pubs.aip.org/aip/jap/article-pdf/doi/10.1063/5.0013847/19773031/055101\1\1_online.pdf (cit. on p. 40).

- [159] Rama K. Vasudevan, Kyle P. Kelley, Eugene Eliseev, Stephen Jesse, Hiroshi Funakubo, Anna Morozovska, et al. « Bayesian inference in band excitation scanning probe microscopy for optimal dynamic model selection in imaging ». *Journal of Applied Physics* 128.5 (2020), p. 054105. eprint: https://pubs.aip.org/aip/jap/article-pdf/doi/10.1063/5.0005323/14894587/054105_1_online.pdf (cit. on p. 40).
- [160] Ruho Kondo, Shunsuke Yamakawa, Yumi Masuoka, Shin Tajima, and Ryoji Asahi. « Microstructure recognition using convolutional neural networks for prediction of ionic conductivity in ceramics ». *Acta Materialia* 141 (2017), pp. 29–38 (cit. on p. 40).
- [161] Felipe Oviedo, Zekun Ren, Shijing Sun, Charles Settens, Zhe Liu, Noor Titan Putri Hartono, et al. « Fast and interpretable classification of small X-ray diffraction datasets using data augmentation and deep neural networks ». *npj Computational Materials* 5.1 (2019), p. 60 (cit. on p. 41).
- [162] Alyson Spitzig, Adam Pivonka, Alex Frenzel, Jeehoon Kim, Changhyun Ko, You Zhou, et al. « Nanoscale thermal imaging of VO₂ via Poole–Frenkel conduction ». *Applied Physics Letters* 120.15 (2022), p. 151602. eprint: https://pubs.aip.org/aip/apl/article-pdf/doi/10.1063/5.0086932/19800345/151602_1_online.pdf (cit. on p. 42).
- [163] Joe Sakai, Satoshi Katano, Masashi Kuwahara, and Yoichi Uehara. « Pump–probe STM light emission spectroscopy for detection of photo-induced semiconductor–metal phase transition of VO₂ ». *Journal of Physics: Condensed Matter* 29.40 (2017), p. 405001 (cit. on p. 42).
- [164] Kenjiro K. Gomes, Abhay N. Pasupathy, Aakash Pushp, Shimpei Ono, Yoichi Ando, and Ali Yazdani. « Visualizing pair formation on the atomic scale in the high-T_c superconductor Bi₂Sr₂CaCu₂O₈+ δ ». *Nature* 447.7144 (2007), pp. 569–572 (cit. on p. 42).
- [165] *Thermal properties of Sapphire* (cit. on p. 45).
- [166] O. A. Osibote, R. Dendere, S. Krishnan, and T. S. Douglas. « Automated focusing in bright-field microscopy for tuberculosis detection ». *Journal of Microscopy* 240 (2 2010), pp. 155–163 (cit. on p. 47).
- [167] Eric Krotkov. « Focusing ». *International Journal of Computer Vision* 1 (1987), pp. 223–237 (cit. on p. 47).
- [168] M. I. Shah, S. Mishra, M. Sarkar, and C. Rout. « Identification of robust focus measure functions for the automated capturing of focused images from Ziehl–Neelsen stained sputum smear microscopy slide ». *Cytometry Part A* 91 (8 2017), pp. 800–809 (cit. on p. 47).
- [169] Manuel Guizar-Sicairos, Samuel T Thurman, and James R Fienup. « Efficient subpixel image registration algorithms ». *OPTICS LETTERS* 100 (2 2008) (cit. on p. 53).
- [170] Shuo Liu, B. Phillabaum, E. W. Carlson, K. A. Dahmen, N. S. Vidhyadhiraja, M. M. Qazilbash, et al. « Random Field Driven Spatial Complexity at the Mott Transition in VO₂ ». *Physical Review Letters* 116 (3 2016) (cit. on pp. 55, 98, 103).
- [171] M. Gurvitch, S. Luryi, A. Polyakov, and A. Shabalov. « Nonhysteretic behavior inside the hysteresis loop of VO₂ and its possible application in infrared imaging ». *Journal of Applied Physics* 106 (10 2009) (cit. on pp. 60, 65).
- [172] Amos Sharoni, Juan Gabriel Ramirez, and Ivan K. Schuller. « Multiple avalanches across the metal-insulator transition of vanadium oxide nanoscaled junctions ». *Physical Review Letters* 101 (2 2008) (cit. on p. 61).
- [173] C. L. Gomez-Heredia, J. A. Ramirez-Rincon, J. Ordonez-Miranda, O. Ares, J. J. Alvarado-Gil, C. Champeaux, et al. « Thermal hysteresis measurement of the VO₂ emissivity and its application in thermal rectification ». *Scientific Reports* 8.1 (2018) (cit. on p. 63).
- [174] Huaifu Zhang, Zhiming Wu, Cao Wang, and Yan Sun. « VO₂ film with small hysteresis width and low transition temperature ». *Vacuum* 170 (2019), p. 108971 (cit. on p. 65).
- [175] Paolo Maffezzoni, Luca Daniel, Nikhil Shukla, Suman Datta, and Arijit Raychowdhury. « Modeling and Simulation of Vanadium Dioxide Relaxation Oscillators ». *IEEE Transactions on Circuits and Systems I: Regular Papers* 62.9 (2015), 2207–2215 (cit. on p. 65).
- [176] Muhammad A. Butt, Cuma Tyszkiewicz, Paweł Karasiński, Magdalena Zięba, Andrzej Kaźmierczak, Maria Zdończyk, et al. « Optical Thin Films Fabrication Techniques—Towards a Low-Cost Solution for the Integrated Photonic Platform: A Review of the Current Status ». *Materials* 15.13 (2022) (cit. on p. 65).
- [177] Yuanjun Yang, Liangxin Wang, Haoliang Huang, Chaoyang Kang, Haitao Zong, Chongwen Zou, et al. « Controlling metal-insulator transition in (010)-VO₂/(0001)-Al₂O₃ epitaxial thin film through surface morphological engineering ». *Ceramics International* 44.3 (2018), pp. 3348–3355 (cit. on p. 66).

- [178] Huafu Zhang, Zhiming Wu, Xuefei Wu, Wenyao Yang, and Yadong Jiang. « Transversal grain size effect on the phase-transition hysteresis width of vanadium dioxide films comprising spheroidal nanoparticles ». *Vacuum* 104 (2014), pp. 47–50 (cit. on p. 68).
- [179] Jie Jian, Aiping Chen, Youxing Chen, Xinghang Zhang, and Haiyan Wang. « Roles of strain and domain boundaries on the phase transition stability of VO₂ thin films ». *Applied Physics Letters* 111.15 (2017), p. 153102. eprint: https://pubs.aip.org/aip/apl/article-pdf/doi/10.1063/1.4991882/13161021/153102_1_online.pdf (cit. on p. 68).
- [180] R. A. Aliev, V. N. Andreev, V. M. Kapralova, V. A. Klimov, A. I. Sobolev, and E. B. Shadrin. « Effect of grain sizes on the metal-semiconductor phase transition in vanadium dioxide polycrystalline thin films ». *Physics of the Solid State* 48.5 (2006), pp. 929–934 (cit. on p. 68).
- [181] F. Bêteille and J. Livage. « Optical Switching in VO₂ Thin Films ». *Journal of Sol-Gel Science and Technology* 13.1 (1998), pp. 915–921 (cit. on p. 68).
- [182] Naor Vardi, Elihu Anouchi, Tony Yamin, Srimanta Middey, Michael Kareev, Jak Chakhalian, et al. « Ramp-Reversal Memory and Phase-Boundary Scarring in Transition Metal Oxides ». *Advanced Materials* 29.21 (2017), p. 1605029. eprint: <https://onlinelibrary.wiley.com/doi/pdf/10.1002/adma.201605029> (cit. on pp. 70, 72–74).
- [183] Elihu Anouchi, Naor Vardi, Yoav Kalcheim, Ivan K. Schuller, and Amos Sharoni. « Universality and microstrain origin of the ramp reversal memory effect ». *Phys. Rev. B* 106 (20 2022), p. 205145 (cit. on p. 70).
- [184] Horng-Ming You, Ulrich M. Gösele, and Teh Y. Tan. « Simulation of the transient indiffusion-segregation process of triply negatively charged Ga vacancies in GaAs and AlAs/GaAs superlattices ». *Journal of Applied Physics* 74.4 (1993), pp. 2461–2470. eprint: https://pubs.aip.org/aip/jap/article-pdf/74/4/2461/18660580/2461_1_online.pdf (cit. on p. 84).
- [185] L. Burzawa, S. Liu, and E. W. Carlson. « Classifying surface probe images in strongly correlated electronic systems via machine learning ». *Phys. Rev. Mater.* 3 (3 2019), p. 033805 (cit. on p. 86).
- [186] Agnieszka Pregowska, Agata Roszkiewicz, Magdalena Osial, and Michael Giersig. « How scanning probe microscopy can be supported by artificial intelligence and quantum computing? » *Microscopy Research and Technique* (2024) (cit. on p. 86).
- [187] Juan Carrasquilla. « Machine learning for quantum matter ». *Advances in Physics: X* 5.1 (2020), p. 1797528. eprint: <https://doi.org/10.1080/23746149.2020.1797528> (cit. on p. 86).
- [188] Giuseppe Carleo, Ignacio Cirac, Kyle Cranmer, Laurent Daudet, Maria Schuld, Naftali Tishby, et al. « Machine learning and the physical sciences ». *Rev. Mod. Phys.* 91 (4 2019), p. 045002 (cit. on p. 86).
- [189] Edwin Bedolla, Luis Carlos Padierna, and Ramón Castañeda-Priego. « Machine learning for condensed matter physics ». *Journal of Physics: Condensed Matter* 33.5 (2020), p. 053001 (cit. on pp. 86, 87).
- [190] Pankaj Mehta, Marin Bukov, Ching-Hao Wang, Alexandre G.R. Day, Clint Richardson, Charles K. Fisher, et al. « A high-bias, low-variance introduction to Machine Learning for physicists ». *Physics Reports* 810 (2019), pp. 1–124 (cit. on p. 86).
- [191] S. S. Schoenholz, E. D. Cubuk, D. M. Sussman, E. Kaxiras, and A. J. Liu. « A structural approach to relaxation in glassy liquids ». *Nature Physics* 12.5 (2016), pp. 469–471 (cit. on p. 86).
- [192] Louis-Fran çois Arsenault, Alejandro Lopez-Bezanilla, O. Anatole von Lilienfeld, and Andrew J. Millis. « Machine learning for many-body physics: The case of the Anderson impurity model ». *Phys. Rev. B* 90 (15 2014), p. 155136 (cit. on p. 86).
- [193] Giuseppe Carleo and Matthias Troyer. « Solving the quantum many-body problem with artificial neural networks ». *Science* 355.6325 (2017), pp. 602–606. eprint: <https://www.science.org/doi/pdf/10.1126/science.aag2302> (cit. on p. 86).
- [194] Alejandro Lopez-Bezanilla and O. Anatole von Lilienfeld. « Modeling electronic quantum transport with machine learning ». *Phys. Rev. B* 89 (23 2014), p. 235411 (cit. on p. 86).
- [195] Luca M. Ghiringhelli, Jan Vybiral, Sergey V. Levchenko, Claudia Draxl, and Matthias Scheffler. « Big Data of Materials Science: Critical Role of the Descriptor ». *Phys. Rev. Lett.* 114 (10 2015), p. 105503 (cit. on p. 86).
- [196] Jonathan Schmidt, Mário R. G. Marques, Silvana Botti, and Miguel A. L. Marques. « Recent advances and applications of machine learning in solid-state materials science ». *npj Computational Materials* 5.1 (2019), p. 83 (cit. on p. 86).

-
- [197] Suheng Xu, Alexander S. McLeod, Xinzhong Chen, Daniel J. Rizzo, Bjarke S. Jessen, Ziheng Yao, et al. « Deep Learning Analysis of Polaritonic Wave Images ». *ACS Nano* 15.11 (2021), pp. 18182–18191 (cit. on p. 86).
- [198] Xinzhong Chen, Ziheng Yao, Suheng Xu, Alexander S. McLeod, Stephanie N. Gilbert Corder, Yueqi Zhao, et al. « Hybrid Machine Learning for Scanning Near-Field Optical Spectroscopy ». *ACS Photonics* 8.10 (2021), pp. 2987–2996 (cit. on p. 86).
- [199] Lei Wang. « Discovering phase transitions with unsupervised learning ». *Phys. Rev. B* 94 (19 2016), p. 195105 (cit. on p. 87).
- [200] P. Ronhovde, S. Chakrabarty, D. Hu, M. Sahu, K. K. Sahu, K. F. Kelton, et al. « Detecting hidden spatial and spatio-temporal structures in glasses and complex physical systems by multiresolution network clustering ». *The European Physical Journal E* 34.9 (2011), p. 105 (cit. on p. 87).
- [201] Daniel S. Fisher. « Scaling and critical slowing down in random-field Ising systems ». *Phys. Rev. Lett.* 56 (5 1986), pp. 416–419 (cit. on p. 102).
- [202] Olga Perković, Karin Dahmen, and James P. Sethna. « Avalanches, Barkhausen Noise, and Plain Old Criticality ». *Phys. Rev. Lett.* 75 (24 1995), pp. 4528–4531 (cit. on p. 102).

RÉSUMÉ

Si l'IA continue de progresser, l'informatique traditionnelle peine à suivre le rythme. Inspirée par le cerveau, l'informatique neuromorphique combine traitement et mémoire pour créer des systèmes optimisés pour les tâches d'IA. Les matériaux clés pour cette technologie sont les synaptors, matériaux à mémoire non-volatile, et les neuristors, matériaux pulsants électriquement. Cependant, les matériaux fonctionnant bien comme synaptors ne fonctionnent souvent pas comme neuristors et vice versa. VO_2 , connu pour être un bon neuristor, peut potentiellement se comporter en synaptor à température ambiante. Pour étudier cela, une nouvelle technique de microscopie optique a été développée pour suivre en température la transition isolant-métal dans VO_2 . Celle-ci nous a permis de cartographier pour la première fois la mémoire non-volatile et de dévoiler la physique sous-jacente, par analyse en apprentissage automatique, conduisant à la formation de motifs fractals.

MOTS CLÉS

circuit neuromorphique, dioxyde de vanadium, transition isolant-métal, caractérisation optique, mémoire non-volatile, réseau neuronal convolutionnel

ABSTRACT

As AI continues to advance, traditional computer designs struggle to keep up. Inspired by the brain, neuromorphic computing combines processing and memory to create faster and more efficient systems, perfect for AI tasks like deep learning and pattern recognition. Key materials for this technology are synaptors implemented as non-volatile memory materials and neuristors, electrically spiking materials. However, materials that work well as synaptors often don't work as neuristors and vice versa. VO_2 , known to be a good spiking neuristor, is a promising synaptor near room temperature. To study this, a new optical microscopy technique was developed to track insulator-to-metal maps in VO_2 using various temperature ramps. This technique allowed us to map for the first time non-volatile memory in VO_2 and to unveil the underlying physics, using new machine learning analysis, driving the formation of fractal patterns in VO_2 .

KEYWORDS

neuromorphic devices, vanadium dioxide, insulating-to-metal transition, optical characterization, non-volatile memory, convolutional neural network